

---

---

# Effects of Manufacturing Variables on Performance of High-Level Waste Low Carbon Steel Containers

Final Report

---

---

Prepared by R. H. Frost, T. R. Muth, A. L. Liby

**Manufacturing Sciences Corporation**

Prepared for  
**U.S. Nuclear Regulatory Commission**

*Legacy-70*

## AVAILABILITY NOTICE

### Availability of Reference Materials Cited in NRC Publications

Most documents cited in NRC publications will be available from one of the following sources:

1. The NRC Public Document Room, 2120 L Street, NW, Lower Level, Washington, DC 20555
2. The Superintendent of Documents, U.S. Government Printing Office, P.O. Box 37082, Washington, DC 20013-7082
3. The National Technical Information Service, Springfield, VA 22161

Although the listing that follows represents the majority of documents cited in NRC publications, it is not intended to be exhaustive.

Referenced documents available for inspection and copying for a fee from the NRC Public Document Room include NRC correspondence and internal NRC memoranda; NRC Office of Inspection and Enforcement bulletins, circulars, information notices, inspection and investigation notices; Licensee Event Reports; vendor reports and correspondence; Commission papers; and applicant and licensee documents and correspondence.

The following documents in the NUREG series are available for purchase from the GPO Sales Program: formal NRC staff and contractor reports, NRC-sponsored conference proceedings, and NRC booklets and brochures. Also available are Regulatory Guides, NRC regulations in the *Code of Federal Regulations*, and *Nuclear Regulatory Commission Issuances*.

Documents available from the National Technical Information Service include NUREG series reports and technical reports prepared by other federal agencies and reports prepared by the Atomic Energy Commission, forerunner agency to the Nuclear Regulatory Commission.

Documents available from public and special technical libraries include all open literature items, such as books, journal and periodical articles, and transactions. *Federal Register* notices, federal and state legislation, and congressional reports can usually be obtained from these libraries.

Documents such as theses, dissertations, foreign reports and translations, and non-NRC conference proceedings are available for purchase from the organization sponsoring the publication cited.

Single copies of NRC draft reports are available free, to the extent of supply, upon written request to the Office of Information Resources Management, Distribution Section, U.S. Nuclear Regulatory Commission, Washington, DC 20555.

Copies of industry codes and standards used in a substantive manner in the NRC regulatory process are maintained at the NRC Library, 7920 Norfolk Avenue, Bethesda, Maryland, and are available there for reference use by the public. Codes and standards are usually copyrighted and may be purchased from the originating organization or, if they are American National Standards, from the American National Standards Institute, 1430 Broadway, New York, NY 10018.

## DISCLAIMER NOTICE

This report was prepared as an account of work sponsored by an agency of the United States Government. Neither the United States Government nor any agency thereof, or any of their employees, makes any warranty, expressed or implied, or assumes any legal liability of responsibility for any third party's use, or the results of such use, of any information, apparatus, product or process disclosed in this report, or represents that its use by such third party would not infringe privately owned rights.

---

---

# Effects of Manufacturing Variables on Performance of High-Level Waste Low Carbon Steel Containers

## Final Report

---

---

Manuscript Completed: August 1989  
Date Published: April 1990

Prepared by  
R. H. Frost,\* T. R. Muth, A. L. Liby

Manufacturing Sciences Corporation  
804 Kerr Hollow Rd.  
P.O. Box 886  
Oak Ridge, TN 37831

\*Colorado School of Mines, Golden, Colorado

Prepared for  
Division of Engineering  
Office of Nuclear Regulatory Research  
U.S. Nuclear Regulatory Commission  
Washington, DC 20555  
NRC FIN B7278

## ABSTRACT

Analytical and experimental research was performed to determine the effect of manufacturing variables on the performance of cast steel overpacks. The work examines the influence of casting and welding process variables on the long-term performance of low carbon steel overpacks in the repository environment.

Centrifugal casting was indicated to be the most economical and technically favorable manufacturing approach for cast steel overpacks. A bottom would be welded into a hollow cylinder to make the container and final closure welding to secure the lid in place would be done at the repository. Effects of alloy chemistry, solidification processing, and solid state phase transformations on final microstructure of the cast and welded overpack has been examined in detail in this report.

Codes and standards governing the manufacture of overpacks do not presently exist. An extension of the ASME Boiler and pressure vessel code supplemented by government standards could be adopted for the purpose. Standard, well-established methods of non-destructive evaluation are adequate for the purpose of identifying likely manufacturing defects.

Experimental work focused on material and process combinations to be used in manufacture of overpacks. Practical process limits were explored and changes in microstructure due to repository thermal conditions were investigated.

## TABLE OF CONTENTS

	<u>Page</u>
Abstract. . . . .	iii
List of Figures . . . . .	vii
List of Tables. . . . .	xi
1. INTRODUCTION. . . . .	1
2. SURVEY OF LITERATURE AND INDUSTRIAL PRACTICE. . . . .	3
2.1 Overpack Container Manufacturing Techniques. . . . .	3
2.2 Ferrous Microstructures and Phase Transformations During Heat Treatment and Welding. . . . .	7
2.3 Corrosion Behavior . . . . .	12
2.4 Microstructural Alteration During Repository Storage . . . . .	18
2.5 Casting Processes. . . . .	19
2.5.1 Process Variables and Process Control . . . . .	19
2.5.2 Chemical Control During Melting Processes . . . . .	21
2.5.3 Heat Transport and Solidification Structure . . . . .	22
2.5.4 Segregation and Casting Defects . . . . .	26
2.6 Welding Processes. . . . .	29
2.6.1 Welding Process Variables and Process Control . . . . .	29
2.6.2 Welding Consumables . . . . .	31
2.6.2.1 Submerged Arc Consumables. . . . .	32
2.6.2.2 Gas Metal Arc Consumables. . . . .	35
2.6.3 The Heat Affected Zone. . . . .	36
2.6.4 New Grades of Microalloyed Steels . . . . .	40
2.6.5 Microstructure and Toughness. . . . .	40
2.6.6 Mechanical Properties of Low Carbon Steel Weld Metal. . . . .	47
2.7 Quality Assurance. . . . .	48
2.7.1 Codes and Standards . . . . .	48
2.7.2 Qualification and Certification . . . . .	50
2.7.3 Inspection. . . . .	51

TABLE OF CONTENTS

	<u>Page</u>
3. EXPERIMENTAL RESEARCH . . . . .	53
3.1 Experimental Rationale . . . . .	53
3.2 Casting Production and Heat Treatment. . . . .	58
3.3 Welding Experiments. . . . .	67
3.3.1 Weld Microstructures. . . . .	70
3.3.2 Thermal Profiling . . . . .	73
3.3.3 Gleeble Simulation. . . . .	79
3.3.4 Discussion of Welding Experiments . . . . .	82
4. RESULTS AND CONCLUSIONS . . . . .	102
4.1 Manufacturing Considerations . . . . .	102
4.2 Metallurgical Considerations. . . . .	102
4.3 Defects from Manufacturing . . . . .	103
4.4 Quality Assurance. . . . .	103
4.5 Experimental Research. . . . .	104
5. REFERENCES. . . . .	105

## LIST OF FIGURES

		Page
Figure 1.	A typical static casting of the dimensions of the overpack container showing the riser.	4
Figure 2.	Schematic representation of the Watertown and Delavoud methods for centrifugal casting in the horizontal position (8)	6
Figure 3.	Iron-Carbon phase Diagram [from V. 8 Metals Hbk]	8
Figure 4.	Schematic continuous cooling transformation diagram.	11
Figure 5.	General corrosion rate vs. time for forged and cast steels immersed in de-aerated seawater at 90°C (14).	14
Figure 6.	Grain size in the heat affected zone as a function of peak temperature and distance from the fusion line (14).	37
Figure 7.	Schematic CCT diagrams showing the influence of inclusions on the nucleation of acicular ferrite (150).	45
Figure 8.	Schematic CCT diagram showing the influence of cooling rate on weld microstructure (134).	46
Figure 9.	Influence of silicon and manganese on the dissolved oxygen content (5).	55
Figure 10.	Concentration of silicon and manganese in iron in equilibrium with silica-saturated manganese-silicate melts (5).	56
Figure 11.	Experimental data on dendrite arm spacings in commercial steels containing from 0.1 to 0.9 weight percent carbon (45).	57
Figure 12.	A schematic diagram of the furnace solidifying equipment used to model static casting.	60

	Page
Figure 13.	Cooling curves obtained from furnace solidified specimens. 61
Figure 14.	Mold configuration prior to tapping steel. 62
Figure 15.	A schematic of the slow cooling device used to slow the cooling rate of one inch (25.4 mm) thick plate to that of a six inch (152.4 mm) thick plate. 66
Figure 16.	A schematic diagram of submerged arc welding setup and instrumentation. 69
Figure 17.	Experimentally determined process space for a heat input of 1.5 MJ/m. 71
Figure 18.	Experimentally determined process space for a heat input of 2.0 MJ/m. 72
Figure 19.	Joint configuration used for multiple pass welding. 74
Figure 20.	Changes in thermal conductivity with temperature for a variety of steels. 77
Figure 21.	Experimentally measured and analytically derived thermal profiles describing specific areas in the heat affected zone. 78
Figure 22.	Measured peak temperatures versus distance from the fusion line for a heat input of 1.5 MJ/m. 80
Figure 23.	Measured and theoretical $t_{8-5}$ times as a function of heat input. 81
Figure 24.	Continuous cooling transformation diagram for AISI 1018 steel (35). 83
Figure 25.	Unetched photomicrographs of the four steel compositions showing the nonmetallic inclusions. (100X) 84

	Page
Figure 26. Photomicrographs of the four heat affected zone subzones in an off chemistry experimental weldment. The top micrograph shows the fusion line and grain growth region, the middle is recrystallized zone, and the bottom shows the partially transformed zone and tempered zone. 2% nital 50X.	86
Figure 27. The fusion line (top) and grain growth region of the four welds studied, showing the microstructural differences directly next to the fusion line. Yorgason's etch, 50X.	87
Figure 28. The grain growth region of each of the four steels showing microstructural differences related to cleanliness and alloy content. Yorgason's etch, 156X.	88
Figure 29. Microstructures of the experimental steels that were thermally cycled by a Gleeble 1500 weld simulator. The peak temperature seen is about 940°C. 2% nital 100X.	90
Figure 30. Microstructures of the experimental steels that were thermally cycled by a Gleeble 1500 weld simulator using a peak temperature of 1250°C. 2% nital, 100X.	91
Figure 31. Microstructures of the experimental steels that were thermally cycled by a Gleeble 1500 weld simulator using a peak temperature of 1450°C. 2% nital, 100X.	91
Figure 32. Location of microstructural observations and measurements.	96
Figure 33. Prior austenite grain size at the fusion line as a function of heat input for the test alloys.	97
Figure 34. Fraction of phases present as a function of distance from the fusion line for alloy 1.	98

		Page
Figure 35.	Fraction of phases present as a function of distance from the fusion line for alloy 2.	99
Figure 36.	Fraction of phases present as a function of distance from the fusion line for alloy 3.	100
Figure 37.	Fraction of phases present as a function of distance from the fusion line for alloy 4.	101

## LIST OF TABLES

		<u>Page</u>
Table 1.	Comparison of Undisturbed Repository Properties.	15
Table 2.	Compositions of Brine Solutions.	16
Table 3.	Comparison of the IIW and JWS Micro-structural Classification Schemes.	43
Table 4.	Chemical Composition Categories	53
Table 5.	Compositions of Four Pig Iron	59
Table 6.	Chemical Analysis of Melt Additions	64
Table 7.	Chemical Analysis of Steel Heats	64
Table 8.	Summary of Grain Sizes for ASTM A-216 Grade WCA Steel.	65
Table 9.	Parameters used for Single Pass GMA Welds.	70
Table 10.	Characteristics of Alloys Used for GMA Welding Experiments.	94
Table 11.	Percent of Area of Inclusions Observed in the Scanning Electron Microscope at 7500X Magnification.	94

## 1. INTRODUCTION

High level radioactive waste from U.S. defense programs and nuclear power generation will be packaged in engineered waste packages and placed in permanent storage in geologic repositories. Government responsibility for development of waste packages and repositories lies with the Department of Energy (DOE). Work is underway within DOE to develop repository sites and waste packages specifically designed to maintain long-term containment of the waste within the repository.

Disposal will be regulated in accordance with 10 CFR Part 60, a regulation under development by the Nuclear Regulatory Commission (NRC). The NRC is responsible for providing DOE with guidance concerning requirements for validation of waste package performance, assessing progress of the DOE program, and eventually to assess conformance of the waste package to the requirements of 10 CFR Part 60. In order to support their regulatory mission, the NRC undertook a research program to develop an understanding of the effects of design, materials and manufacturing processes on performance of the waste package. The research described herein is a part of that program.

The DOE has pursued three different repository development programs according to proposed location and geologic characteristics. The programs are: 1) Basalt Waste Isolation Project located at the DOE's Hanford Site, 2) Nevada Nuclear Waste Storage Investigations Project (NNWSI) at DOE's Nevada Test Site, and 3) Office of Nuclear Waste Isolation (ONWI) with possible locations in Utah, Texas, Louisiana and Mississippi.

Conceptual waste package designs have been prepared for each of the proposed repositories (1-3). The waste package typically consists of the waste form sealed in a metal canister, a metal overpack and packing material to fill the annular space between the overpack and the surrounding host rock. The various conceptual designs describe the metal overpack as a cast carbon steel vessel with end caps attached by welding.

The reference material of construction for the metal overpack is a cast low carbon steel conforming to ASTM A216 Grade WCA (4) with alloy chemistry modified to AISI Type 1018. The chemistry modification restricts carbon content to the 0.15-0.20 weight percent range to avoid excessive hardenability in the final closure weld. This weld will probably not be heat treated after welding. Low carbon steel was chosen as the reference material based upon its good fabricability, low cost, availability, and acceptable corrosion behavior.

The research described here is directed toward evaluation of the effects of manufacturing variables on the performance of the overpack component of various proposed DOE waste package designs. The various conceptual designs for overpacks cover a range of

lengths, diameters and wall thicknesses based upon such factors as corrosion allowance, thermal strength of the waste form and lithostatic pressures in the repository. The conceptual waste package design for the salt repository (3) is one of the more recent of those generated by the DOE effort, and it contains information on proposed manufacturing methods for overpacks. The overpack to contain defense high level waste in the salt repository is considered typical of the various overpack designs. It is a cylinder 338 cm. long, 64 cm. inside diameter, and 8.6 cm. wall thickness, and with end caps 16.7 cm thick. It is expected that the cylindrical body will be centrifugally cast, while the heads will be statically cast. The bottom end cap will be joined to the body as a shop assembly operation using the submerged arc welding process. The top end cap will be remotely welded on as a hot cell operation at the repository. Narrow gap gas metal arc welding will probably be used for the final closure to avoid problems of flux handling and removal in the hot cell environment.

The work presented here includes experimentation as well as interpretation of literature particularly significant to the manufacture of low carbon steel overpacks by casting and welding. The focus is on the microstructure of low carbon steel castings and weldments, and on how casting and welding process variables influence that microstructure and the resulting long term performance of high level waste overpacks in the repository environment. It is the microstructure that carries the signature of the prior thermal experience of the casting and welding processes. The microstructure can be related directly to properties which include both the mechanical and corrosion behavior. The degree of control of the casting and welding processes can be interpreted from microstructural analysis of the resulting canister assembly.

## 2. SURVEY OF LITERATURE AND INDUSTRIAL PRACTICE

### 2.1. Overpack Container Manufacturing Techniques

The candidate processes for production of cylindrical, heavy walled, steel overpack containers include: wrought processing, static casting, and centrifugal casting. In order to avoid human radiation exposure, the overpack containers must be remotely sealed by weld closure after placement of the radioactive waste. The candidate weld closure processes for sealing the container include: flux cored arc welding (FCAW), gas metal arc welding (GMAW), submerged arc welding (SAW) and electroslag welding (ESW). This section of the report provides a summary of the various candidate fabrication and weld closure processes. Forging, ring rolling, and piercing are viable wrought processes for the fabrication of heavy walled cylinders for application as overpack containers. However, these processes require a large ingot or casting for starting material (5). An initial survey of possible manufacturing methods concluded that there was some question as to the forging capacity in the United States, and that wrought processing would be much more costly than casting processes for overpack container fabrication. For these reasons, wrought processing will not be considered in the present study.

The casting processes available for overpack container production include static casting in sand or metal molds and centrifugal casting. A static casting of the dimensions of the overpack container must be pit molded. This technique will yield a much different microstructure than that of a wrought product of the same dimensions. The solidification time may be as long as 30 hours (6). This solidification time will yield a coarse solidification structure with secondary dendrite arm spacing of around 1000 micrometers. A very coarse solidification microstructure may be detrimental to mechanical performance because of the large amounts of microsegregation and macrosegregation, and the limited ability to homogenize composition differences because of large diffusion distances. The process variables which must be considered for the static casting of large heavy walled cylinders include: feeding, risering, core buoyancy, shake-out time, molding time and clean-up procedure. For large chunky steel castings it can be expected that 40 to 50 percent of the total tonnage cast will be gates, runners and risers (7). This low yield is a tremendous expense. The positioning of the required risers is shown in Figure 1. Another consideration is that the casting must be bottom poured to prevent oxidation, splashing, and cold shuts (8). The feeding system must be pressurized to insure uniform feeding and short pouring times. A typical design of the feeding system is shown in Figure 1.

Core buoyancy will be a major factor in determining the reinforcement of the central core and the type of sand binder used to achieve the required core strengths. This force requires the use of reinforcing bars to prevent core distortion, and the welding of the reinforcing bars to an external structure to

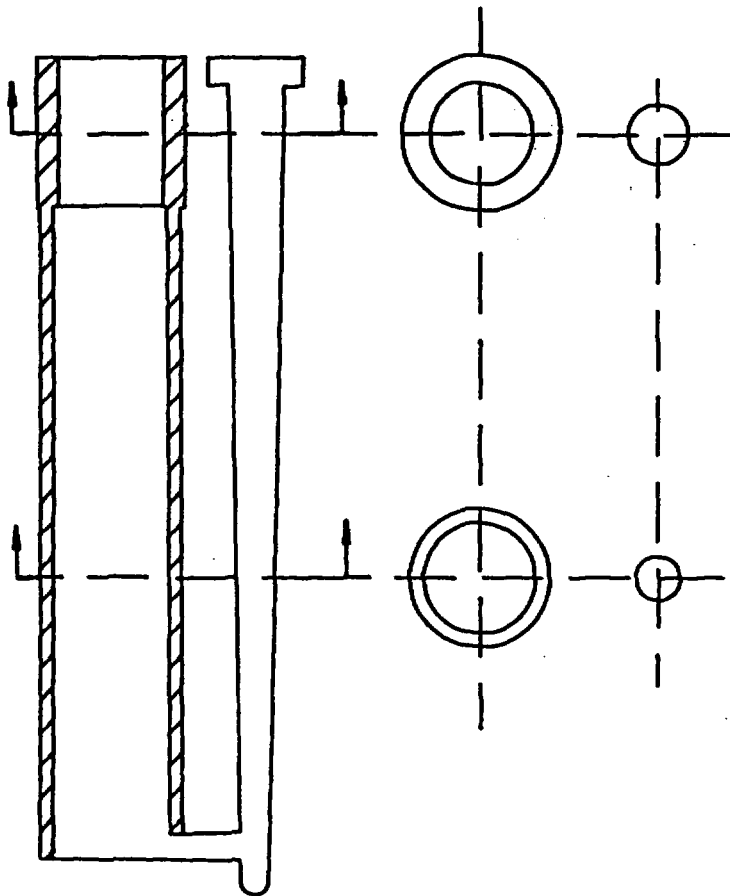


Figure 1: A typical static casting of the dimensions of the overpack container showing the riser.

prevent core shift. These procedures are time consuming with the result that pit molding is labor intensive and costly. In addition to long molding times, the shake out times for large pit molded castings can be as long as several weeks. The cleaning of large pit molded castings is a significant task. The risers shown in Figure 1 must be removed, and the surface must be cleaned by shot blasting or grinding. Weld repair to take care of blow hole porosity or shrinkage porosity may represent a significant cost, and non-destructive testing to provide radiographic quality is expected to be costly as well.

Centrifugal casting offers significant benefits for the production of cast overpack containers. The metal is poured into a cylindrical metal mold which is rotating at speeds of up to 2,000 rpm. The centrifugal force holds the metal against the wall while solidification proceeds. This enhances thermal contact between the surface of the casting and the mold wall, and provides a significant feeding force to prevent the development of porosity (10). Short castings can be poured with the axis of the mold vertical. In this case the centrifugal force causes the molten metal to flow up along the mold wall. Long castings are poured with the mold axis horizontal with one of the following techniques: The Watertown method, the DeLavaud method, and the German process (11).

The Watertown method uses a heavy cast iron chill mold which is coated with a refractory mold wash and spun at 1300 to 2000 rpm. When the mold is at speed a weighed amount of metal is poured into a pouring basin equipped with a short spout at the near end of the mold. The rate of entry into the mold is synchronized with spinning speed by regulating the spout diameter so that molten metal will be distributed evenly and without tearing the solidified, but hot, shell. Pressure is applied to the far end shortly after solidification to prevent mold restraint and subsequent tearing as the tube contracts lengthwise in the mold (2). See Figure 2 for diagram.

The DeLavaud method uses a thin walled, water cooled metal mold which is mounted on tracks and inclined at a slight angle to the horizontal. A pouring trough is extended into the spinning mold. Metal is deposited in a helix from the farthest end of the trough as the spinning mold is retracted (11). The German process, instead of using a mold wash, uses a fine sand deposited from a long trough over the mold surface. The cast iron mold is spray cooled with water to maintain dimensional tolerance and increase mold life. The thermal barrier provided by the sand reduces heat shock, lessens checking of the mold surface, and prevents surface laps on castings caused by premature freezing (11).

The advantages of centrifugal casting for the production of ferrous tubular products include: enhanced feeding without the need for a riser; a large yield compared with static casting techniques which require a riser; the elimination of cores and the requirement of costly and time consuming pit molding techniques, the segregation of non-metallic inclusions and slag

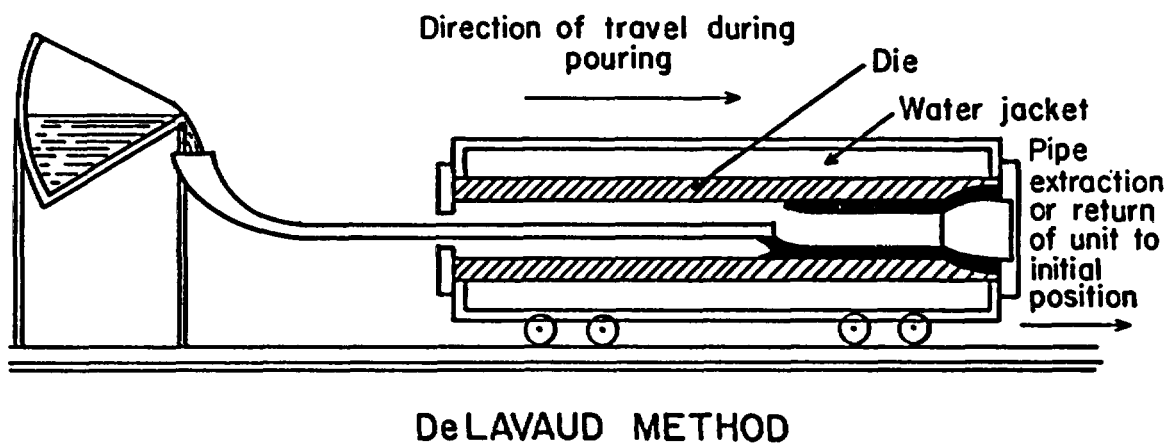
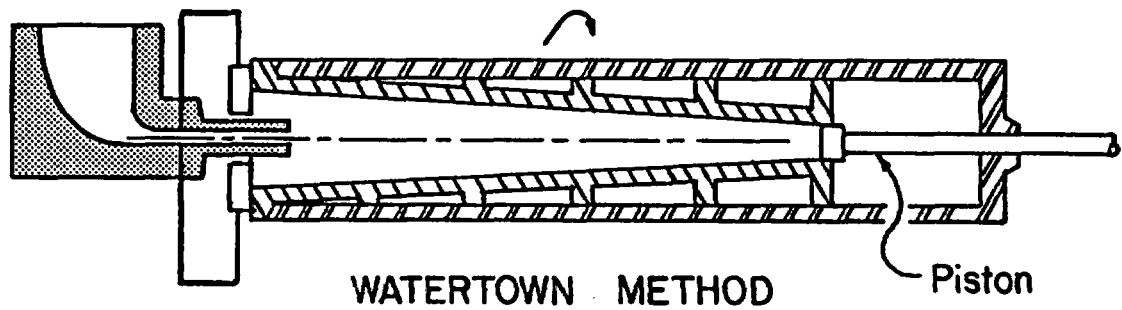


FIGURE 2. Schematic representation of the Watertown and Delavoud methods for centrifugal casting in the horizontal position (8).

to the inside surface of the casting; the development of a hollow cavity along the axis of the casting; and refinement of the solidification structure. The metal is forced out against the mold with a force of up to 200 g's (10) which provides an increase in the feeding force of two orders of magnitude over static castings. Slag and non-metallic inclusions are forced to the center by the centrifuging action, and the nucleation of gas bubbles and blow holes is suppressed by the high pressures.

The solidification structure of centrifugally cast steels is refined compared to that of statically cast steel of the same section thickness. All of the commercially available centrifugal casting techniques involve a metal (grey iron, steel or copper) mold which may or may not be water cooled. The solidification time for centrifugally cast cylinders is therefore significantly reduced compared to that for static sand castings. With the highly conductive mold metal interface more nuclei become active as sites for primary solidification. Since the number of grains depends on a competition between the rate of nucleation and the rate of growth a centrifugally cast vessel will have a smaller grain size than the statically cast vessel (12). After analysis of the various casting and forging processes, it is concluded that centrifugal casting is the technique most likely to be selected for the production of cylindrical high level nuclear waste overpack containers.

## 2.2 Ferrous Microstructures and Phase Transformations During Heat Treatment and Welding

Low carbon steels represent the most important group of weldable, economical alloys for nuclear waste canisters. Proper use of these alloys requires an understanding of the allotropic transformations in castings and weld fusion and heat affected zones. Figure 3 (13) shows the equilibrium phase diagram for the binary iron-carbon system. At high temperatures the face centered cubic austenite phase is capable of dissolving up to 2% carbon, but at low temperatures the body centered cubic ferrite phase can dissolve only about 0.02% carbon. At the eutectoid composition of 0.8% carbon the equilibrium microstructure (pearlite) consists of ferrite (Fe) and cementite ( $\text{Fe}_3\text{C}$ ) lamellae. The ferrite phase is a dilute Fe-C solid solution and the cementite phase is the compound  $\text{Fe}_3\text{C}$ . Mild steels with carbon contents in the range of 0.1 to 0.2% C will consist of ferrite plus pearlite. These microstructures are produced by cooling from the higher temperature austenite region at a cooling rate slow enough to allow the equilibrium decomposition of austenite into ferrite and cementite as indicated by the eutectoid transformation. At faster cooling rates the eutectoid reaction may not have sufficient time, and several non-equilibrium phases are possible. The morphology of these phases depends on the extent of carbon diffusion during the cooling process.

The microstructures of castings and welds are controlled by the metallurgical history which includes: the nature of the solidification processes, subsequent thermal processing such as

PHASE DIAGRAMS OF BINARY ALLOY SYSTEMS  
C - Fe CARBON - IRON

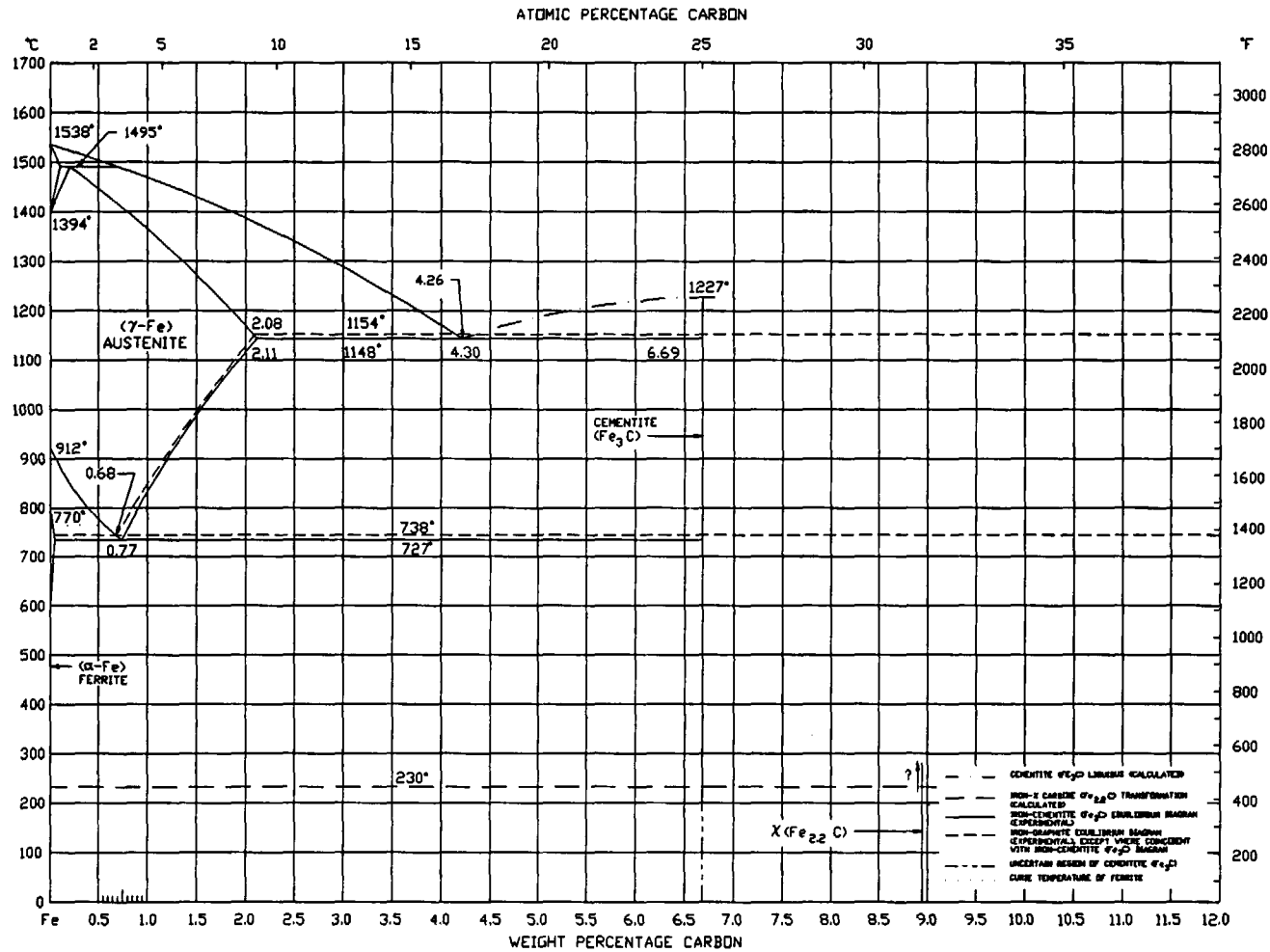


FIGURE 3. Iron-Carbon phase Diagram [from V. 8 Metals Hbk]

heat treating or welding which raise the temperature to a point where carbon diffusion can occur, and heating during long term storage of radioactive waste products. This discussion will deal first with solidification structures, and then with the equilibrium and non-equilibrium austenite decomposition reactions which occur as austenite cools below the eutectoid temperature at various cooling rates.

The phase diagram in Figure 3 shows that iron carbon alloys with carbon contents less than 0.5% C undergo the peritectic reaction during solidification. Sand and centrifugal castings exhibit dendritic solidification over a range of temperatures. The dendrites grow into the melt to create a liquid solid region referred to as the mushy zone. For steels with carbon contents in the peritectic region (Carbon < 0.5%), delta ferrite dendrites are the first solid to form as the melt cools below the liquidus line. These dendrites are of lower carbon composition than the liquid as dictated by the horizontal tie lines across the two phase delta ferrite - liquid region. Thus, carbon (and other solute elements) segregate to the liquid in between the dendrites. For substitutional solutes such as silicon, manganese, or nickel, this microsegregation will remain as interdendritic segregation or coring in the final solidification structure. The high diffusivity of carbon allows the peritectic reaction in Fe-C alloys to go to completion during the solidification process. At the peritectic temperature low carbon delta ferrite reacts with liquid at a higher carbon content to form austenite. This reaction takes place in the mushy zone during solidification so that only austenite dendrites remain when solidification is complete.

The solidification of low carbon steel weld metal is similar to the solidification of castings except that the thermal gradient is much higher, and the solidification velocity may be so high that secondary and tertiary dendrite arms do not fully develop. If the secondary dendrite arms are not developed the solidification structure is referred to as cellular or cellular-dendritic. In some cases the solidification at the weld center line is slow enough for fully developed dendrites. This tends to occur with high heat input welding processes such as electroslag welding or submerged arc welding which produce a large fusion zone. The microsegregation caused by solidification of the parent casting or the weld fusion zone remains as a component of the microstructure, and the differences in composition between the dendrite center line and the center of the interdendritic space may contribute to the development of the austenite decomposition microstructure. The solid state phase transformations which occur on heating or cooling through the eutectoid temperature have the most significant influence on the microstructure. When an equilibrium two phase (ferrite + cementite) microstructure is heated above the eutectoid temperature new austenite grains nucleate and grow at the grain boundaries. The transformation is complete at the A3 temperature which marks the upper boundary of the two phase ferrite plus austenite phase region. After the structure has completely

transformed, growth of the austenite grains becomes a significant variable. In general, large austenite grains provide resistance to the eutectoid transformation on cooling and lead to nonequilibrium martensitic or bainitic structures which have lower room temperature ductility. Excessive austenite grain growth can be minimized by limiting the time at high temperatures during heat treatment, and by providing second phase particles such as carbides or nitrides which act to pin the austenite grain boundaries and prevent growth.

The phase transformations which constitute austenite decomposition on cooling are of major significance for the room temperature microstructure. The nature of these transformations and their products are influenced by: the cooling rate and time for carbon diffusion; by the size of the austenite grains; and by the presence of alloy elements, tramp elements, or nonmetallic inclusions which increase or retard the rates of nucleation and growth.

The only alloy elements present in plain carbon steels such as ASTM A-216 are silicon and manganese which are added for deoxidation purposes. The manganese also forms primary manganese sulfides to prevent the formation of eutectic iron sulfides. Aluminum at low levels of around 0.05 wt.% is sometimes added for deoxidation. For these alloys the cooling rate and the extent of carbon diffusion during cooling are the major variables which control the microstructure. At the relatively slow cooling rates encountered during the cooling of castings in the mold, proeutectoid ferrite nucleates at the grain boundaries as the alloy cools below the A<sub>3</sub> temperature and grows out into the austenite grains with a rounded allotriomorphic morphology. As cooling proceeds below the A<sub>1</sub> (eutectoid temperature) the remaining austenite at the center of the grains transforms to the equilibrium pearlite structure which consists of alternating plates of ferrite and cementite.

The influence of the cooling rate on the nature of the austenite decomposition products is best illustrated by the continuous cooling transformation (CCT) diagram shown in Figure 4. The C-curves indicate the start or finish of the ferrite, pearlite, or bainite transformations, and the M<sub>s</sub> line along the bottom of the diagram indicates the start of the martensite transformation for cooling conditions which are rapid enough to avoid the diffusion controlled transformations.

With faster cooling rates such as those encountered in normalizing, there is less time for diffusion and the proeutectoid ferrite takes the form of thin plates (Widmanstätten ferrite) which grow into the austenite grains with preferred orientations. The pearlite transformation takes place more rapidly and at lower temperatures which yields a finer pearlite spacing. At the very fast cooling rates encountered during quenching proeutectoid ferrite may not form at all, and the pearlite transformation may be bypassed to form nonequilibrium microconstituents such as bainite or martensite at temperatures

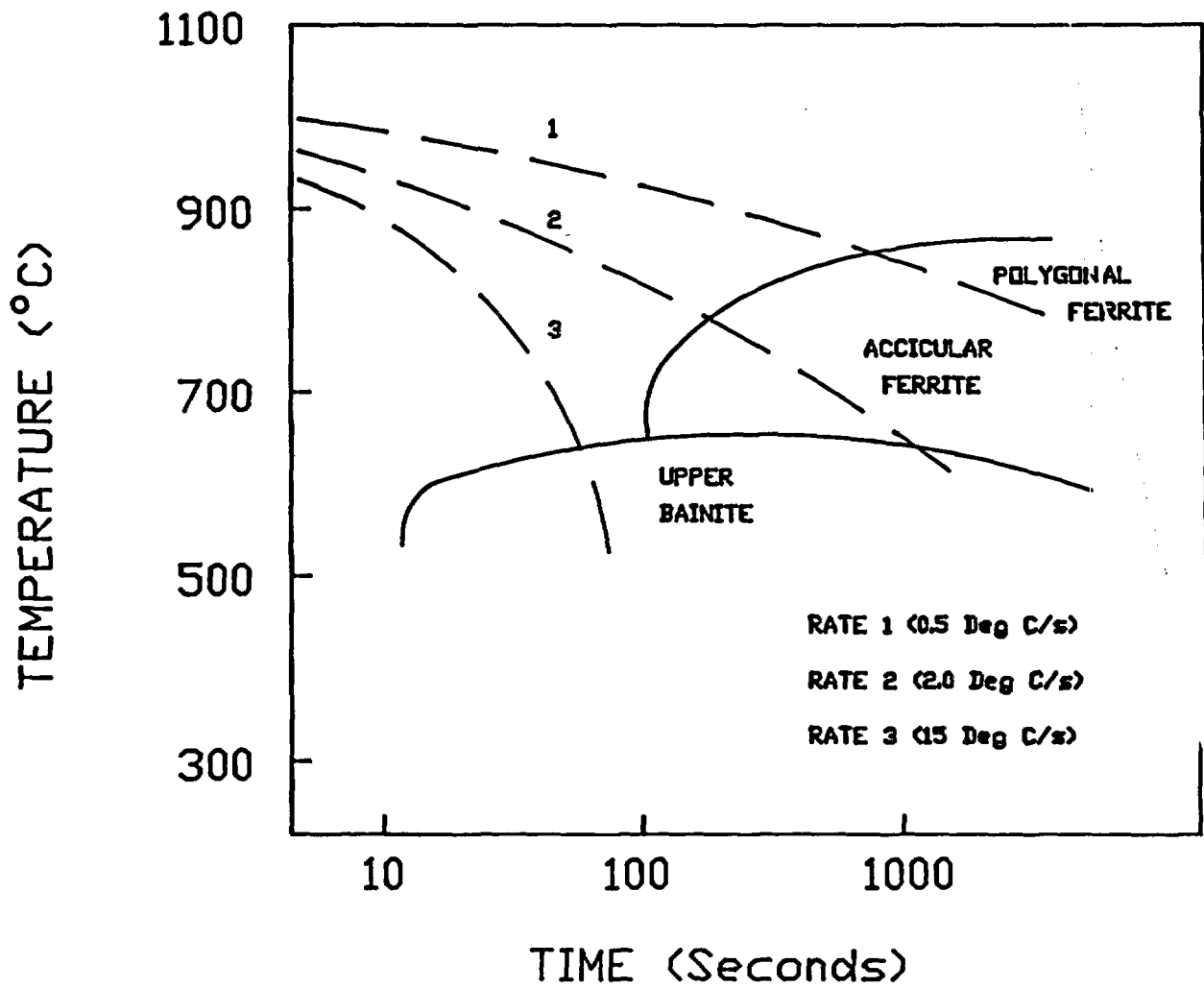


FIGURE 4. Schematic continuous cooling transformation diagram.

well below those at which the pearlite transformation normally takes place. Bainite is an extremely fine mixture of ferrite and carbides which is generally not resolvable by optical microscopy. Martensite is a metastable body centered tetragonal structure which forms from the face centered cubic austenite by a diffusionless isothermal transformation which starts at the  $M_s$  temperature indicated in Figure 4. Bainite and martensite microstructures have higher strengths and lower ductilities than pearlitic microstructures.

The presence of alloying elements (Cr, Ni, Mo, etc.) or tramp elements (O, S) tend to shift the curves on the CCT diagram to longer or shorter times. Alloy elements which increase the hardenability block the formation of pearlite along the grain boundaries and shift the C-curves to longer times. Large amounts of these elements may block the formation of pearlite for all but the slowest cooling rates, and result in the formation of a non-equilibrium bainitic or a martensitic structure. The tramp elements oxygen and sulfur (as oxide or sulfide inclusions) tend to promote the nucleation of ferrite or pearlite along the grain boundaries and shift the curves to the left to shorter times.

### 2.3 Corrosion Behavior

Extrapolation of known corrosion behavior to predict total corrosion degradation of steel waste containers after a 500 to 1,000 year exposure in a specific environment will require both the determination of the proper form for the corrosion rate expression and the corrosion rate coefficient. Existing general corrosion data is reported in mils per year (mpy) which makes an assumption of a constant corrosion rate. A constant rate is possible when the corrosion chemical action on the surface rather than mass transport of reactants to the surface is the dominating parameter. The linear (mpy) expression suggests that there are no corrosion products adhering to the surface, or if there were, they would serve as no barrier for the corrosion process. If there were adhering corrosion products it would be expected that a parabolic rate expression would be the anticipated form for such extended corrosion times. That is, the form would be given by:

$$\frac{dx}{dt} = \frac{K_1}{x - K_2 t} \quad (1)$$

where X is the section loss due to corrosion, t is the time of exposure and K<sub>1</sub> and K<sub>2</sub> are rate constants. If X >> K<sub>2</sub>t, that is at the early periods of the 500 to 1000 years of exposure then the expression becomes:

$$\frac{dX}{dt} = \frac{K_1}{X} \quad (2)$$

which gives a parabolic rate expression. But at a longer time when X-K<sub>2</sub>t is equal to K<sub>3</sub> then the expression becomes:

$$\frac{dX}{dt} = \frac{K_1}{K_3} = \text{Constant} \quad (3)$$

which describes a linear form. This linear form suggests that the attack on the metal/corrosion products interface is occurring at the same rate as the loss of the corrosion product at the corrosion product/environment surface. Evidence of parabolic corrosion behavior is seen in Figure 5 for both forged and cast steel (14). Figure 5 indicates a nonlinear corrosion rate behavior which approaches a constant corrosion rate at longer times. Similar concerns must be given to the rate expression describing localized attack (such as pitting) and environment cracking.

The estimate of the corrosion degradation of nuclear waste canisters after the 1000 years in the repository environment will also require a quantitative understanding of the environment. Ground water composition in granitic and argillaceous rock formations have been determined and a wide variety of ions were found to be present (14). These ions can be classified as aggressive ions such as Cl<sup>-</sup>, SO<sub>4</sub><sup>-2</sup>, and F<sup>-</sup>, or as passivating ions such as HCO<sub>3</sub><sup>-</sup> and CO<sub>3</sub><sup>-2</sup>. The concentration of these ions varied for the various sites and indicated that the pH could vary from 5.0 to 9.8. An example of the corrosion media for the various sites is given in Table 1 (15). Another potential corrosion environment for these ferrous waste containers is in brines. Some of the anticipated brine compositions are given in Table 2. Another environmental concern which is unique to a nuclear environment is the additional cathodic reaction due to the radiolytically generated oxidizing species. (16, 17).

With knowledge of potential corrosion environments, March, et al. (14) calculated E vs pH diagrams to indicate the various corrosion behaviors possible with environmental variations. They indicated on this activity diagram the compositional range of the various species to promote general corrosion. For various HCO<sub>3</sub><sup>-</sup>/CO<sub>3</sub><sup>-2</sup> ratios and chlorine ion concentrations three types of

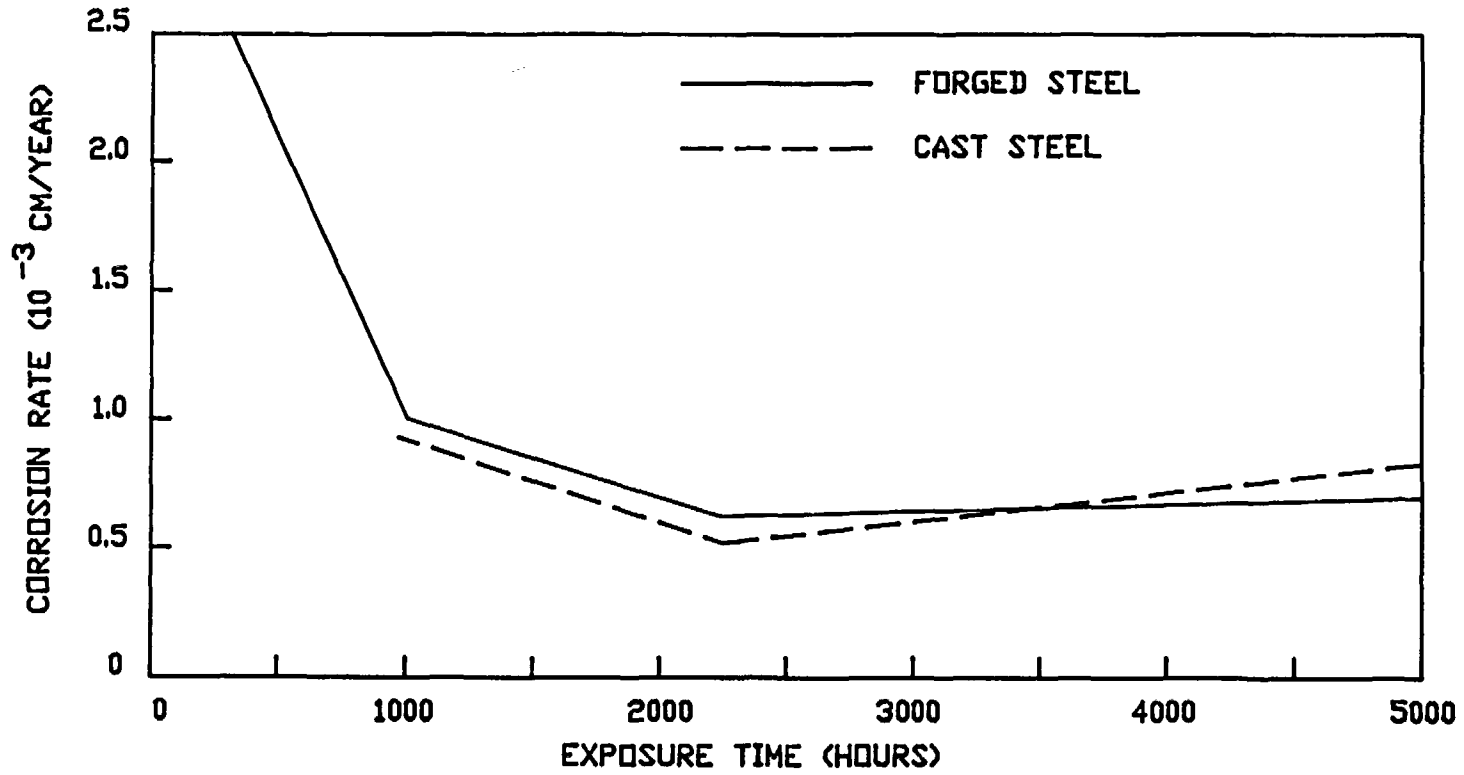


FIGURE 5. General corrosion rate vs. time for forged and cast steels immersed in de-aerated seawater at 90°C (14).

Table 1 - COMPARISON OF UNDISTURBED REPOSITORY PROPERTIES (15)

	Basalt	Tuff	Salt
<u>Rock</u>			
Thermal conductivity (W/m°C)	2.2	1.8	3.6
Thermal expansion coefficient (°C <sup>-1</sup> )	7x10 <sup>-6</sup>	4x10 <sup>-6</sup>	45x10 <sup>-6</sup>
Apparent porosity (%)	1	18	2
Maximum allowable temp. (°C)	300	300	250
Flow (m/yr pore velocity)	<1	<300	<0.01
<u>Fluid</u>			
pH	9.5	7.3	6.3
Eh (volts)	-0.5	0	-0.1
Dissolved silica (mg/l)	40	60	<0.01
Major anions (mg/l):			
HCO <sub>3</sub> <sup>-</sup> /CO <sub>3</sub> <sup>-2</sup>	80	120	900
Cl <sup>-</sup>	200	7	250,000
SO <sub>4</sub> <sup>-2</sup>	100	20	50
F <sup>-</sup>	30	2	<0.01
Major cations (mg/l):			
Na <sup>+</sup>	300	50	60,000
K <sup>+</sup>	10	5	5,000
Ca <sup>+2</sup>	2	15	80,000
Mg <sup>+2</sup>	0.05	2	10,000

TABLE 2 .- COMPOSITIONS OF BRINE SOLUTIONS (18):

	Brine A	Brine B
Na <sup>+</sup>	42,000	115,000
K <sup>+</sup>	30,000	15
Mg <sup>+2</sup>	35,000	10
Ca <sup>+2</sup>	600	900
Sr <sup>+2</sup>	5	15
Cl <sup>-</sup>	190,000	175,000
SO <sub>4</sub> <sup>-2</sup>	3,500	3,500
I <sup>-</sup>	10	10
HCO <sub>3</sub> <sup>-</sup>	700	10
Br <sup>-</sup>	400	400
BO <sub>3</sub> <sup>-</sup>	1,200	10

corrosion behavior were found. Stable conditions exist at highly negative potentials where passivity was achieved and the corrosion product serves as a barrier to further corrosion. General corrosion was found at less negative potentials, and pitting corrosion was found at less negative potentials and higher pH levels. No evidence for passivation was found when the  $\text{HCO}_3^-/\text{CO}_3^{2-}$  ratio was less than 0.0001M.

Cramer and Carter (18) have reported that the weld area of AISI 1020 carbon steel, including the heat affected zone, corrode faster than the non-weld areas. The regions of the heat affected zone corrode at a rate of 125 mpy compared to 25 mpy for the non-weld regions of the specimen. They also reported variations in the corrosion rate of the weld metal depending on selection of the cover electrode. The deposit of E7016 rod corroded at a high rate of 920 mpy while deposits of E6011, E6012 and E7018 corroded at rates similar to the non-weld AISI 1020 material. Heat treating the deposits made by E7016 and E7024 rods promotes low weld corrosion rates. In oxygenated brine the difference in the corrosion rate of the weld and non-weld carbon steel was not significant, because both materials had high general corrosion rates.

Pitting corrosion was shown to be possible for low carbon steels in some ground water conditions. Pitting is the result of localized passive film break down and will occur under conditions represented by the passive regions of the E vs. pH diagram (19). Pitting is characterized by a delay time prior to pit growth. The pits usually grow in the direction of gravity, and their growth usually accelerates with time. The pitting is the result of a concentration cell in which the saturated solution in the pit is different than the solution associated with the surfaces. The potential in the pit is different from that at the surface. The deeper the pit, the more saturated the solution in the pit and the potential difference is greater. This potential difference promotes a cell in which the pit bottom is the anode. The number of pits is not a significant variable, for the integrity of the waste canister is lost with only one pit that has grown across the canister section thickness.

Romanoff (20) investigated pitting in carbon steels in soils at approximately 10°C-20°C to determine the empirical rate expression. He assumed the following form:

$$P = 0.746 t^{0.37} \quad (4)$$

where P is the maximum pit depth in mm and t is the time in years. Marsh et.al. (14) conducted pitting experiments in 0.1 M NaHCO<sub>3</sub> + 1000ppm Cl<sup>-</sup> solution with a pH of 8.4 and a temperature of 90°C. Their expression for growth of the maximum pit depth is given by:

$$P = 3.19 t^{0.485} \quad (5)$$

This expression was reported to give a maximum penetration of 91 mm over 1000 years; whereas the Romanoff expression was at a lower temperature would predict 9.6 mm for the same length of service. The fact that the literature indicates two different scale laws suggests that there are insufficient data as functions of time, temperature and environmental conditions to make long term prediction of pitting damage. Harrar et. al.(21) and Carter et.al (22) have reported the pitting corrosion behavior of low carbon steel in geothermal brines. Geothermal brines may be an excellent source of supplementary corrosion data for nuclear waste canisters in salt repository situations.

#### 2.4 Microstructural Alteration During Repository Storage

The microstructures generated during the casting and welding processes encountered in manufacturing may be modified by exposure to the thermal experience of repository storage. This thermal experience will vary with container and repository design, and waste form. Sustained temperatures in the range of 200-300°C are possible for periods of up to 50 years with some designs. The microstructural changes caused by the thermal experience will be the result of thermally activated processes such as: (a) carbon and alloy element diffusion; (b) grain growth and the movement of grain boundaries induced by capillarity or surface tension forces; (c) changes in the shape, size, and distribution of secondary phase particles such as carbides, nitrides, sulfides or oxides; and (d) changes in defect structures related to vacancies and dislocation substructures.

Microstructural changes are expected to be the most pronounced in the fusion and heat affected zones of the welds used to close the ends of the overpack container. The final closure weld, in particular, will not receive post weld heat treatment, and it will leave residual stresses and non-equilibrium microstructures which are expected to be modified by thermally activated processes. The influence of these thermally activated modifications were studied by subjecting submerged arc weld specimens to high temperatures for short "equivalent time". Based on kinetic arguments for thermally activated processes, this thermal experience is expected to duplicate the microstructural effects of long term repository storage.

## 2.5 Casting Processes

### 2.5.1 Process Variables and Process Control

An analysis of the structure and properties of a cast overpack container requires a careful consideration of the nature of the independent and dependent variables that are involved in the melting and solidification processes. The independent process variables include: (a) the chemical process variables which control the ladle composition, (b) the heat transport and fluid flow variables which influence solidification of the casting, and (c) the heat treatment variables which control austenite decomposition and the final heat treated microstructure. The dependent variables are controlled by heat transport and by the nature of solidification of the alloy. These include: the solidification velocity, the nature and coarseness of the solidification structure, and the degrees of microsegregation and macrosegregation.

The melting and refining process variables which control composition and cleanliness include: charge material selection, slag chemistry, atmosphere control, ladle treatment including degassing and deoxidation practice, and alloy element additions. Steel melting for large castings is generally accomplished using the electric arc furnace or the coreless induction furnace.

Specialty grades of steel such as stainless alloys are sometimes produced using the Argon Oxygen Decarburization Process (AOD). The thermochemistry of iron and steel making and descriptions of the various steelmaking processes are found in references (5, 23-37). The independent variables which control the solidification structure and properties include: casting size and geometry, riser design and placement, mold design and thermal properties, gating design, and the use of directional solidification or centrifugal casting techniques to change solidification or feeding characteristics. The nature of the solidification process can be placed in one of several categories depending on the location of the heat choke or the primary resistance to heat flow. For sand castings the primary resistance to heat flow is in the mold, for die castings the major resistance is at the mold metal interface; and for teemed ingots heat flow barriers exist at both the mold-metal interface and the solidified portion of the ingot. Analytic solutions exist for these three cases which provide the temperature distribution, solidification velocity, and thickness solidified as functions of time and distance from the mold-metal interface. General descriptions of solidification processes are provided in references (6, 7, 8, 10, 11, 38-47). Many of these references are texts which are designed for solidification or foundry courses in metallurgy curricula. References (48-60) deal with specific aspects of solidification important to cast waste containment vessels. The final set of independent process variables involve heat treatment. Castings are generally normalized to relieve residual stresses, and high strength steel castings are generally quenched and tempered to maximize strength and toughness. Other heat treatments may involve high

temperature homogenization to relieve microsegregation, annealing for the purposes of cutting, or more complicated heat treatments for purposes such as precipitation hardening.

The dependent variables in the casting process involve fluid flow, solidification velocity, solidification structure, and the degrees of microsegregation and macrosegregation. The pouring time, aspiration, and turbulence are controlled by the design of the gating system. The solidification velocity is controlled by the rate of heat extraction by the mold. The local solidification time is a measure of the total time over which solidification takes place at any particular point in the casting. It controls the secondary dendrite arm spacing and is controlled by the solidification velocity, by the width of the freezing range between the liquidus and solidus temperatures on the equilibrium phase diagram, and by the thermal gradient at the solid-liquid interface. The dendrite arm spacing has a major influence on the high temperature soaking time required to homogenize the cast structure. The degree of microsegregation or coring between the dendrite arms is controlled by the alloy composition and by the phase diagram; and it is relatively independent of the solidification velocity. The Scheil equation or non-equilibrium lever rule, can be used to predict the concentration of a particular alloy or tramp element as a function of the fraction solid and the initial composition of the alloy. Variations in composition over large distances are termed macrosegregation, and are caused by the flow of solute rich or solute depleted liquid within the mushy zone between the solidus and liquidus isotherms. Macrosegregation is influenced by alloy composition, solidification velocity, casting geometry, and by the width of the mushy zone. The types of macrosegregation include surface or centerline segregation, channel segregates or freckles, and banding. Macrosegregation can be strongly influenced by solidification processing variables.

The chemical composition, structure, and homogeneity of castings may be varied through the use of a number of process control techniques. These include: chemical analysis combined with alloy additions or refining, temperature measurement, and the use of casting techniques to promote directional solidification or enhanced feeding. Precise alloy compositions require a thorough analysis and control of charge ingredients, a precise charge calculation combined with empirical knowledge of melting losses, and control of slag chemistry and refining techniques. An on line chemical analysis using an emission spectrometer helps to make certain that the heat is tapped with the correct chemical analysis. Control of temperature and solidification variables is maintained through the use of immersion thermocouples, and by various techniques for modifying the heat transport conditions during solidification. Temperatures within the solidifying casting can be measured by placing thermocouples within the mold cavity for experimental castings, and the thermal data obtained by this method may be used to modify the geometry or heat transport properties of the mold.

## 2.5.2 Chemical Control During Melting Processes

The quality of steel alloys produced in the electric furnace is strongly influenced by the choice of scrap and by the nature and extent of the refining that can be accomplished. Direct arc furnaces are typically used for heats ranging from 5 to 300 tons. Melting is accomplished by a direct arc between the electrodes and the charge, and the high temperature of the slag that covers the melt provides excellent refining capabilities. The coreless induction furnace provides efficient melting for steel heats up to about 25 tons. Traditional refining techniques based on a high temperature slag are limited because of the danger of eroding the thin furnace lining, and because the slag does not suscepr to the magnetic field and is not heated. Ladle refining techniques, however, can be used to change the alloy content or to refine tramp elements. The cleanliness of steel produced by a coreless induction furnace is controlled by the quality of the scrap and alloy additions, and by the extent of refining and atmosphere protection.

Most foundries producing high quality steel castings formilitary, aircraft, or naval applications purchase high quality scrap for melting. This limits the sulfur, phosphorus, tin, and other tramp elements. High quality scrap may be obtained from sources such as punchings from structural sections, scrapped rails, and bar stock which is produced by the continuous casting process from primary pig iron. The use of bar stock is preferable because of its controlled and constant chemistry, but the price is much higher. The use of low grade scrap such as that from automobile bodies will result in significant problems with tramp elements such as copper, nitrogen, and tin.

Induction furnace melting practice is covered in references 30, 33, 35 and 36. The charge is packed as tightly as possible into the furnace without damaging the lining, and maximum power is used until melting is complete. After meltdown the slag is removed, and alloy elements which are not readily oxidizable such as nickel and molybdenum are charged. These may also be charged cold before the start of melting. Carbon is added using low silicon pig iron, and the rate of pig iron addition is controlled such as to achieve a vigorous carbon boil of at least a 5 minute duration. This helps to remove hydrogen and some of the nitrogen. The heat is generally blocked by a ferrosilicon addition after the carbon boil is completed in order to achieve constant carbon losses. After the tapping temperature has been reached and the slag removed, the balance of the ferrosilicon and the ferromanganese are added. The heat is tapped shortly after of the ferromanganese addition in order to limit manganese losses by vaporization. An aluminum kill of 0.05 to 0.07 wt.% is charged to the stream after about one third of the heat has been tapped.

Electric arc furnaces are designed to produce heats ranging from one ton to as much as 300 tons. They are very efficient and are capable of significant refining of the metal because the arc from the overhead electrodes heats the slag. Melting practice for the

electric arc furnace can be designed to reduce tramp elements such as sulfur and phosphorus, but the metallic tramp elements such as copper and tin remain a significant problem. Electric arc furnace melting practices are covered in references 27, 28, 30, 31, 32 and 34. The highest quality steel is produced using a double slag melting practice. A basic, oxidizing slag is used first to oxidize carbon, silicon, and manganese and to refine phosphorus. This slag is then removed from the process so that the phosphorus will not revert, and a basic reducing slag is formed by adding hard burnt lime, calcium fluoride, and carbon in the form of crushed electrodes. This basic reducing slag removes sulfur, prevents oxygen pickup, and protects against oxidation losses of alloy elements. The control of gaseous impurities is a significant consideration for all electric steel making practices (26-29, 36, 41 and 42). The gasses which can cause problems include hydrogen, nitrogen, and oxygen in the form of carbon monoxide. Oxygen can be removed to low levels by deoxidation with silicon and manganese followed by killing with aluminum. This can yield dissolved oxygen contents as low as 10 ppm. and total oxygen contents which includes oxide inclusions of 50 to 100 ppm. Hydrogen and nitrogen must be removed mechanically by means of a carbon monoxide boil, by sparging, or by vacuum treatment. Hydrogen can be effectively removed by any of these methods, but nitrogen presents a problem because surface active oxygen and sulfur prevent nitrogen from crossing the interface into the bubble. Thus, nitrogen is never removed to a satisfactory extent, and it tends to build up in steel scrap. The electric melting practices which yield the highest quality utilize a carbon boil during the progress of the heat combined with vacuum treatment at the time of tapping. This can consist of placing the whole ladle in a vacuum chamber or of vacuum stream degassing at the time the furnace is tapped into the ladle. Vacuum treatment of the entire ladle is difficult because of problems with nucleation of gas bubbles at depths below the surface greater than about 6 inches. Vacuum stream degassing is more successful because gas bubbles can nucleate and grow to critical size while falling in the stream from a tundish into an evacuated ladle.

Deoxidation practice is an important consideration in controlling steel quality and cleanliness. Cast steels are generally dead killed with aluminum in order to prevent rimming or a carbon monoxide boil during solidification and the resulting gas porosity. A maximum of 0.05 to 0.07 wt. % aluminum should be used for deoxidation, because higher aluminum contents of around 0.1 wt.% can lead to problems with aluminum nitride formation and rock candy fracture.

### 2.5.3 Heat Transport and Solidification Structure

The independent process variables which control the solidification structure involve heat transport and the design of the casting. References 6, 7, 8, 10, 11, 44-56 provide general information on heat transport and solidification. Solidification is controlled by the shape and size of the casting and by the heat extraction capabilities of the mold. The rate of heat

extraction by the mold is a function of the thermal conductivities and specific heats of the casting alloy and the mold material, and of the boundary heat transport coefficient between the metal and the mold.

Several casting processes are available for castings the size of the proposed overpack containers. These include: sand casting, permanent or semi-permanent mold casting, centrifugal casting, and solidification in water cooled copper molds. Sand molds are considered to be insulating. Their heat transport behavior can be modeled based on the assumption that the heat choke is in the mold and there is little resistance to heat transport in the solidified metal or at the mold/metal interface. Semi-permanent and permanent molds are constructed of graphite, silicon carbide, or gray iron as in the case of ingot molds. These provide a much greater rate of heat extraction than is available from sand molds, and analytical solutions for solidification behavior in these molds require a different set of assumptions and boundary conditions. Water cooled copper molds such as those used in vacuum arc or electroslag remelting provide the most rapid heat extraction. In this case the solidification velocity can be considered to be linear within the first few inches of the mold wall. Centrifugal castings are produced in a rotating steel mold with a sand lining. Heat transport is slower across the sand lining, but the fluid flow along the solid liquid interface and the high centrifugal force provide excellent feeding and a refined microstructure.

Solidification in insulating molds such as sand molds may be modeled based on an analytical solution referred to as Chvorinov's Rule (6, 8, 45, 47, 57). This solution is based on the assumptions of uni-directional heat transport, a semi-infinite mold, and the assumption that the heat choke is in the sand rather than in the metal or at the mold-metal interface. In one dimension the partial differential equation for unsteady heat transport is:

$$\frac{\partial^2 T}{\partial x^2} = \frac{1}{\alpha} \frac{\partial T}{\partial t} \quad (6)$$

where:

- $\alpha$  =  $K/\rho c$  = thermal diffusivity ( $\text{cm}^2/\text{s}$ )
- $\rho$  = density ( $\text{gm}/\text{cm}^3$ )
- $c$  = specific heat ( $\text{cal}/\text{gm}^\circ\text{C}$ )
- $k$  = thermal conductivity ( $\text{cal}/\text{cm.s.}^\circ\text{C}$ )

Two initial conditions and two boundary conditions are given as follows:

Initial Conditions:

- (1)  $T(+x, 0) = T_o$             Initial Mold Temperature  
 (2)  $T(-x, 0) = T_e$             Zero Superheat

Boundary Conditions:

- (1)  $T(0, t) = T_e$             Constant Surface Temperature  
 (2)  $T(X, t) = T_o$             Semi-Infinite Mold

where:  $T_e$  = Equilibrium Melting Point of the Alloy  
 $T_o$  = Ambient Temperature

At the instant of pouring ( $t = 0$ ) the mold is at ambient temperature  $T_o$  and the metal is at the equilibrium melting point  $T_e$ . At some later time ( $t > 0$ ) when a solidified layer of thickness ( $x$ ) has formed, the surface of the casting is still assumed to be at  $T_e$ , but the mold has absorbed heat raising its temperature. The solution of equation 6 subject to the initial and boundary conditions provides the temperature in the sand mold as a function of distance from the mold metal interface ( $-x$ ) and the time after the instant of pouring ( $t$ ):

$$T = T_m + (T_o - T_m)\text{erf} (x/2) (\alpha t)^{\frac{1}{2}} \quad (7)$$

where:            erf = error function

The solidification velocity ( $R = dx/dt$ ) is determined from equation 7 using an energy balance at the mold-metal interface which equates the rate of latent heat release with the heat flux into the mold at the mold surface. The heat flux at the mold surface ( $Jx$ ) is expressed using Fourier's Law which gives the flux as the negative product of the thermal conductivity and the thermal gradient:

$$Jx = 0 = K_{\text{mold}} \frac{dT}{dx} = -\rho HR \quad (8)$$

where:  $R$  = solidification velocity (cm/sec)  
 $H$  = heat of fusion (cal/gm)

An expression for the thermal gradient at  $x=0$  is obtained by differentiating the solution for the temperature field in the mold with respect to time. Substitution of this differential into equation 8 and solution for the solidification velocity gives an expression for the solidification velocity as a function of the temperature difference between the melting point and the

ambient temperature, the thermal properties of the mold and metal, and the time elapsed since pouring:

$$R = \frac{(T_m - T_o) (K_S \rho_S C_S)^{\frac{1}{2}}}{\rho_H (\pi t)^{\frac{1}{2}}} \quad (9)$$

where:  $K_S$ ,  $\rho_S$ ,  $C_S$  = thermal constants of the sand

The solidified thickness ( $X$ ) is determined as a function of time by separating the variables in equation 9 and integrating from  $x = 0$  at  $t = 0$ . The resulting expression gives the solidified thickness as a function of the square root of time:

$$X = \frac{2}{(\pi)^{\frac{1}{2}}} \frac{(T_m - T_o)}{\rho_H} (K_S \rho_S C_S)^{\frac{1}{2}} (t)^{\frac{1}{2}} \quad (10)$$

In order to apply the results to three dimensional castings and ingots Chvorinov substituted the volume to surface area ratio of the casting for the thickness solidified. Thus, the solidification time for a casting can be expressed as a constant times the square of the volume to surface area ratio:

$$t_f = C^2 (V/A)^2 \quad (11)$$

The solidification of teemed ingots, of castings in semi-permanent molds such as silicon carbide or graphite involves thermal gradients in both the mold and the solid metal. When no barrier to heat transport exists at the mold-metal interface the progress of solidification and the temperature fields in the mold and casting may be modeled by Schwartz's Solution (6, 45, 57). This solution can also be applied to the solidification of welds by considering the parent plate to be the mold.

Schwartz's solution assumes that the mold and metal are both semi-infinite and that heat transport is unidirectional. Further, it is assumed that perfect thermal contact exists between the mold and the metal, and that the temperature at the mold-metal interface is constant. The solution is based on two initial conditions and four boundary conditions:

### Initial Conditions

- (1)  $T(-x, 0) = T_0$  Initial Mold Temperature.
- (2)  $T(x, 0) = T_m$  Zero Superheat

### Boundary Conditions

- (1)  $T(0, t) = T_s$  Constant Interface Temperature
- (2)  $T(x, t) = T_m$  Equilibrium at the Solid/Liquid Interface
- (3) Heat Balance at the Mold-Metal Interface
- (4) Heat Balance at the Solid-Liquid Interface

Two solutions are obtained: one for the temperature field in the mold as a semi-infinite solid, and one for the metal as a semi-infinite solid. The application of the initial and boundary conditions provide three equations which are sufficient to solve for the desired variables:

$$\frac{(T_m - T_0) C_1}{H(\pi)^{\frac{1}{2}}} = \beta e^{\beta^2} \left[ \operatorname{erf} \beta + \frac{K_1 \rho_1 C_1}{K \rho c} \right] \quad (12)$$

where:  $\beta$  = constant  
 $T_m$  = melting point  
 $T_0$  = ambient temperature  
 $k_1, \rho_1, c_1$  = thermal constants for the metal  
 $k, \rho, c$  = thermal constants for the mold

$$\frac{(T_m - T_s) C_1}{H(\pi)^{\frac{1}{2}}} = \beta e^{\beta^2} \operatorname{erf} \beta \quad (13)$$

$$S = 2\beta(\alpha, t)^{\frac{1}{2}} \quad (14)$$

Equation 12 is used to solve for  $\beta$  the constant argument of the error function. The solution may be carried out graphically or by trial and error. Equations 13 and 14 are used to solve for the constant surface temperature, and for the thickness of the solidified layer,  $S$ , as a function of time. The foregoing equations may be useful in predicting the degree of alloy segregation during casting.

#### 2.5.4 Segregation and Casting Defects

The defects associated with casting processes used to produce overpack containers are an important consideration for the present study. Casting defects may include defects related to the mold, defects related to the design of the casting, and defects related to the alloy composition. Mold related defects include: shifts and dimensional variations caused by inaccuracy

in the mold, blow holes or other moisture related defects caused by wet sand; defects such as rat tails, buckles, and cope spallation related to thermal expansion and/or failure of the mold; and hot tears, cold cracks, and other failures related to mold restraint of the casting. Defects related to casting design include: shrinkage porosity caused by inadequate risering or feeding; miss runs, hot spots, or cold shuts caused by inadequate riser design or insufficient fluidity; hot tears or cracks caused by poor casting design; and problems with core floating, chaplets, or fusion of the core surface caused by incorrect core design. Defects related to alloy composition include microsegregation, macrosegregation, blow hole porosity or other gas related defects, and non-metallic inclusions which can be related to metallurgical failures.

It is estimated that use of the centrifugal casting process to produce the overpack container castings will minimize or bypass many of the above defects. Centrifugal casting will eliminate the need for a riser, provide high feeding forces, eliminate the need for the use of cores, eliminate defects related to expansion or moisture in sand molds, and remove nonmetallic inclusions, etc., by the centrifuging action. The three potentially most damaging casting defects related to the centrifugal casting process are the formation of cold shuts caused by splashing and freezing of molten metal on the mold wall, the formation of longitudinal hot tears caused by the hoop stresses on the outer surface of the casting as it cools and contracts away from the mold wall, and segregation related defects such as microsegregation and macrosegregation which are related to solidification processes. Pure materials can be solidified at their melting points with a planer solidification front, but if the melt is thermally undercooled below the equilibrium melting point the planer interface will break up to form dendrites. Commercial alloys containing two or more elements may solidify with a plane solidification front if the alloy is very dilute and a very large thermal gradient is present at the solid/liquid interface. These conditions are present in single crystal growing processes, however, the presence of solutes and the small thermal gradients present in commercial casting and welding processes lead to cellular or dendritic solidification and to the segregation of the solute elements (8, 45, 46, 49-54).

The segregation of alloy or tramp elements on a microscopic scale between dendrites is referred to as "microsegregation", and the segregation over larger distances caused by the flow of solute enriched or solute depleted liquid is termed "macrosegregation". Microsegregation results from the difference in solute solubility between the liquid and solid phases and by the lack of equilibrium caused by low solute diffusivity in the solid. Solute segregation to the liquid or solid occurs during solidification, and this segregation is fixed because of the low solid diffusivity. Microsegregation is difficult to avoid in commercial casting and welding processes, but the composition differences can be altered somewhat by diffusion during high temperature heat treatments. Ingots are generally soaked at the hot working temperature for a number of hours before rolling to

homogenize the composition gradients. Some microsegregation will, however, remain even after extensive thermal processing.

Macrosegregation over large distances in the casting or ingot is considerably more damaging. It may take the form of banding, surface or centerline segregation, or the formation of channel segregates. and it may result in scrapping of the product. Therefore, the avoidance of solidification conditions or alloys in which macrosegregation is likely to occur is a must for the production of cast overpack containers. The extent of microsegregation may be estimated by the Scheil Equation or "Non-Equilibrium Lever Rule" (45, 46, 54, 55), which is based on a solute balance at the solid/liquid interface, and on the assumptions of: equilibrium at the interface, complete diffusion in the liquid, and no diffusion in the solid. The Scheil equation may be written to express the composition of the solid or liquid at the interface as a function of the fraction solid or liquid, the initial composition of the melt, and the equilibrium partition ratio of the solid composition to the liquid composition given by the ends of the tie lines across the two phase region of the phase diagram.

$$C_l = C_o f_l^{k-1} \quad (15a)$$

$$C_s = kC_o(1-f_s)^{k-1} \quad (15b)$$

where:  $C_l, C_s$  = liquid and solid compositions at the interface.  
 $C_o$  = initial liquid composition.  
 $k$  = equilibrium partition ratio.  
 $f_l, f_s$  = fractions of liquid and solid.

The volume fraction of eutectic present after solidification is complete can be estimated by solving for the liquid fraction remaining when the liquid composition reaches the eutectic composition. Calculations for systems such as the iron-sulfur system show that a small amount of eutectic is formed even when the initial concentration in the melt is small and within the solid solubility limit. In the absence of manganese to form manganese sulfide, a small amount of sulfur is sufficient to form the iron-sulfur eutectic along the grain boundaries, and cause severe ductility problems. Expressions similar to the Scheil equation can be derived to account for limited diffusion in the liquid, convection in the liquid, diffusion in the solid, or other conditions. Macrosegregation is more difficult to deal with analytically, because it involves both microsegregation and fluid flow problems. Analytical expressions have been derived for several types of macrosegregation including: banding, under-riser segregation in castings, channel segregates in ingot

solidification, and others (45, 53, 61-64). In general, these solutions show that no macrosegregation occurs when the direction of interdendritic fluid flow is parallel to the direction of isotherm movement, and the fluid flow velocity is equal to the flow necessary to feed shrinkage:

$$\frac{v}{u} = - \frac{\beta}{1-\beta} \quad (16)$$

where:  $v$  = interdendritic fluid flow velocity.  
 $u$  = isotherm velocity.  
 $\beta$  = solidification shrinkage.

For alloy systems in which the equilibrium partition coefficient is less than one the solute segregates to the liquid during solidification. If the velocity of the solute enriched liquid is greater than that required to feed shrinkage negative macrosegregation will result, and if the flow velocity is less than that required to feed shrinkage positive macrosegregation will result.

## 2.6 Welding Processes

### 2.6.1 Welding Process Variables and Process Control

Closure of the ends of the overpack containers will most likely be accomplished by welding end caps in place using arc welding techniques. These welds must be free from defects which would lead to possible failure of the overpack during long term storage. Submerged arc welding is a good candidate for weld closure of the first end, because the process offers the advantage of a high deposition rate and good process control, and the slag can be chipped off between passes. The closure of the second end after placement of the waste must be accomplished remotely because of the high level of radiation. The gas metal arc welding process is a good candidate for closure of the second end, because it can be remotely controlled, and there is no slag to chip between passes. Conventional arc welding power supplies are of constant potential design. The arc length is held approximately constant, and the welding current is controlled by the electrode velocity. The current, welding potential, and electrode velocity influence a number of weld characteristics such as the transfer mode, penetration, melting rate and arc stability. For this reason it is desirable to consider the independent and dependent process variable and the functional relations between them. This will allow better process control.

Welding process variables are discussed by Lancaster (65, 66), by Easterling (67), and by the American Welding Society (68, 69). An investigation of gas metal arc welding process variables by Frost and Vaughan (70) showed that the process variables may be classified as either independent and dependent based on the

possibility of direct machine control. The independent variables can be defined as parameters set on the welding machine. These independent variables include:

$V_O$  - Open Circuit Potential  
 $W$  - Electrode Velocity  
 $S$  - Weld Travel Speed  
 $A_W$  - Electrode Cross Sectional Area  
 $G$  - Distance between the Contact Tube and the Work

The cross section of the electrode is generally held constant for a particular welder. The distance between the contact tube and the work is often neglected as an independent variable. The dependent process variables are controlled by the choices of the independent variables above. The dependent variables include:

$V$  - Arc Potential  
 $I$  - Welding Current  
 $A_R$  - Reinforcement Cross Section  
 $H$  - Heat Input

The welding potential ( $V$ ) in gas metal arc welding is a linear function of the welding current controlled by the machine characteristic or droop of the power supply (70):

$$V = V_O - c(I) \quad (17)$$

where:  $c$  = machine constant

The welding current was found to be approximately independent of the voltage and a linear function of the electrode velocity:

$$I = a + b(W) \quad (18)$$

Where ( $a$ ) and ( $b$ ) are machine constants. The current may also be influenced by the electrical resistivity of the electrode where this is different from that of carbon steel.

The reinforcement area  $A_r$  is equal to the product of the electrode cross sectional area and the ratio of the electrode velocity to the weld travel speed:

$$\frac{W}{S} (Aw) \quad (19)$$

The heat input per unit length of weld (H) is the product of an arc efficiency ( $\eta$ ) times the product of the current and potential divided by the weld travel speed:

$$H = \eta (VI/S) \quad (20)$$

The arc efficiency ( $\eta$ ) ranges from 90 to 99% for submerged arc welding and from 66 to 85% for the gas metal arc welding process (65). The heat input controls the superheat in the deposited weld metal, the extent of melting of the base plate, the rate of solidification of the fusion zone, and the thermal history of the heat affected zone. Equations 17 through 20 may be combined to yield an expression for the electrode velocity as a function of the reinforcement cross section, the heat input, and the constants in equations 17 and 18:

$$W^2 + \{(HA_w/cb^2A_r) + Z\}W + Y = 0 \quad (21)$$

where:  $Z = 2a/b - V_o/cb \quad (22)$

$$Y = a - V_o/c + a/b^2 \quad (23)$$

The electrode velocity calculated from equation 21 can be used to determine the current, potential, and weld travel speed required to produce a given weld reinforcement cross sectional area and heat input per unit length.

### 2.6.2 Welding Consumables

Since welding consumables are selected and purchased by very broad specifications established by the Welding Industry, it is essential that the fabricators of nuclear waste containers be aware of some of the physical behavior of these consumables. To fully understand the relationship between the selection of welding consumables and their use, and the attainability of an acceptable weldment many cause-and-effect relationships need to

be considered. This level of understanding will be even more important for automatic welding systems for remote closing of the overpack containers. Three categories of welding consumables need to be examined for this study: the electrode or filler metal, the flux for the case of submerged arc welding, and the cover gas for gas metal arc welding.

#### 2.6.2.1 Submerged Arc Consumables

Welding electrodes for submerged arc and gas metal arc welding are specified by the American Welding Society in Chapter 94, Vol. 5, of the 6th Edition of the Welding Handbook (71), and in Volume 6, ASM Metals Handbook, 9th Edition (72). The fundamentals of welding processes are covered in Volume One of the Seventh Edition of the Welding Handbook (68), and the particulars of the various welding processes are covered in Volume Two (69).

Electrodes and fluxes for submerged arc welding of carbon and low alloy steels are covered in AWS Specifications. Electrodes for welding carbon steels are classified according to composition in AWS Specification A5.17-80. Electrodes are grouped into low, medium, and high manganese contents; and the carbon, silicon, and tramp element contents specified within each group. Electrodes for welding low alloy steels are grouped according to alloy element groupings in AWS Specification A5.23-80. The alloy groupings include carbon-molybdenum, chromium-molybdenum, nickel, and other alloys.

Fluxes for submerged arc welding are classified on the basis of the ultimate tensile strength, the Charpy impact toughness of the weld metal, and the heat treated condition for which the mechanical properties are obtained. The flux types are classified based on the constituents and on the basicity index which is the ratio of the sum of the weight fractions of basic oxides plus calcium fluoride ( $\text{CaO}$ ,  $\text{MgO}$ ,  $\text{MnO}$ ,  $\text{FeO}$ , etc.,  $\text{CaF}_2$ ) to the sum of the weight fractions of the acid oxides ( $\text{SiO}_2$ ,  $\text{TiO}_2$ ,  $\text{Al}_2\text{O}_3$ , etc.). The composition groups include: manganese silicates, calcium silicates (acid, neutral, and basic), alumina based, and fluoride ( $\text{CaF}_2$ ) based (72).

Submerged arc welds are produced under a molten flux cover which shields the weld metal from the atmosphere, contributes to the stability of the welding process, and influences the composition and cleanliness of the weld metal. Therefore, the choice of flux has a major influence on the welding process. Three major flux characteristics will be considered in the present discussion: the viscosity, the influence of the flux on arc stability, and the pyrometallurgical behavior of the flux as it influences the composition of the weld metal.

The viscosity of a welding flux is one of its most important physical properties. The flux must be fluid enough to allow the transfer of elements between the flux and metal and allow gasses to escape. Small additions at the concentration levels common for residuals in mineral based fluxes may promote sufficient change to degrade the designed performance of the flux.

Typical welding flux viscosities at 1400°C are of the range of 2-7 poise (73). The flux must be fluid enough so that it flows to cover the weld pool, but viscous enough that it does not run away from the molten metal and flow in front of the arc, leading to possible overlapping of the weld metal. Viscosity of the flux is a very important concept for out-of-position welding. Flux viscosity is a strong function of temperature. If the flux viscosity at 1450°C is above 7 poise, there is a definite increase in the susceptibility of weld surface to pocking, which has been associated with the presence of easily reducible oxides in the flux. The oxide is reduced, and the oxygen reacts with carbon to form carbon monoxide which can not be transported through a more highly viscous flux and is trapped at the liquid metal/flux interface, forming surface defects. Flux viscosity is also strongly influenced by the SiO<sub>2</sub> content. The high SiO<sub>2</sub> or other network forming oxides are polymeric or glassy in nature and have high viscosities. Basic fluxes which are high in the basic oxides such as CaO or MgO are ionic in nature and have low viscosities.

Fluxes stabilize the arc in submerged arc welding by providing easily ionizable elements for the arc atmosphere, and by influencing electronic behavior at the anode and the cathode spots. Early research (74, 75) suggests that fluxes made up of easily ionized compounds produced better arc stability; however, much of this work was done using single component fluxes and the results are not applicable to more complex systems.

Arc instability has been defined as the deviation in arc voltage from the set welding voltage. It has been reported (76) that additions with greater ionization potentials provide more stable arc welding stability. These results indicate that arc stability is probably controlled more by the electrode spots than by interactions in the plasma. Weld metal oxygen content has been reported to influence the nature of the cathode spot and thus arc stability (77). Increasing the weld metal oxygen content increases the oxygen or oxide content on the weld pool surface which is suggested to lower the work function at the cathode spot. The welding arc instability is also a function of the parent metal composition.

The chemical behavior of fluxes during arc welding has been studied by a number of investigators (73, 78-83). Studies have been undertaken to predict the weld metal composition by applying pyrometallurgical thermodynamic concepts based on the assumption of the existence of a pseudoequilibrium state (83, 84, 85). The concern over the weld metal oxygen and carbon content has become of primary interest. The concept of basicity to describe the refining behavior of a slag is generally used and accepted in the iron and steelmaking industries. It is related to the classification of oxides into acid oxides and basic oxides depending on their capacity of forming or breaking anion

networks. The most commonly used basicity index formula, BI, in welding metallurgy, was proposed by Tutiani, Boniszewski, and Eaton (78):

$$BI = \frac{CaO + MgO_2 + CaF_2 + K_2O + Na_2O + Li_2O + 1/2(MnO + FeO)}{SiO_2 + 1/2(Al_2O_3 + TiO_2 + ZrO_2)} \quad (24)$$

It was found that, in general, the higher the basicity, the cleaner the weld in regard to non-metallic inclusions. This generalization has a serious disadvantage (78, 84, 86, 87). It is unable to correlate the strengths and toughness of welds made with the high  $Al_2O_3$ ,  $TiO_2$ , and  $ZrO_2$  fluxes correctly, and although numerous basicity formulae have been considered since, 1968, none has been flexible enough to deal with a high amphoteric-oxide content.

It has been reported (88, 89, 90) that high flux basicity will reduce weld metal oxygen levels and improve toughness. Recently Eager (91) demonstrated this concept using two different expressions for basicity. It was found that for the fluxes investigated the weld metal oxygen content drops from about 900 to 300 ppm for a basicity index change from 0.5 to 1.5 and then remains constant with increasing basicity.

There is still some concern over using this index, which was primarily conceived for evaluating sulphur refinement, and for predicting weld metal oxygen as general criteria for submerged arc welding behavior.

Wood (92) suggests that silicon recovery in the weld metal or the silica activity in the submerged arc welding flux should be used to replace the basicity index. Wegrzyn (93) states that the oxygen content in submerged arc welds made with neutral and basic fluxes depends foremost on the amount of manganese and silicon in the weld metal and the ratio of manganese to silicon.

Other approaches to define basicity were also proposed and applied. K. Mori (85) proposed that the actual oxygen ion activity in the slag is more important than the strength of the metal oxygen bond and developed the following expression as a scale of acidity (or basicity):

$$B_L = \sum a_i N_i \quad (25)$$

where:  $a_i$  = characteristic constant for each of the components.  
 $N_i$  = mole fraction of the components.

When  $B_L > 0$  the slag is basic; when  $B_L = 0$  the slag is neutral; and when  $B_L < 0$  the slag is acidic.

North, et.al., (84) proposed an oxygen potential equation making a distinction between oxygen ion activity (basicity) and oxygen potential (stability of the oxides):

$$\text{Oxygen Potential} = \frac{100 - (\text{FeO} + \text{MnO} + \text{SiO}_2 + \text{TiO}_2)}{(\text{FeO} + \text{MnO} + \text{SiO}_2 + \text{TiO}_2)} \quad (26)$$

The stability of an oxide is determined by the ease with which it decomposes. Stable oxides require a relatively low partial pressure of oxygen to prevent decomposition while the less stable oxides require higher oxygen partial pressures. The oxygen potential is then the driving force for oxygen transfer to the weld metal. It is a general observation that welds made with acidic fluxes contain higher oxygen content and a low weld metal oxygen is associated with basic fluxes.

#### 2.6.2.2 Gas Metal Arc Consumables

In GMA welds are usually made with a constant voltage power supply in the electrode positive (DCEP) polarity (66, 68, 69, 72). This provides a stable arc and good penetration characteristics. The electrodes for the gas metal arc welding of carbon steels are classified based on strength, ductility, toughness, and chemical composition in AWS Specification A5.18. The content of microalloying additions such as titanium, and niobium are particularly important in controlling the microstructure of the weld metal (72).

The molten weld pool and adjacent metal are shielded from atmospheric oxygen and nitrogen by an inert gas/plasma column. The choice of cover gas is a particularly important in terms of bead shape, microstructure, and properties. Typical choices for cover gases include helium (He), argon (Ar), and carbon dioxide ( $\text{CO}_2$ ). Carbon dioxide is the cheapest cover gas available. Because of its low electrical conductivity and ionization potential (13.07 Volts),  $\text{CO}_2$  produces an unstable arc with low heat input. Argon with an ionization potential of 15.75 volts produces a quite stable arc. Penetration is a problem with pure argon, so small oxygen additions are usually made to increase penetration. Helium, with an ionization potential of 24.48 volts, produces the hottest arc.

Dillenbeck and Castagno (94) recently performed a study of cover gases and the associated effects on bead geometry. The results show that a mixture of 80%  $\text{CO}_2$  - 20% He produced the best bead geometry for a given cost. The mixtures of 74%  $\text{CO}_2$ -15% Ar-11% He and 60%  $\text{CO}_2$ -20% Ar-20% He closely matched the performance of the  $\text{CO}_2$ -He mixture at slightly higher costs.

The choice of a cover gas will also effect weld metal chemistry and inclusion content via its oxidizing ability. A maximum of

approximately 0.57 wt% oxygen is found in the weld metal. Grong (95) found that this limit is caused by the formation of a protective CO layer. As expected the absorbed oxygen continues to rise with increasing oxygen additions. Alloy losses are also related to the type of cover gas. Grong has shown that the loss of carbon occurs almost entirely in the molten drop at the electrode tip. Silicon losses take place mainly in the weld pool. Manganese is lost in the arc and weld pool via evaporation rather than oxidation.

### 2.6.3 The Heat Affected Zone

Fusion welds in steel may be classified into several zones based on the thermal history and the resulting microstructures (67, 96). Figure 6 from Easterling (67) shows a schematic illustration of the fusion and heat affected zones of a weld. Material within the fusion zone is melted by the heat input and a weld solidification structure is achieved. Material within the heat affected zone does not undergo melting, but the microstructure may be changed by one of several phenomena. The extent of microstructural modification depends on the peak temperature attained at the particular point and on the cooling rate below the eutectoid temperature.

The peak temperature controls the extent of austenization and grain growth. In the grain growth region of the heat affected zone which borders the fusion zone the maximum temperatures are high enough for the transformation to austenite and for grain growth to occur during a small time interval. In the recrystallized region, temperatures in the austenite phase field are reached and recrystallization and grain refinement occur. However, the temperatures are not sufficiently high for grain growth. In the tempered region the temperature does not exceed the A1 temperature. No transformations occur, but some tempering is observed. Outside of the tempered region the microstructure of the parent plate is not changed.

The cooling rate below the eutectoid temperature controls the austenite decomposition products for regions where the transformation to austenite occurs. This is generally expressed in terms of the time for cooling between 800°C and 500°C. It is a function of welding process variables: heat input, weld velocity, weld geometry, reinforcement crosssection, and weld preheat. For low heat input arc welds such as gas metal arc welds the cooling time between 800°C and 500°C is on the order of 10 seconds. Electroslag welds have a slow weld velocity and a large heat input, and the cooling time between 800°C and 500°C is on the order of minutes.

The heat affected zone microstructures which result from different cooling rates have a significant influence on mechanical properties (97). Nuclear waste containers represent an extreme case because of the heavy sections and the high heat input required for the welding processes. The slow cooling of fusion and heat affected zones of high heat input welds tends to

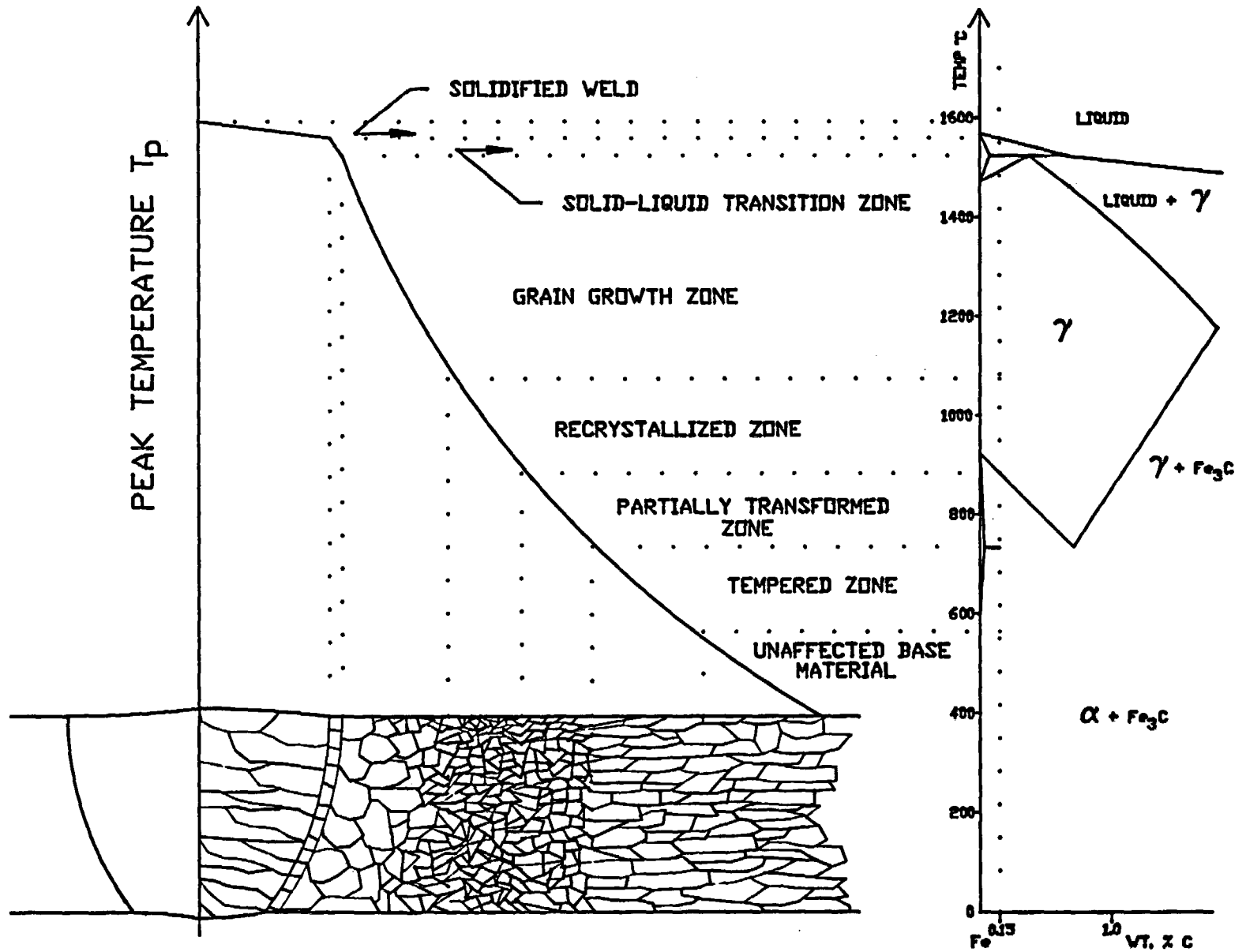


FIGURE 6. Grain size in the heat affected zone as a function of peak temperature and distance from the fusion line (14).

promote the formation of low toughness ferrite/pearlite structures with large grain boundary ferrite allotriomorphs. Rapid cooling such as is experienced with low heat input, thin section welds tends to result in the formation of bainitic or martensitic structures with low ductility. Acicular ferrite microstructures with high toughness appears to be formed at intermediate cooling rates with the aid of non-metallic inclusions which act as nucleation sites for acicular ferrite.

Kaae and Bailey (98) investigated the HAZ fracture toughness of two controlled-rolled Nb treated low carbon manganese steels. These steels were welded by SMAW, SAW, and electroslag processes, respectively. Results of impact tests showed that the fracture toughness of the HAZ decreases with increased energy input during welding. Values of 216, 54, and 41 ft. lb. in order of increasing energy input at a test temperature of  $-15^{\circ}\text{C}$  typify this trend. Transition temperatures of  $15^{\circ}\text{C}$  for an energy input of 2,000 KJ/in.,  $-25^{\circ}\text{C}$  for 170 KJ/in., and  $-40^{\circ}\text{C}$  for 20 KJ/in. were reported. This increasing transition temperature with increasing energy input is attributed to greater coarsening of the austenite grain size for the higher heat processes. In addition, fracture toughness of the electroslag HAZ in the upper shelf region was significantly below that of the other two processes.

Hrivnak (99) also studied the electroslag HAZ and concluded that electroslag joint properties are most influenced by coarsening of the austenite grains adjacent to the fusion zone and by possible formation of viscous films of impurities on the austenite grain boundaries. In addition, Hrivnak points out that transformations in the HAZ may be affected by thermally induced stresses during welding. Malinovska and Hrivnak (100) found that the critical areas of an electroslag weld in low-carbon steel, with respect to notch toughness are the weld metal center and that portion of the HAZ heated to temperatures above  $1,100^{\circ}\text{C}$ . It is possible to restore degraded HAZ properties with heat treatment after welding. The effects of normalizing (austenization followed by an air cool) on the properties of electroslag heat affected zones have been reported by Malinovska and Hrivnak (99), Bentley (101), Braun, Eregin and Malai (102), and Braun et. al. (103). Bentley (101) investigated the recovery of HAZ properties by successive normalizing treatments for four different mild steels. On the basis of Charpy V-notch tests at one temperature the toughness of the HAZ was markedly improved after the first normalizing treatment and slightly improved by the second. An overall loss of toughness was found for a high sulfur steel where the toughness was only recovered 50% by the normalizing heat treatment. This loss was attributed to the formation of a sulfur rich film on the austenite grain boundaries.

Braun and co-workers (102, 103) addressed the effect of heat treatment on the microstructure and impact properties of high-strength, low alloy steels of 0.25 to 0.30 wt. % carbon. These

investigations showed that the HAZ impact properties could be nearly recovered by normalizing from 950°C followed by tempering at 650°C for 20 hours. Toughness of the HAZ generally increased with increasing time at the tempering temperature.

Even though normalization treatments may produce marked recovery of HAZ properties, this treatment is limited from a practical standpoint. At the temperature required for normalization, the yield strength of most steels drops to such a value that heavy welded components may be deformed by their own weight (100). The need for dimensional stability in addition to the economic factors in high temperature heat treatment has prompted interest in heat treating electroslog weldments at lower temperatures.

Heat treatment of electroslog weldments in the temperature range A1 to A3 has been studied (100, 104, 105). Malinovska and Hrivnak (100) found that properties superior to those obtained by normalizing could be obtained in steels of 0.15 to 0.19 weight percent carbon and 1.21 to 1.23 weight percent manganese by annealing at 750°C for five hours and air cooling, followed by reheating to 630°C and holding for ten hours followed by furnace cooling. It was noted that the coarse grain region in the HAZ forced by overheating during welding was completely refined. It was also found that the yield strength of these steels was high enough at 750°C to prevent distortion due to the weight of the weldment. Similar studies of four steels ranging from 0.15 to 0.25 weight percent carbon and 1.47 to 1.6 weight percent manganese were made by Zeke and Malinovska (105). The steel with the highest carbon content in this group was found to respond most favorably to the heat treatment between the A1 and A3 temperatures. Makara, et.al. (104) also found that heat treatment in the A1 to A3 temperature range markedly improved the notch toughness of steels of 0.07 to 0.09 weight percent carbon and 1.07 to 1.75 weight percent manganese. In this study a treatment at 780°C for 8.5 hours followed by furnace cooling was found to be most effective. Specimens held at the heat treatment temperature for longer than 11 hours showed a sharp loss of notch toughness.

The carbon equivalent (CE) is commonly used to calculate the necessity for preheat and post weld heat treatment for steels using the empirical expression:

$$CE = \%C + \frac{\%Mn}{6} + \frac{\%Cr}{5} + \frac{\%Mo}{4} + \frac{\%P}{3} + \frac{\%Ni}{15} \quad (27)$$

The carbon equivalent values are also used for comparison of their hardenability and susceptibility to hydrogen damage. It is usually considered that a steel with carbon equivalent value less than 0.40 may be welded without preheating. Carbon equivalent

values between 0.40 and 0.65 suggests a need for preheat treatment prior to welding, while values greater than 0.65 suggest both preheat and post weld heat treatment for the steel.

#### 2.6.4 New grades of microalloyed steels

High strength - low alloy steels (HSLA), or microalloyed steels are low carbon (0.06 - 0.15% C) steels which contain small amounts of elements such as niobium, vanadium or titanium. The concentration of these elements is rarely above 0.1 weight percent. In spite of this minimal amount of addition, their ability to form nitrides and carbonitrides limits the grain growth very effectively and produces a very fine grained microstructure. This resulting microstructure shows superior strength and toughness when compared to plain carbon steels. Together with microalloying, thermomechanical processing provides a further step of upgrading the final quality of the product. The strength of such a product is around 500 MPa (72.5 ksi) and the impact transition temperature is as low as  $-80^{\circ}\text{C}$ . Such improvements in mechanical properties are beneficial. However, good weldability is another essential requirement.

Current literature shows no unified opinion on niobium effects on weld metal toughness. Some authors (106, 107) found that niobium was always harmful to impact toughness, while others (108) reported that up to a certain limit, niobium is beneficial. Garland and Kirkwood (109-111) have proposed a model concerning niobium behavior in weld metal toughness. In principle, niobium deteriorates the toughness by precipitating fine Nb(C,N) particles, increasing the strength. At the same time, niobium improves the toughness by promoting acicular ferrite formation. The net effect of the niobium additions depends on which contribution is greater. Post weld heat treatments of niobium steels usually result in precipitates. Therefore, multiple pass welding is a serious concern in welding niobium based microalloyed HSLA steels.

#### 2.6.5 Microstructure and Toughness

Toughness in weld metal does not depend on a single factor but on a number of variables, often interrelated, e.g., welding procedure, flux composition, cooling rate, microstructure, etc. An investigation to improve notch toughness of submerged arc welds was conducted by Lewis et. al. (112). Their attempt was to change filler wire compositions to match those used in other arc welding processes which produced satisfactory welds. Surprisingly, this was not successful, and studies were then made to see why submerged arc welds had lower notch toughness than gas metal arc welds. Submerged arc welds were found to contain more inclusions, oxygen, and silicon than gas metal arc welds. Obviously, the flux had an influence on the mechanical properties. Lewis, et. al, (113) later attempted to lower the oxygen and inclusion content by modifying a standard flux with various additions.  $\text{CaF}_2$  and  $\text{TiO}_2$  additions were found to be beneficial in improving the weld metal toughness. The oxygen contents of the welds made with the modified silicate inclusions

were fewer and smaller. They reported an optimized flux composition which produced a 540 ppm oxygen content compared with 960 ppm for those welds made with the standard flux. Even though we expect the oxygen of wrought steel to be below 100 ppm oxygen, the very lowest weld metal oxygen levels for flux related welding processes are in the range of 200-300 ppm. Manganese silicate submerged arc welding fluxes are known to produce a high weld metal oxygen content, up to 900 ppm oxygen. New arc welding fluxes based on lower silicon contents, usually with a substantial  $\text{CaF}_2$  content, have been developed to promote lower oxygen content and thus higher weld metal toughness. Experiments with varying  $\text{CaF}_2$ ,  $\text{FeO}$ , and  $\text{MnO}$  contents in a  $\text{SiO}_2$  flux (114, 115) have shown that there is a major reduction in weld metal oxygen content for calcium silicates compared with manganese silicates of the same silicon content, and a further decrease in weld metal oxygen content is obtained with  $\text{CaF}_2$  additions. These flux modifications illustrate the conceptual approach to the development of advanced arc welding fluxes. The consumables for flux related welding processes must be carefully selected considering the wire and plate compositions and the heat input.

The transformation of weld metal austenite can give different microstructures depending on cooling rate and on the chemistry of the steel. When the cooling rate is extremely slow, the ferrite nucleates at the prior austenite grain boundary, or on inclusions lying within the prior austenite boundaries. Growth proceeds along the boundary and advancing into the austenite grains. Some researchers termed grain boundary ferrite as ferrite veining, because of its distribution in the microstructure. The continuous, large flat surfaces provided by the veining constitute an easy crack propagation path which means low resistance to cleavage fracture initiation and propagation. Grain boundary ferrite needs little or no undercooling and is sometimes considered the "equilibrium" transformation product.

Grain boundary ferrite formation and acicular ferrite formation (116) are two competing processes that occur concurrently. However, it should be noted that grain boundary ferrite is the first to nucleate and grow. The formation of ferrite side plates (Widmanstätten ferrite) and then acicular ferrite occur after the grain boundary ferrite. Sometimes the boundary nucleated ferrite (116) grows across the austenite grains along preferred growth directions as parallel sheaves of laths which are usually referred to as ferrite side plates. The aspect ratio (length/width) of the ferrite side plates is approximately 10:1 (116). This ratio increases as the weld metal oxygen increases. A Kufdjumov-Sachs relationship was observed between the ferrite side plate and the parent grain (117). The mechanism of Widmanstätten ferrite formation is not completely clear. Some researchers report that side plates grow by a shear mechanism, and others report that carbon diffusion is necessary because of different solubilities of carbon in austenite and in ferrite (118). Another approach (118) uses the interface instability theory to explain the advance of the plate, which depends on how fast carbon can diffuse away from the plate. Undercooling is necessary to induce the Widmanstätten ferrite formation.

Non-metallic inclusions (116, 119, 120) act as nucleation sites for acicular ferrite. Once nucleated, the acicular ferrite laths grow until they impinge on each other (if the conditions are favorable). Acicular ferrite is characterized by the interlocking ferrite laths of high acicularity with a length to width ratio of approximately 4:1 (116). The fine interlocked ferrite laths provide high resistance to cleavage initiation and propagation. The laths have high angle boundaries with substructures of high dislocation density (121). The absence of entrapped and grain boundary carbides constitute the basic distinction between acicular ferrite and bainite. The starting temperature for acicular ferrite (109, 110, 122, 123, 124) is slightly lower than that for grain boundary ferrite, but it is higher than that for bainite formation and martensite formation. The amount of acicular ferrite is directly related to the number and size distribution of non-metallic inclusions.

The nomenclature of weld metal microstructure is not totally uniform (123, 124, 125). This discrepancy in terminology is a source of confusion. There is still a need to thoroughly characterize all constituents of weld metal microstructures, because distinctions between some of the phases are not clear. Systems for the classification of austenite decomposition products in weld metal microstructures have been developed by the International Institute of Welding (IIW) (126 - 131), and by the Japanese Welding Society (JWS) (132). Table 3 below shows a comparison of these microstructural classification schemes (133) with the microstructural constituents arranged in order of decreasing transformation temperature.

The best combination of strength and toughness in mild-steel weld metal has been found to be partially due to the development of fine acicular ferrite microstructures (120, 134). Proeutectoid ferrite will predominate when the ferrite transformation occurs at high temperatures (135). The promotion of acicular ferrite should result from achieving the proper amount of supercooling through either rapid cooling or through alterations in weld-metal chemistry which delay the ferrite transformation. The microstructures to be avoided are those of high temperature blocky or proeutectoid ferrite which result from a small degree of supercooling, and those which contain small amounts of martensite which are caused by a large degree of supercooling (136). It is recognized then, that acicular ferrite is the microstructural constituent which generally correlates with a high resistance to cleavage fracture (137, 138). Thus, any factor leading to an increase in the volume fraction of this constituent is of considerable importance in efforts to improve weld-metal toughness.

The achievement of an acicular microstructure and high toughness by weld alloying with Mn, Mo, Ti, B, Ni, Nb and V has been reported (109, 110, 139, 140, 141). Oxygen, apparently, is one of the factors which has a fundamental significance on the weld

**TABLE 3 - COMPARISON OF THE IIW AND JWS MICROSTRUCTURE  
MICROSTRUCTURAL CLASSIFICATION SCHEMES**

JWS System	IIW System
<b>FERRITE</b> -Grain Boundary Ferrite -Intragranular Polygonal Ferrite -Side Plate Ferrite	<b>PRIMARY FERRITE</b> -Grain Boundary Ferrite -Intragranular Polygonal Ferrite
<b>PEARLITE</b> -Pearlite	<b>FERRITE CARBIDE AGGREGATE</b> -Pearlite
<b>ACICULAR FERRITE</b> -Acicular Ferrite	<b>ACICULAR FERRITE</b> -Acicular Ferrite
<b>BAINITE</b> -Upper Bainite -Lower Bainite	<b>FERRITE WITH A SECOND PHASE</b> -Ferrite with an Aligned Second Phase. -Ferrite with a Non Aligned Second Phase
<b>MARTENSITE</b> -Lath Martensite -M-A Constituent	<b>MARTENSITE</b> -Lath Martensite -Twin Martensite

metal transformation behavior (90, 142). Reducing the weld metal oxygen content from a high value of 600 ppm oxygen content, the microstructure goes from high contents of grain boundary ferrite to acicular ferrite, and at very low weld metal oxygen contents the microstructure becomes bainitic. The weld metal transformation behavior has been explained (90, 142, 143) to be influenced not by the effect of oxygen in solution but by the oxygen as it affects the number of small inclusions available as potential nucleation sites for upper transformation products during continuous cooling.

Inferior notch toughness of high oxygen welds could be improved by deoxidizing the weld with limited aluminum additions (143, 144). Aluminum additions were also related to a change in the number, type, and size distribution of weld metal inclusions. North, et.al., (86) correlated the reduction in transition temperature with a microstructure change. The amount of proeutectoid ferrite was found to decrease as the aluminum content increased.

The reliability of using the weld metal oxygen content as the only indicator of the inclusion content has been questioned (120); however, the weld metal oxygen content is related to the inclusion density (145, 121). A high inclusion density has been found to promote the nucleation of ferrite, particularly at the higher temperatures during the cooling cycle (121, 134). The resulting higher temperature ferrite morphology can be blocky ferrite or Widmanstätten side plate ferrite. Inclusions are commonly found in the center of blocky ferrite grains (112). As would be expected, each type of inclusion, and thus flux type, has its own relationship between inclusion density and weld metal oxygen content. Since it is the inclusion density which is basic to the nucleation process for ferrite, the inclusion density rather than that oxygen content should be fundamental to any microstructure-property relationship. Weld metal oxygen is only indirectly related to the tendency for the formation of a specific ferrite microstructure. Alloying elements affect the hardenability of steels; a relatively large degree of which is necessary to form acicular ferrite. Above 600 ppm oxygen, inclusions are reported (138) to dominate the mechanical behavior. Between 600 and 300 ppm oxygen there is influence by both inclusions and hardenability additions; and below 300 ppm oxygen the hardenability additions are considered to dominate. High concentrations of inclusions, corresponding to oxygen contents greater than 600 ppm., strongly influence the upper shelf toughness and the ductile brittle transition temperature.

Research has been performed to determine the proper balance of Mn, Nb, O, B, Ti, Mo, V, and Zr to maximize the amount of acicular ferrite in the weld metal (109, 146-149). The hardenability effect is shown (150) schematically with a hypothetical continuous cooling transformation diagram (134) in Figure 7. Slow cooling causes the formation of blocky ferrite, while faster cooling rates produce acicular ferrite. Increasingly rapid cooling rates produce bainitic and ultimately martensitic microstructures. Figure 8 (150) shows that an

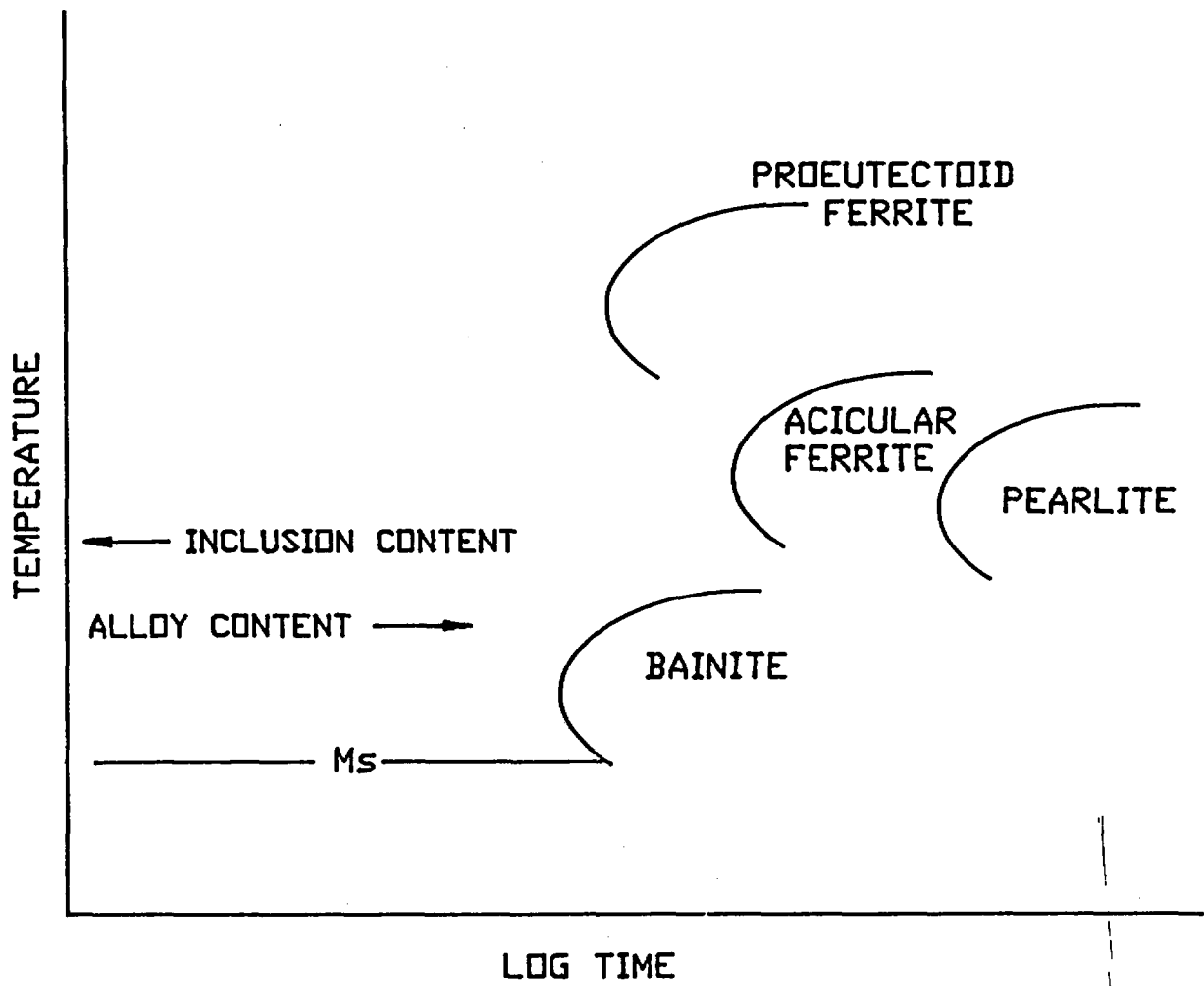


FIGURE 7. Schematic CCT diagrams showing the influence of inclusions on the nucleation of acicular ferrite (150).

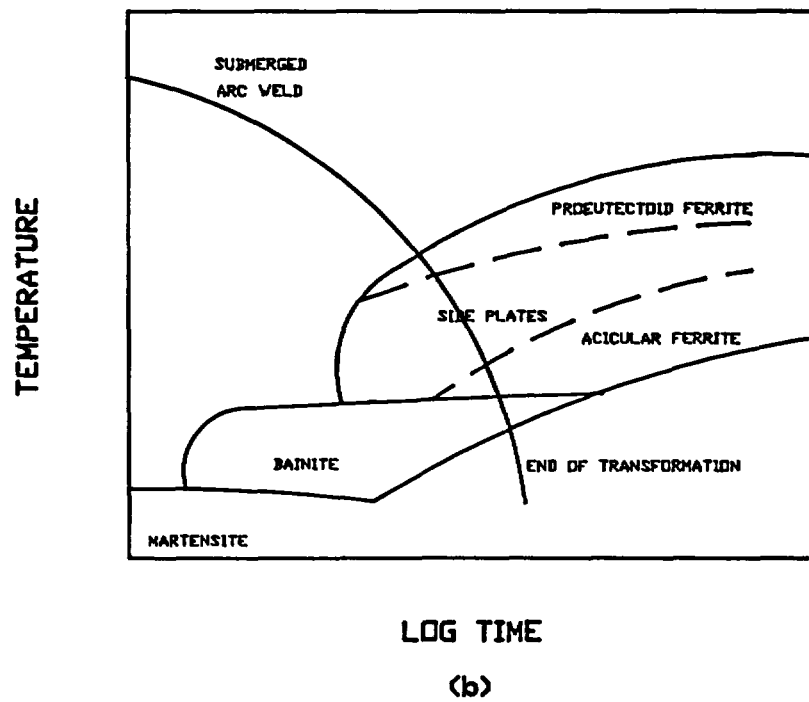
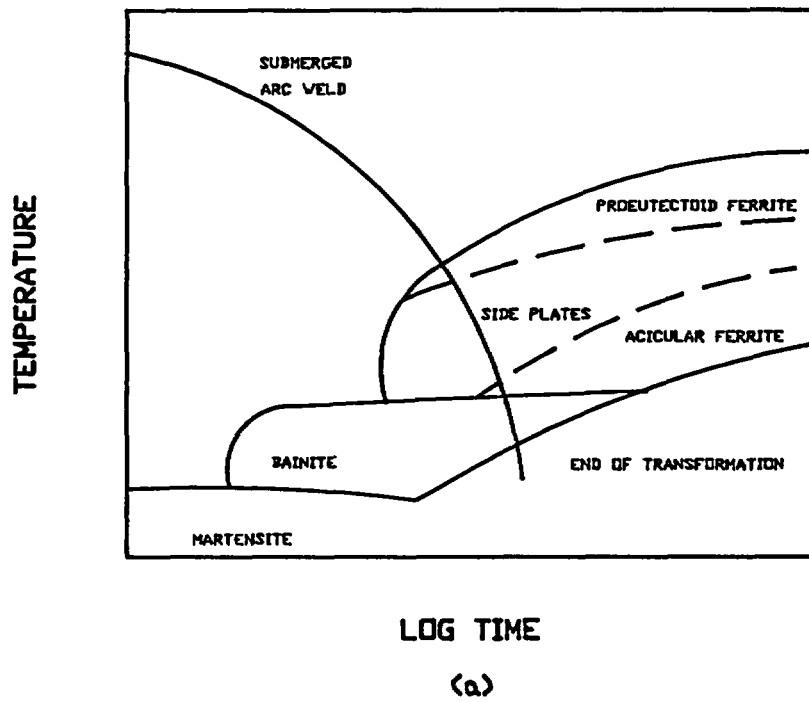


FIGURE 8. Schematic CCT diagram showing the influence of cooling rate on weld microstructure (134).

increase in oxygen, thus in nucleants, shifts the CCT curve to the left and causes an increase in the amount of resulting proeutectoid ferrite.

Grain boundary ferrite (in high oxygen welds) has been associated with a specific type of inclusion. Inclusions from acidic fluxes are shown to be of the manganese silicate type (121). Usually a high inclusion density and large inclusions were found associated with acidic and neutral fluxes (151, 152). For neutral and basic fluxes, distinct geometric shapes of inclusions were seen (spheres, triangles, irregular shapes, etc.). The shapes of the inclusions may be important because of a match or mismatch between certain crystallographic planes in the inclusion and in the ferrite. This may alter the nucleation and transformation behavior of the weld metal. These inclusions could be correlated with the type of flux used. For example, triangular shaped inclusions are mainly found in welds produced with a basic flux. Because of surface tension, glassy oxide inclusions formed originally in the liquid are expected to be spherical in shape. This is not true, however, for refractory oxide inclusions, nitrides, or for inclusions formed by solid state reactions.

#### 2.6.6 Mechanical Properties of Low Carbon Steel Weld Metal

The mechanical properties of low carbon steel weld metal are controlled by the microstructure; and the microstructure is controlled by the cleanliness, composition, and welding heat transport and solidification variables. Historically, flux basicity has been used to relate flux chemistry to weld metal properties. Highly basic fluxes have been reported to provide greater toughness (75, 86, 90) and high weld cleanliness (90, 137, 138). In carbon-manganese steel weld metals, it is generally accepted that a higher proportion of fine acicular ferrite (approximately 90%) is desirable to impart a combination of strength and high toughness (153). It is considered that the finer and more interlocking the individual laths, other factors being equal, then the greater the resistance to cleavage fracture initiation and propagation (90). Farrar, Tuliani, and Norman (137) suggest the same microstructure-toughness relationship, but add a condition of low inclusion content to achieve a high toughness.

Plots of toughness contours versus oxygen content and manganese content (154) which suggest that there are optimum ranges of oxygen and manganese contents which maximize weld metal toughness. At a fixed manganese content, a coarse microstructure predominates at a high oxygen level. Decreasing the weld metal oxygen content refines the microstructure and increases toughness, and a further decrease in oxygen allows the formation of a bainitic structure with reduced toughness. Similar microstructural changes can be observed at a fixed weld metal oxygen content with a decrease in the manganese content. The maximum toughness correlates with the maximum volume fraction of acicular ferrite in the weld microstructure.

## 2.7 Quality Assurance

Selection of quality requirements for any manufactured item is based upon an understanding of design, fabrication methods, and conditions of use such as lifetime and maintenance objectives. Matters of design, fabrication, and conditions of use are known in general terms for cast steel overpacks. Definitions of sought-after mechanical and metallurgical characteristics of the overpack are not precisely known at this time. Review of applicable quality assurance methods has therefore been generalized and based upon assumptions about probable process and material choices.

Development and implementation of a quality assurance program for manufacture of waste overpacks will involve application of a traditional approach used for manufacture of industrial components that fall under the purview of government regulation because of potential threat to human safety or the environment. Criteria and requirements are specified by codes and standard; materials and processes are subject to certification and qualification; and final components are evaluated by non-destructive or destructive methods. The various aspects of this approach and their application to waste overpacks will be examined in the following paragraphs.

### 2.7.1 Codes and Standards

Standards are those documents that govern and guide the materials, processes, products, services, and systems used in the manufacture of an end item. Codes are a subset of standards that are generally mandatory with respect to minimum requirements. Standards are developed, used and updated by committees from private and governmental organizations that are interested in a particular type of product. Private organizations include trade groups, professional societies, and end users. Governmental organizations are either regulatory or user oriented. Committees are purposely balanced and a consensus must be achieved by a high percentage of the members. For this reason, standards developed in such a way are termed consensus standards.

Standards are usually prepared and issued under the auspices of a professional society or trade association. Some standards are considered to have sufficient general value and applicability to be adopted as an American National Standard by the American National Standards Institute (ANSI). ANSI is a private organization with responsibility for coordinating national standards for use within the United States. ANSI does not prepare standards but adopts those prepared by others. Adoption by ANSI does not imply mandatory application. However, a standard may carry the force of law if cited by government rules or regulations.

Organizations that issue standards that may be applicable to nuclear waste containers include American Society of Mechanical Engineers (ASME) (190), American Welding Society (AWS) (191), and ASTM (192).

ASME is responsible for the ASME Boiler and Pressure Vessel Code (BPVC). This code is referenced in the safety regulations of most states and major cities of the United States and is also included by reference in a number of Federal Regulations. While the BPVC is not specifically applicable to nuclear waste containers, it is a suitable model for preparation of a specific code. It is unique among manufacturing standards because it requires third party inspection independent of the manufacturer and user. The National Board of Boiler and Pressure Vessel Inspectors examines and commissions inspectors. These inspectors are employed by authorized agencies such as insurance companies or regulatory bodies. Fabricators are subject to an audit of procedures and quality management before being authorized to manufacture pressure vessels that carry the ASME code stamp. The BPVC is also unique in its comprehensive treatment of issues that affect final quality. Such issues as design, materials, processes, inspection, operator qualification, and quality management are subject to regulation by the code.

AWS issues and maintains numerous codes, specifications, and guides covering welding and quality control of welding. Many of these have been adopted by ANSI as national standards. Specifications for filler metals and recommended practices for various welding processes are unique to AWS. Many filler metal specifications have been approved by ANSI and incorporated in the ASME BPVC.

ASTM, formerly the American Society for Testing and Materials, publishes specifications for materials, testing methods and analytical procedures covering virtually all materials of industrial interest. The ASTM A216 specification (156) describing the reference material for this study and several other specifications (157 - 174) cited in this document are examples of specifications that may be applicable to the manufacture of nuclear waste containers. ASTM materials specifications usually contain mandatory requirements that must be met in order to apply the ASTM designation and supplementary requirements such as heat treatment or additional testing that may be specified by the user if desired.

Departments of the Federal Government usually apply national consensus standards by reference in the United States Code of Federal Regulations. New or existing consensus standards for manufacture of high level waste containers will presumably be adopted and referenced in Title 10, Part 60 as it is developed. Consensus standards may be amended or supplemented as dictated by need. The Department of Energy has used the ASME BPVC supplemented by internal standards known as RDT standards to administer the nuclear energy program.

## 2.7.2 Qualification and Certification

The manufacturing of overpacks is envisioned to be based upon the processes of casting and welding. The body will be cast as a hollow cylinder, probably by centrifugal casting. One end of the cylinder will be closed by welding a plug into the end, possibly in the same shop where the casting is done. The other end will be closed after emplacement of the waste. This final enclosure will be done as a remote operation.

Cast products are typically made to a product specification, often with methods that are considered to be proprietary. The end product is specified as to soundness, chemical and metallurgical characteristics, mechanical properties, and dimensional characteristics. Codes usually do not attempt to regulate quality of castings by qualification of manufacturing personnel or by control of manufacturing methods. On the other hand, most codes and standards require the qualification and certification of welding procedures and of operators who perform the welding. Also, weldments are subject to inspection by qualified inspection personnel using specified procedures.

Welding qualification focuses separately on the process and the welder or process operator. All codes and standards require welding to be done according to a qualified welding procedure specification (WPS). The manufacturer is generally responsible for preparation of the WPS to meet code requirements. The WPS specifies all of the welding variables such as process, base metal, filler metal, joint design, welding position, welding current, arc voltage, travel speed, shielding gas or flux, preheat, interpass temperature, and post weld heat treatment. Variables are designated as essential or nonessential. A WPS must normally be qualified by demonstrating that the procedure may be used to produce under production conditions welded joints that meet prescribed requirements. Changes in essential variables outside of specified limits require requalification of the WPS.

The purpose for qualifying a WPS through testing of weld specimens is to determine that welding done in accordance with the WPS can produce welds with properties desired for the end use. The mechanical and metallurgical properties of a welded joint may be altered significantly by changes in the WPS. In the case of nuclear waste containers, the key issues will be weld soundness and long term compatibility with the repository environment. Qualification testing may include corrosion testing in addition to more commonly specified mechanical testing and metallurgical examination. Such testing may be applicable to both castings and weldments for use in high-level nuclear waste containers.

Welder performance qualification tests are used to determine the ability of the person being tested to produce acceptable welds using a specified process and procedure. The basic purpose of such qualification testing is determination of a required minimum skill level. Welder qualification is generally done according to

a qualified WPS and the results are often assessed according to the same qualification requirements as for the WPS. Welder qualification and qualification of the WPS are, however, separate issues. Changes in welding procedure which may make additional or different demands on the welder's skill are usually reason for requalification.

Documentation is an important aspect of qualification and certification for both procedures and operators. An up-to-date version of each WPS in use must be kept on file. Qualification records for welders and welding operators must be kept current and periodic requalification is sometimes required to maintain code compliance.

### 2.7.3 Inspection

Determination of compliance of a manufactured item with codes, standards, or specifications is generally done by physical inspection of the product during and after manufacturing. Nondestructive examination or testing, NDE or NDT, are synonymous terms that describe inspection of a product without affecting its usefulness. Inspections for code compliance using NDE requires that tests be conducted according to established or qualified procedures by properly trained and qualified personnel and that results are interpreted against an agreed upon standard. Commonly used NDE methods include visual inspection, liquid penetrant, magnetic particle, radiography, eddy current, ultrasonic and acoustic emission. Of these methods visual inspection, when properly applied, is by far the most versatile and useful. Of the other methods, liquid penetrant, magnetic particle, and eddy current are applicable to detection of surface or near-surface discontinuities. Discontinuities that are concealed deep within a structure may be identified by radiography, ultrasonics, and acoustic emission.

Another important method of identifying potential defects in manufactured items is process monitoring. Although typically not required by the various codes, continuous monitoring and recording of process variables can be used to confirm that a qualified process has been operated within specified limits. Acoustic emission may be used to detect and locate potential defects during the welding process (193).

Destructive tests such as mechanical testing and metallographic examination are useful in determining the quality of a fabricated item. For small or inexpensive fabrications it is common to do destructive testing on a sampling basis from the actual production run. On larger structures such as ships or pressure vessels examination of materials of construction, individual components, or test weldments is a more reasonable approach. Destructive examination can be used to directly observe characteristics such as mechanical properties of base metal and welds, soundness of base metal and welds, location and depth of

welds, extent of heat affected zone, and metallurgical structure of weld and base metal. Components or specimens may also be subjected to environmental or service testing as part of a destructive testing program.

Body and lid components for cast steel overpacks will be inspected at the place of manufacture. The body is assumed to be a centrifugal casting with end welded in place by submerged arc welding. In addition to visual inspection, the most widely applied NDE method for examination of similar components is radiography. This method is reliable in locating porosity, inclusions, and cracks in some orientations in both the casting and the weld. Liquid penetrant inspection may be used as a supplementary technique to look for discontinuities that may extend to the surface. The final closure weld after waste loading will be done remotely and will therefore present a challenge for adequate inspection. Visual inspection can be accomplished through remote video or fiber optic means. Ultrasonic testing may be used to identify subsurface defects if coupling by liquid or jell can be accommodated. Process monitoring including, perhaps, continuous acoustic emission monitoring of the welding process will be important to controlling quality of the final closure weld.

### 3. EXPERIMENTAL RESEARCH

#### 3.1 Experimental Rationale

The effect of manufacturing on container performance encompasses a wide range of process and material variables. Useful experimental research within the confines of the overall project budget was possible only by clearly focusing the work toward a few attainable objectives. The first of these objectives was to characterize the microstructures that will result from material and process combinations within the range of materials and processes that the DOE will likely use. The second objective was selection and verification of a few important process limits defined by analytical research. Third, a preliminary investigation of changes in starting microstructure that might result from repository thermal conditions was performed.

The overpack material can be expected to show a wide variation in starting microstructures as a result of differences in alloy chemistry and cleanliness, initial solidification processing, welding, and thermal processing during or after fabrication. A series of specimens was prepared in the laboratory to simulate a wide variation in possible starting overpack microstructures.

The influence of alloy composition and cleanliness on microstructure was investigated using three alloy composition categories within the ASTM A-216, Grade WCA specification for carbon steel castings which are suitable for welding. The target alloy element and tramp element contents for the three composition categories are given in Table 4. The carbon content was held near 0.18% for all three categories. The manganese, silicon, and oxygen contents were varied to change the hardenability, cleanliness, and the nature of the deoxidation product. The silicon and manganese levels influence the state of deoxidation, and the ratio of silicon to manganese determines the nature of the deoxidation product (solid silica or a liquid manganese silicate). The ratio of the manganese to oxygen contents influence hardenability through alloy content and cleanliness.

TABLE 4 - CHEMICAL COMPOSITION CATEGORIES

Alloy	%C	%Si	%Mn	O%	%S	%P	Mn/O
A	0.18	0.10	0.50	0.020	0.01/0.02	0.02/0.03	25
B	0.18	0.25	1.00	0.007	0.01/0.02	0.02/0.03	145
C	0.18	0.25	1.00	0.007	0.045	0.02/0.03	145

Figure 9 shows the influence of silicon and manganese additions on the dissolved oxygen content for a steel with an initial oxygen content of 0.1% (1000 ppm). Additions of 0.1% Si and 0.05% Mn reduce the oxygen level to about 0.02% (200 ppm), and leave 0.05% Si and 0.4% Mn in solution after deoxidation. The additions of 0.25% Si and 1.00% Mn reduce the dissolved oxygen content to about 0.008% (80 ppm) and leave 0.2% Si and 0.9% Mn in solution after deoxidation. Figure 10 shows the influence of the silicon to manganese ratio on the nature of the deoxidation product. For the silicon and manganese charges given in Table 4 the deoxidation product is molten manganese silicate at a steel making temperature of 1600°C.

The compositions of the three alloys in Table 4 are chosen to vary the hardenability, oxygen content, and the cleanliness in terms of nonmetallic inclusions. Alloy A has a low manganese to oxygen ratio to reduce hardenability and increase the oxide inclusion content. Alloy B has a high manganese to oxygen ratio to provide higher hardenability and limit the oxide inclusion content. Alloy C has the same high manganese to oxygen ratio as Alloy B plus the addition of 0.045% sulfur to investigate the influence of sulfide inclusions on alloy microstructure. The ASTM A-216 specification allows residual alloy elements to the following maximums: Cu 0.5%, Ni 0.5%, Cr 0.4%, Mo 0.25% and V 0.03%. Total residual alloy content is limited to 1.0%. The levels of these residual elements were minimized in the experimental heat compositions. The influence of solidification rate on the microstructure was determined using a range of cooling rates to provide a range of cell spacings or secondary dendrite arm spacings. Figure 11 shows the variation of the secondary dendrite arm spacing with cooling rate during solidification for carbon steel alloys. The plot is linear because the secondary dendrite arm spacing is a power function of the cooling rate.

The slow solidification of large sand castings is expected to produce a secondary dendrite arm spacing of 400 to 500 micrometers at a cooling rate of about 3°C per minute during solidification. Low heat input welds such as gas metal arc welds are expected to cool at a rate of 5,000 to 10,000°C per minute. At such rapid cooling rates secondary dendrite arms do not form, and a cellular solidification microstructure is obtained with a cell spacing of about 20 micrometers. The solidification rates and microstructures of ingots, centrifugal castings, electroslag welds, and submerged arc welds are expected to fall in between these two limits. For the present experiments castings with small secondary dendrite arm spacings were produced by pouring into a gray iron ingot mold. Specimens with very large dendrite arm spacings were produced by slow solidification in an induction furnace with the power gradually turned down over a period of 10 to 30 minutes. Welding will be used to assemble and seal the cast steel container; therefore, the weld and its heat affected zone in the cast base metal have been addressed experimentally. Submerged arc welds (SAW) and gas metal arc welds (GMAW) were investigated using consumables and procedures

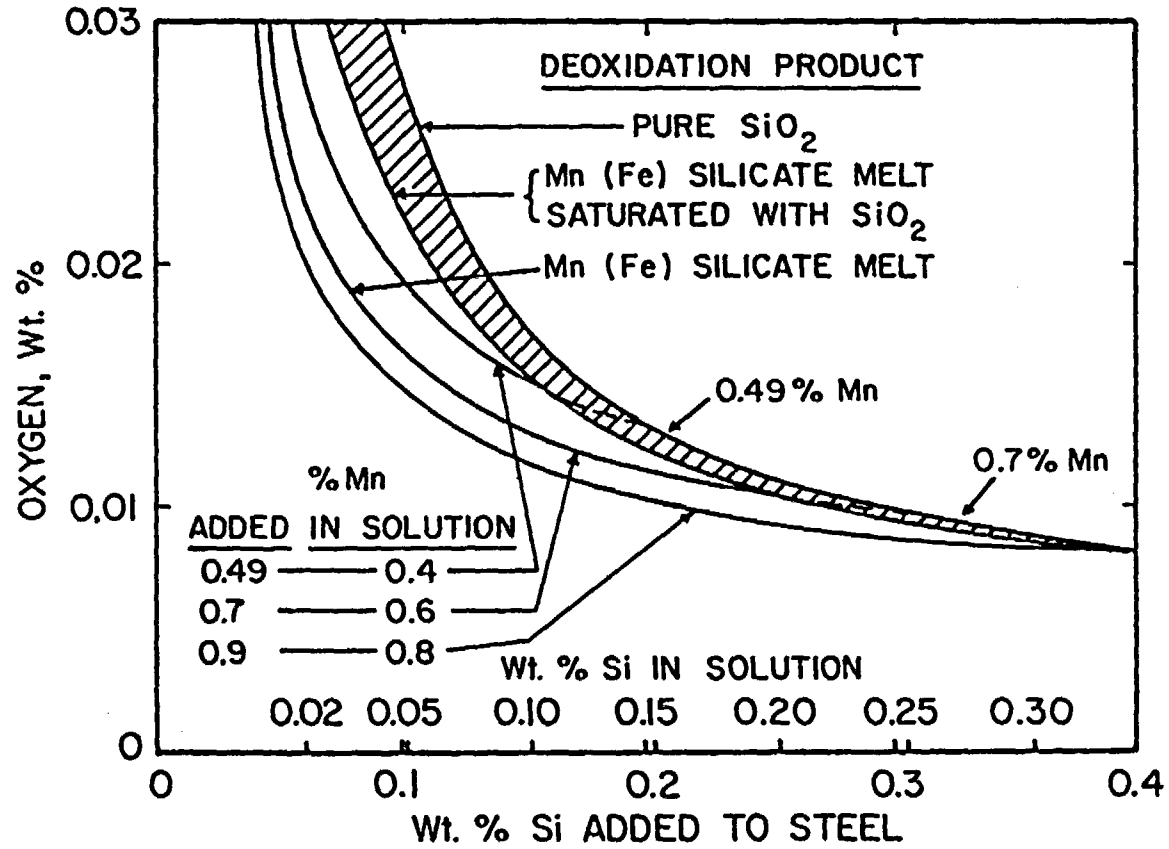


FIGURE 9. Influence of silicon and manganese on the dissolved oxygen content (5).

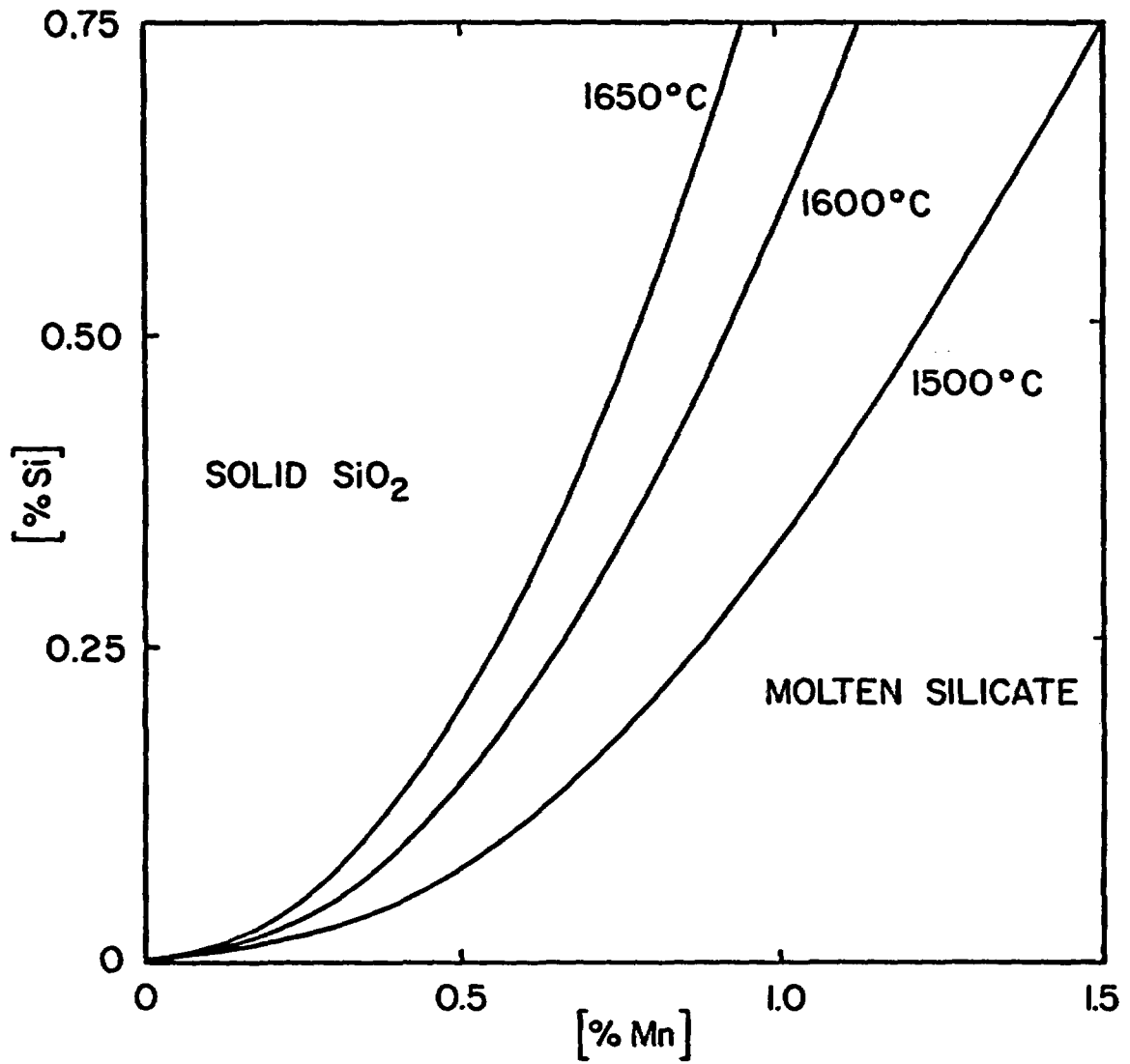


FIGURE 10. Concentration of silicon and manganese in iron in equilibrium with silica-saturated manganese-silicate melts (5).

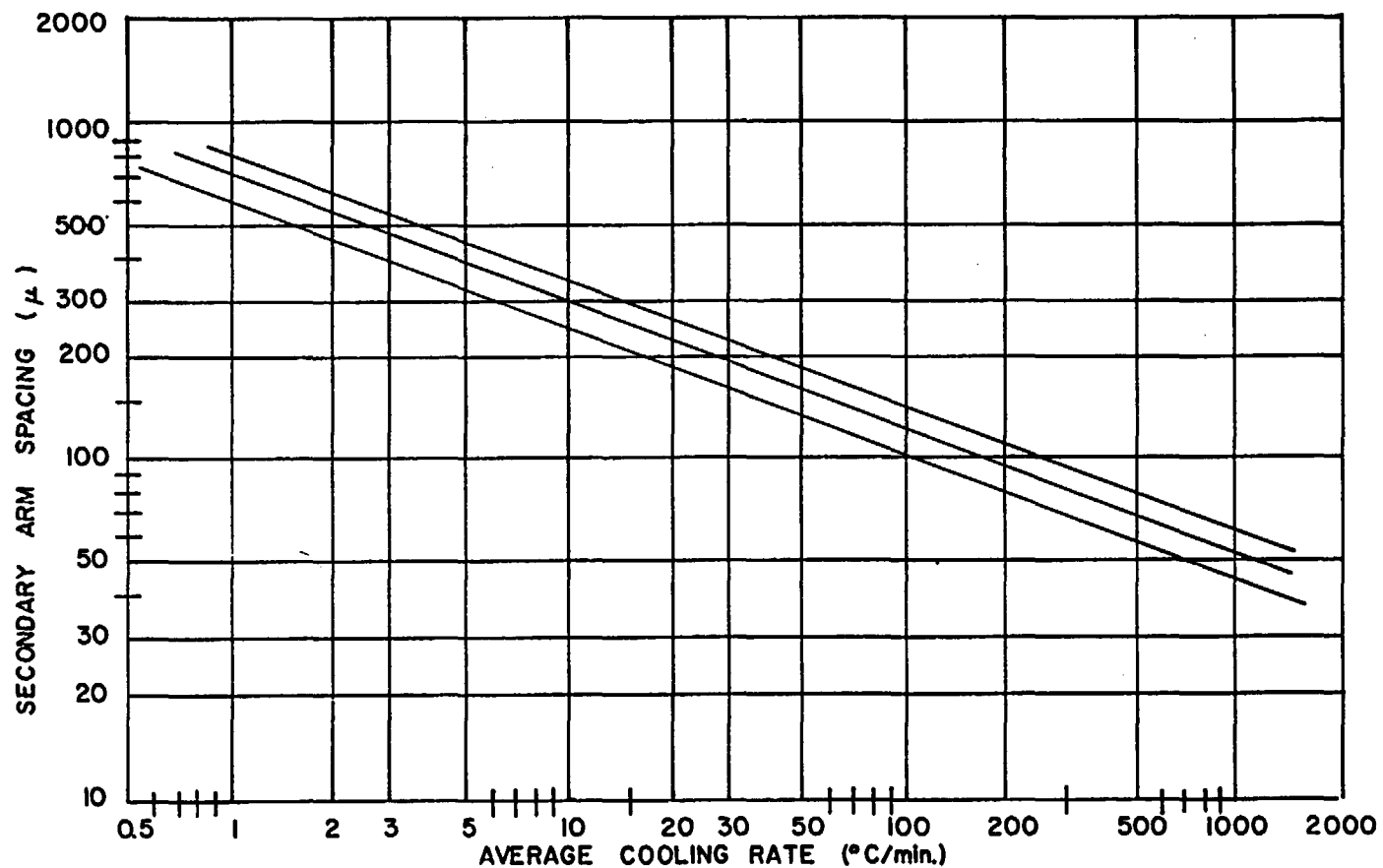


FIGURE 11. Experimental data on dendrite arm spacings in commercial steels containing from 0.1 to 0.9 weight percent carbon (45).

which are representative of standard commercial practice. The submerged arc welds represent a high heat input, slow cooling welding process, and the gas metal arc welds represent a lower heat input welding process with a much higher cooling rate.

Changes in the continuous cooling phase transformation diagram (CCT) were expected to be produced by the variations in the Mn/O ratio and the sulfur level. The presence of oxide and sulfide inclusions can influence the microstructure of the fusion and heat affected zones by limiting austenite grain growth near the fusion line, and by enhancing ferrite nucleation. The grain size and the level of hardenability additions such as manganese have a significant influence on hardenability. An increase in the grain size or in the manganese content cause the ferrite and pearlite curves on the continuous cooling transformation to be shifted back to longer times. The action of oxide and sulfide inclusions to promote ferrite nucleation tends to decrease hardenability and cause the ferrite curves on the CCT diagram to shift to earlier times.

The changes in austenite decomposition reactions caused by changes in heat input and weld metal composition were evaluated by radial dilatometry during cooling of cylindrical Gleeble specimens, and by analysis of SAW and GMA welds. Metallographic analysis were carried out to identify microstructural differences in the weld fusion zone and the heat affected zone. In addition, multipass welds were produced and metallographically evaluated to determine the influence of multiple passes on the microstructures of previous weld beads and heat affected zones.

The third phase of the experimental effort concerned an evaluation of microstructural changes that could occur during long term storage. It was estimated that the thermal experience would include temperatures in the range of 200 to 300°C for periods of up to 50 years. Experiments to determine microstructural changes caused by repository storage were based on the assumption that thermally activated processes, principally carbon diffusion, control the rate of microstructural changes over the life of the container. Thus, long term storage was simulated by heat treating for a shorter period at a higher temperature.

### 3.2 Casting Production and Heat Treatment

The experimental objective of the casting portion of the research program was to investigate the influence of melting and casting process variables on the microstructure of ASTM A-216 grade WCA carbon steel castings. Three compositions within the specification were selected to provide high and low manganese/oxygen ratios, and the addition of sulfur, to investigate the influence of sulfide inclusions. These compositions were given in Table 4.

Steel making was carried out in a coreless induction furnace. Static castings and chill castings were poured and heat treated

by normalizing. These castings were later sectioned and machined to provide specimens for submerged arc and gas metal arc welding, and for Gleeble modeling of thermal histories in the heat affected zone. The solidification structure of large static sand castings was modeled by a solidification experiment carried out inside the induction furnace to slow down the solidification rate. The experimental setup is shown in Figure 12. A number 4 graphite susceptor was lined with asbestos paper, rammed with an Alumina refractory and placed inside the coreless induction furnace. A one inch AISI 1018 steel bar stock was placed in the crucible and covered with a two hole graphite lid. An Alumina protected type R thermocouple was placed in one hole and a hollow Alumina tube connected to argon shielding gas was in the other. The molten charge was slowly cooled by turning the rheostat down on the induction furnace power supply. The time-temperature data obtained from the thermocouple is plotted in Figure 13. Two heats were produced at cooling rates of 0.5°C and 2.0°C. After cooling to room temperature the castings were sectioned for metallographic evaluation of the secondary dendrite arm spacings as a function of the cooling rate (45). Castings to simulate the solidification behavior of the centrifugal casting process were poured in gray iron chill molds. The gray iron book molds were arranged on the ductile iron chill plate and olivine molding sand was rammed between them as shown in Figure 14. This configuration was used to cast all the experimental plate for this investigation.

The steel alloys were produced by air induction melting in a 50 lb. induction furnace using AISI 1028 steel bar stock, electrolytic iron, pig iron for carbon addition, and low carbon ferroalloys. Four heats of pig iron with high carbon and low silicon contents were produced in the 50-pound induction furnace prior to steel making and cast into pig molds for carbon additions. The compositions of the four pig iron heats are shown in Table 5.

TABLE 5 - CHEMICAL ANALYSIS OF PIG IRON

	C	Mn	Si	S
NRC-P1	4.05	-	0.50	0.006
NRC-P2	4.08	0.14	0.30	0.0074
NRC-P3	3.30	0.10	0.10	0.010
NRC-P5	3.74	0.64	0.13	0.010

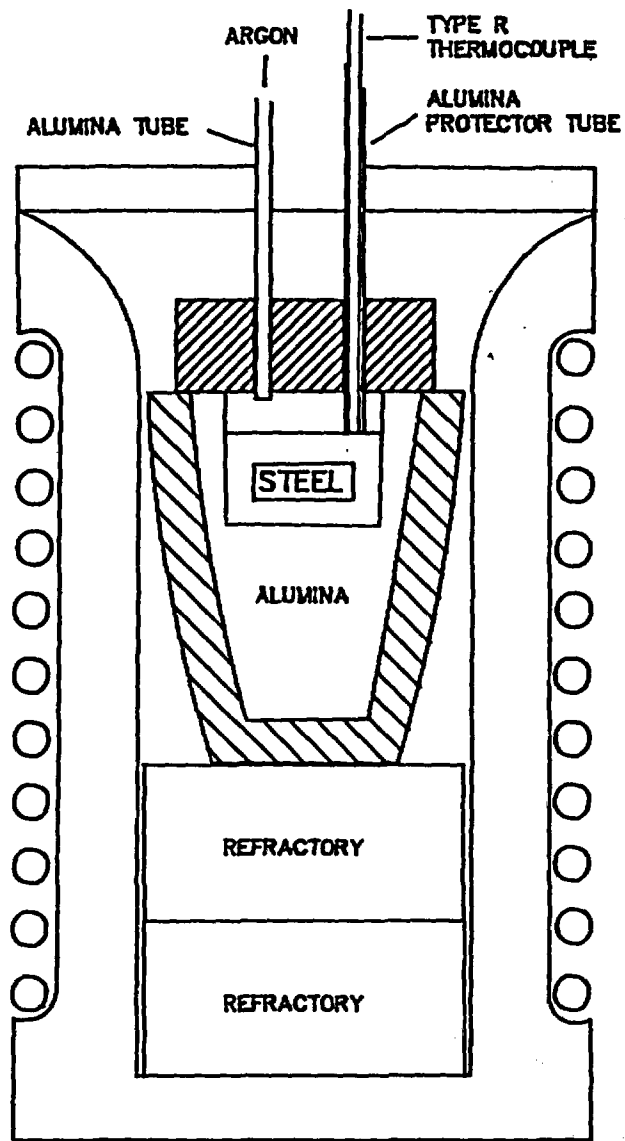


FIGURE 12. A schematic diagram of the furnace solidifying equipment used to model static casting.

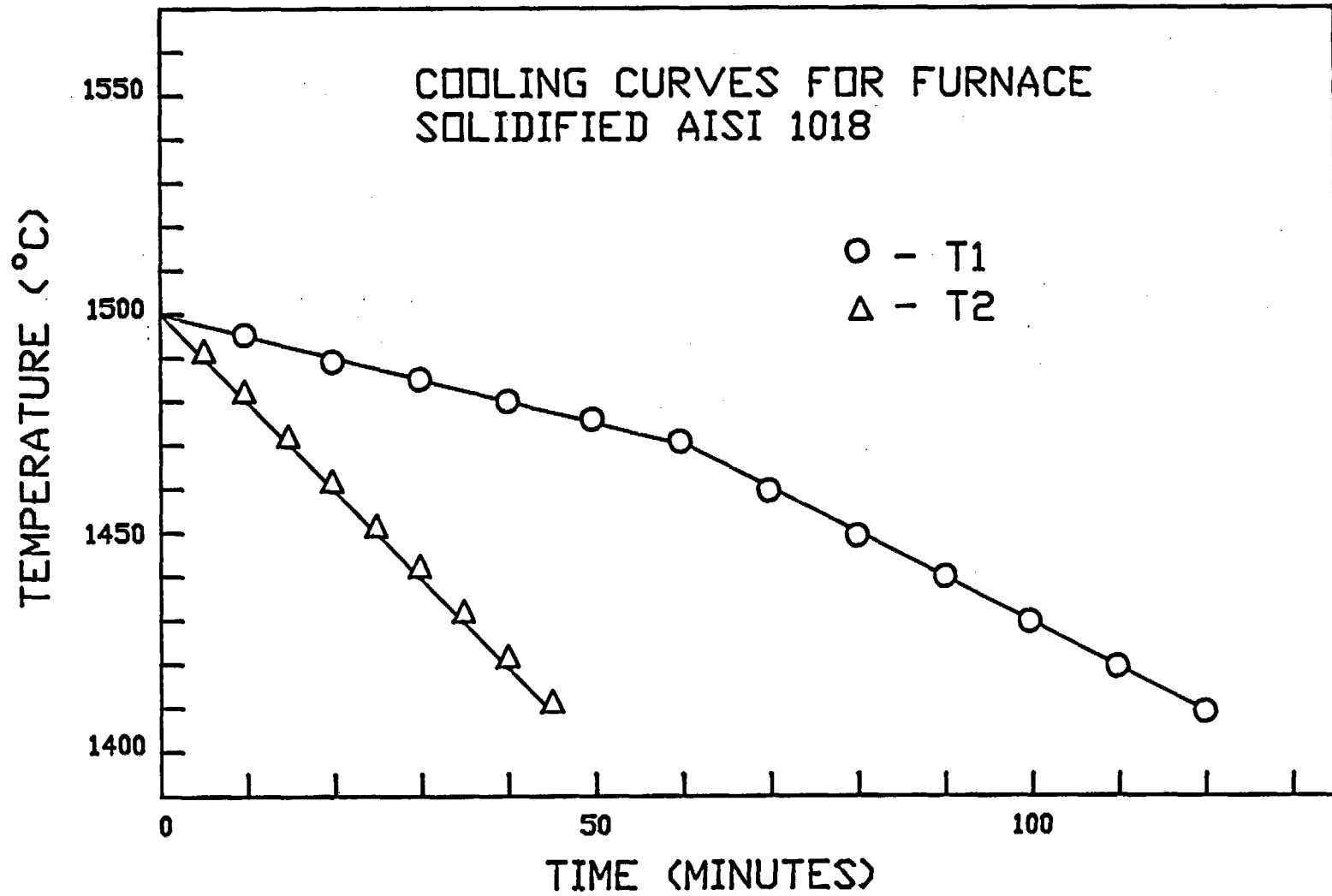


FIGURE 13. Cooling curves obtained from furnace solidified specimens.

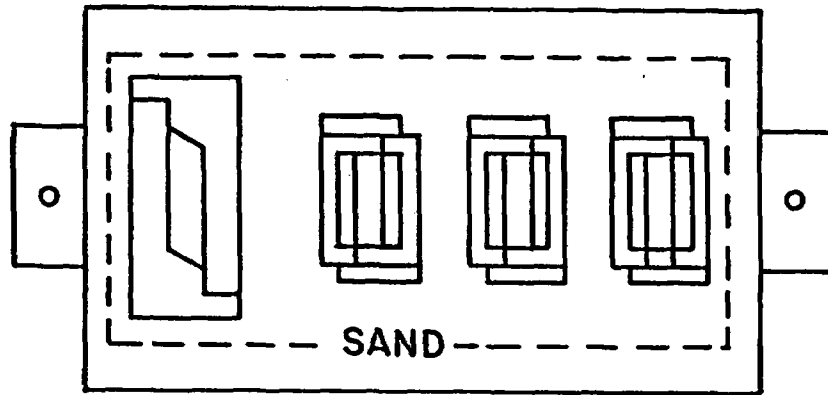


FIGURE 14. Mold configuration prior to tapping steel.

Thirty five heats of steel with compositions corresponding to variations of the compositions in Table 4 were produced by air melting in the 50 pound furnace. An iterative charge calculation technique was used for all heats. Melt logs were kept to document the times and furnace temperatures for alloy additions, furnace and ladle conditions, time spent in the furnace after alloy additions, pouring temperature, tapping temperature, ladle time, and deoxidation additions. Consistent procedures were used for all heats to provide quality control.

The steel melting practice consisted of melting bar stock and electrolytic iron to produce an overoxidized condition at melt down. At meltdown 30 grams of ferrosilicon was added to control any premature boil. Deoxidation was accomplished by the addition of pig iron to bring the carbon level up and promote a carbon monoxide boil. The carbon boil was allowed to go on for exactly five minutes at which time 50 grams of ferrosilicon was added to block the heat. The temperature of the melt was brought up to 1675°C in ten minutes, the balance of the ferrosilicon was added, and the heat was tapped to the ladle. The ferromanganese and one half of the aluminum kill were charged to the ladle before tapping. The remainder of the aluminum kill was charged to the stream during tapping. The slag was removed and the ladle was tapped to the molds. The time for tapping from the furnace and pouring the molds varied from 30 seconds to 2 minutes depending on the desired oxygen content. The high sulfur heats needed an addition of iron pyrite ( $\text{FeS}_2$ ) and that was added cold with the bar stock at the beginning of the heat.

The chemical analyses of the melting stock and the steel heats were obtained by emission spectrometry for alloy and tramp elements and by LECO analysis for interstitial elements. Vacuum emission spectrographic analyses were carried out for silicon, manganese, chromium, nickel, molybdenum, titanium, copper, and various tramp elements. LECO interstitial analyzers were used to determine: carbon, sulfur, oxygen, and nitrogen levels.

The chemical analyses of the melting stock and scrap are given in Table 6 along with analyses of the ferroalloys provided by vendors. These analyses were used for charge calculation purposes, and the melting losses were computed based on the charge calculation and the chemical analysis of the heat. These losses shown are unique to the furnace used, the melting procedure, and the alloy cast. Eight of the steel heats were chosen for welding studies and/or Gleeble investigation of the microstructures as a function of thermal history. The compositions of these steel heats along with the three target compositions are given in Table 7.

TABLE 6 - CHEMICAL ANALYSIS OF MELT ADDITIONS

	%C	%Mn	%Si	%S	%Al	%Ti	BAR
EN201	0.034	0.053	0.003	0.007	-	-	SCRAP
AlSi 1008	0.087	0.41	0.005	0.021	-	-	SCRAP
AlSi 1018	0.021	0.86	0.24	0.02	-	-	SCRAP
FeMn	1.46	80.10	1.46	-	-	-	Med.C.
FeSi	-	-	50.0	-	-	-	Lump
FeS2	-	-	-	53.3	-	-	Powder
Al	-	-	-	-	100	-	Shot
FeTi	-	-	-	-	-	46	Lump

TABLE 7 - Chemical Analysis of Steel Heats

Heat No.	%C	%Mn	%Si	%S	%P	%Al	Mn/O	%O
Alloy A	0.18	0.50	0.10	0.01	0.02	0.05	25	0.0200
Alloy B	0.18	1.00	0.25	0.01	0.02	0.05	145	0.0070
Alloy C	0.18	1.00	0.25	0.045	0.02	0.05	145	0.0070
NRC-5	0.17	0.51	0.10	0.01	0.008	0.043	44.7	0.0114
NRC-12	0.17	1.06	0.32	0.01	0.013	0.050	64.2	0.0165
NRC-14	0.15	1.07	0.21	0.045	0.012	0.054	49.1	0.0218
NRC-15	0.21	1.13	0.20	0.01	0.014	0.030	188.3	0.0060
1	0.25	0.19	0.65	0.015	0.005	0.04	23.8	0.0080
2	0.15	1.04	0.36	0.019	0.006	0.04	130.0	0.0080
3	0.10	1.05	0.64	0.060	0.010	0.04	75.0	0.0140
4	0.14	0.30	0.10	0.018	0.004	0.05	30.0	0.0100

A sample from each heat of the one inch thick cast plate designed for the machining of Gleeble specimens was sectioned for metallographic examination. Each sample was polished to a 0.05 micron Al<sub>2</sub>O<sub>3</sub> finish, etched with two percent nital, examined under a microscope, and photographed.

The specifications for ASTM A-216 grade WCA call for the material to be delivered in the normalized, normalized and tempered, or annealed condition. Normalizing was the chosen condition for this investigation. The standard normalizing treatment consists of austenization at 900°C for one hour per inch of thickness followed by air cooling (176). The ferrite grain size varies with increased section thickness as shown in Table 8 from Volume 7 of the 8th Edition of the Metals Handbook (177). The overpack container designs call for wall thicknesses between three and fourteen inches. Thus, the overpack containers would have a larger grain size than the 1.5 inch thick weld plate cast for this investigation.

TABLE 8 - SUMMARY OF GRAIN SIZES FOR ASTM A-216 GRADE WCA STEEL (177).

Section Thickness	Grain Size (um)
Experimental (1 in.)	18
Volume 7 (1 in.)	22
Volume 7 (3 in.)	36
Volume 7 (6 in.)	41

The cooling rate of a six inch ( 15.24cm) diameter casting cooled from a normalizing temperature of 900°C is approximately 10°C per minute (178). A controlled cooling device designed to allow the one inch thick plates of this investigation to cool at 10°C per minute was constructed, and is shown in Figure 15. The controlled cooling device was calibrated using off-chemistry, cast one inch thick plate with a type K thermocouple mounted in predrilled holes. A heat treatment which consisted of austenization for two hours at 1050°C followed by cooling in the controlled cooling device yielded a room temperature ferrite grain size typical of a six inch section thickness, and that treatment was carried out on all steels of this study.

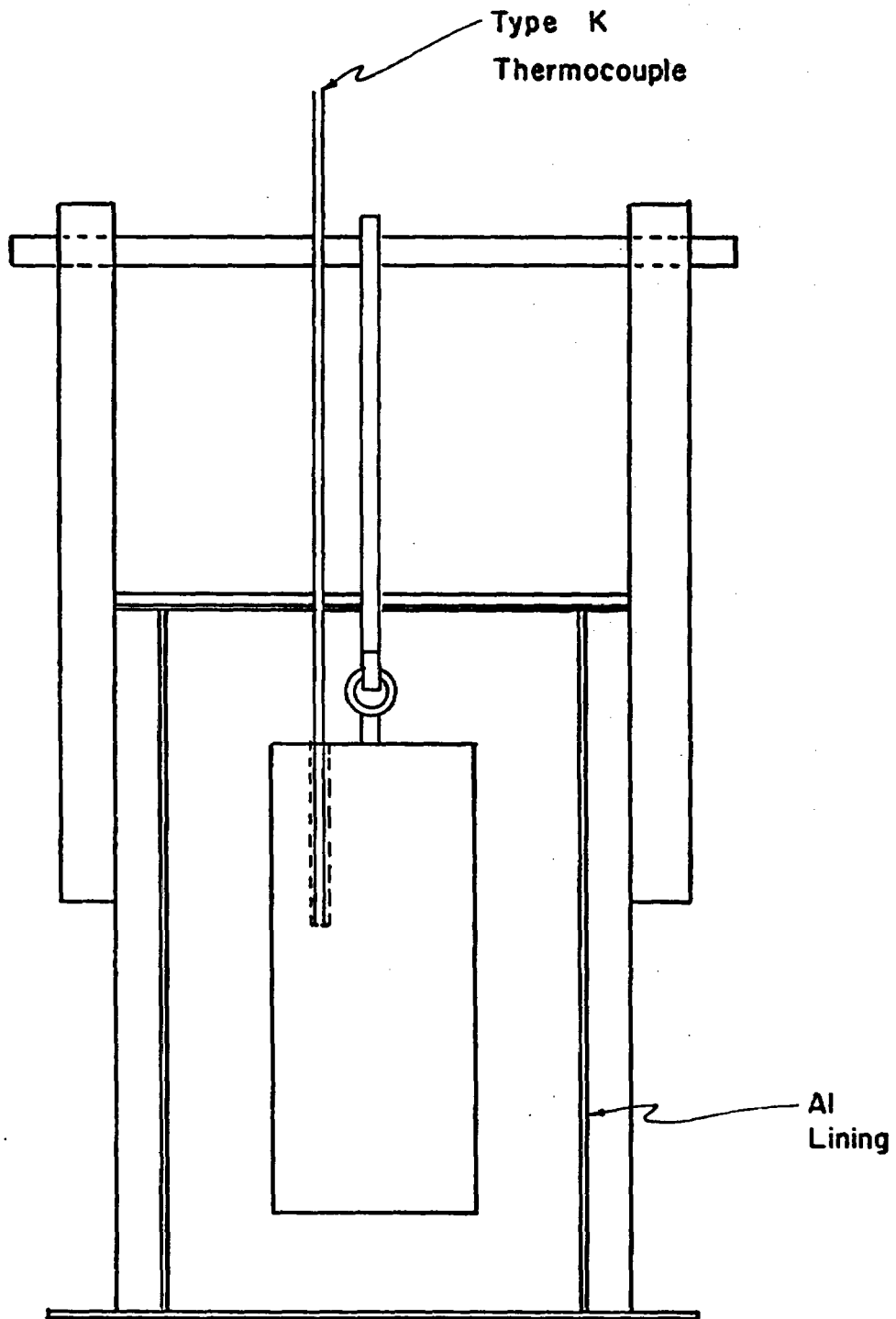


FIGURE 15. A schematic of the slow cooling device used to slow the cooling rate of one inch (25.4 mm) thick plate to that of a six inch (152.4 mm) thick plate.

### 3.3 Welding Experiments

Submerged Arc and Gas Metal Arc welds were carried out on 1.5 inch thick cast plate to investigate the influence of welding process variables and parent plate structure on the properties of the welded assembly. The thermal histories of the multi-pass welds were recorded by thermocouples placed in blind holes in the base plate so that the thermocouple tip was near the fusion line. After normalization the 1.5 inch weld plates were specially normalized they were machined to provide a single sided 30° edge preparation. Two 5/64 inch diameter thermocouple holes were drilled in each weld plate approximately six inches apart as depicted in the figure. The hole depth varied depending on what region of the heat affected zone was monitored. A 0.005 inch diameter bare platinum wire was welded to a 0.005 inch diameter bare platinum 13% rhodium wire using a capacitive discharge 150 volt welder, and a graphite block. The bare thermocouple was welded to the bottom of the predrilled holes using the same capacitor discharge welder. The bare wires were protected by an Al<sub>2</sub>O<sub>3</sub> two hole protector tube which slid over the two wires to prevent short circuiting. The protector tube was cemented in place using an MgO refractory mix and the wires were connected to a type R junction box.

A type R Numatron digital thermocouple monitor was calibrated using a constant voltage generator and readings were adjusted to correspond with tabulated standards (179). The Numatron was then connected to the type R junctions of the weld-plate and used to insure proper wire polarity. Before any thermocouple measurements were made, an evaluation of the parameters which affect the measurements of the temperature device used for this study was carried out. This evaluation included the following considerations: thermal gradient across the hot junction; response time of the wires and hot junction; calibration and precision of the equipment used; and conversion from voltage-time to temperature-time.

Since the heat affected zone in this investigation is approximately 0.125 in. wide, the hot junction must be as small as possible to avoid any thermal gradient across it. A thermal gradient of 150°C is not uncommon in weld thermal cycle measurements (180). The hot junction was kept to 0.010 in. to eliminate any error caused by the dimensions of the hot junction. The response times of the 0.005 inch diameter thermocouple wires were calculated using guidelines set forth in literature (181). The theoretical response time for the thermocouples used was 0.0012 seconds for 0.005 inch wire, however the hot junction was 0.010 inches in diameter making the response time 0.0035 seconds.

At a 500°C/sec. heat up rate, typical for submerged arc welds an error of 1.75°C was possible in the peak temperature. The thermocouple reliability as determined from the ASTM manual on the use of thermocouples was  $\pm 3.75^\circ\text{C}$  between 538°C and 1482°C (182). This gives a total cumulative error of  $\pm 5.50^\circ\text{C}$  with just the system configuration. The small diameter of the

thermocouple wire required that care be taken not to strain or damage it during installation and invalidate the quoted calibration.

A Nicolet 4094 digital recording oscilloscope, which is a fast response time instrument, was used to gather the voltage-time data from the thermocouples. In instruments designed for faster response, other desirable features have been sacrificed. The Nicolet 4094 is no exception. The sensitivities are lower, and thus an amplified signal is better suited for measurements of this kind (181).

A groundless isolation amplifier was placed in the circuitry to amplify the thermocouple signal and filter any eddy currents or stray voltages induced by the welding process (183). A cold junction compensator was also placed in the thermometry circuit. The combination of the errors previously described, and those produced by the amplification circuitry, gave a possible  $\pm 5.50^{\circ}\text{C}$  error in the temperature measurement.

The Nicolet 4094 digital recording oscilloscope was used in combination with an integrated circuit isolation amplifier, cold junction compensator to monitor heat affected zone thermal cycles. Two isolation amplifiers were calibrated by using a constant voltage generator and adjusted according to standard tables (179). The 4094 (with the amplifiers and compensators connected) and the Numatron were attached to a type R thermocouple in a furnace and checked to see if their readings were consistent. The 4094 was then connected through the isolation amplifier and cold junction compensator to the weld mounted type R junction and a setting of 0.3 ms/point was set on the scanner. Two thermocouple locations per weld were monitored with the oscilloscope/amplifier combination, using the two available channels on the 4094. The complete set up is diagramed in Figure 16 (184).

Submerged arc welding was carried out on 1.5 inch weld plate from Heats NRC-3, -4, -5, -8, -9, -10, -11, -12, -13, -14 and -15 using a Hobart RC 500, 500 ampere, dc, 100% duty cycle, constant potential, reverse polarity power supply with remote carriage. A welding voltage of about 25 volts, welding current of around 500 amperes and a travel speed of 12 in. per minute were maintained to give an energy input of about 63 KJ/in., neglecting heat transfer efficiency. A Hewlett Packard two-pen analog chart recorder monitored voltage and current continuously during welding. Tibor 22, 3/32 inch diameter wire, in combination with Oerlikon OP121TT flux was used for welds. An unfused flux depth of 1.25 inches was maintained for each pass, and the fused flux was removed between passes.

For microstructural analysis the welds were further sectioned to isolate the thermocouple hot junction, polished to 0.05 micron finish, etched with a boiling saturated picric acid in methanol with one percent Aerosol OT solution for two minutes to reveal the prior austenite grain size next to the fusion lines. Photomicrographs were taken to record the prior austenite grain

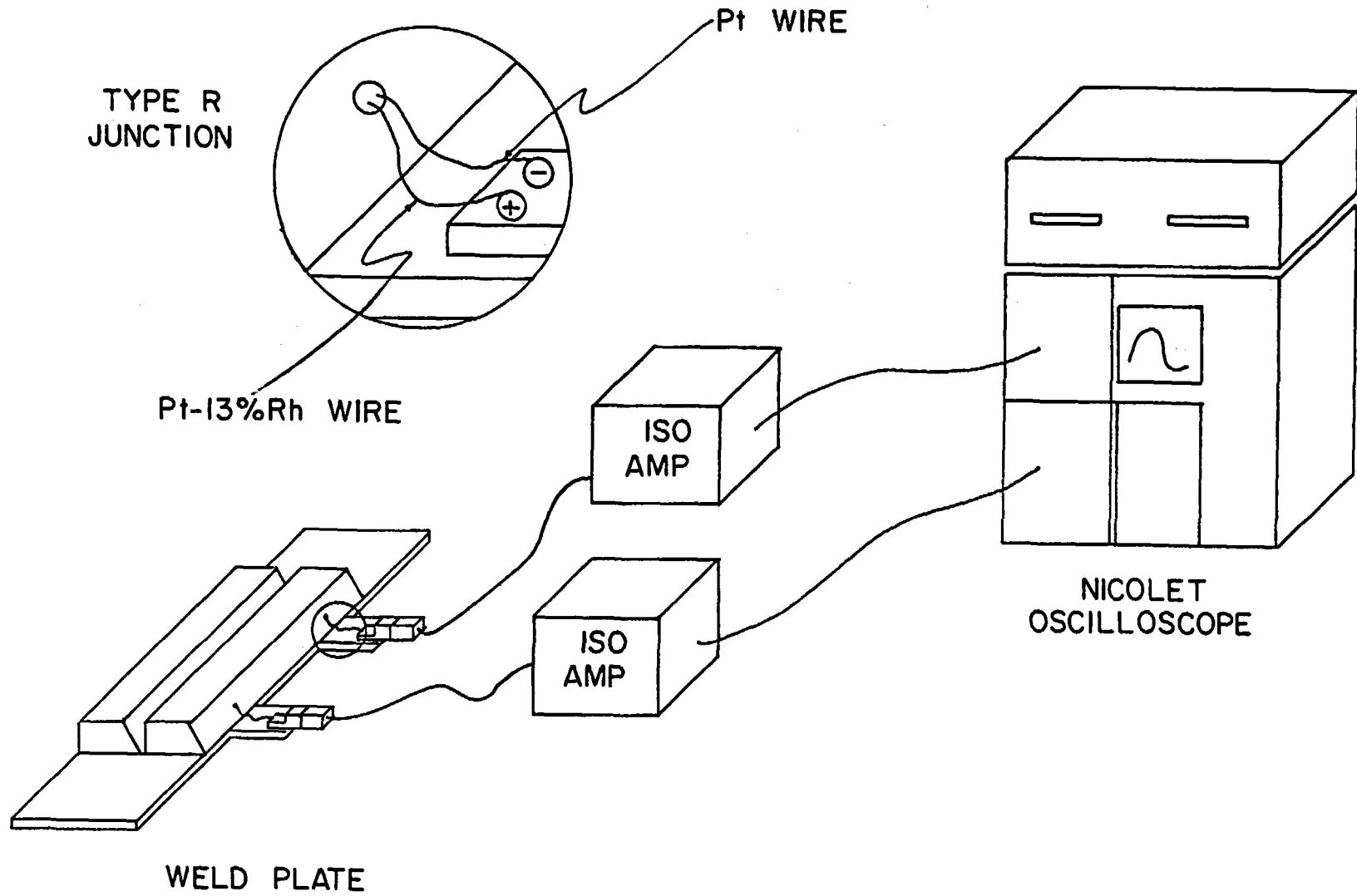


FIGURE 16. A schematic diagram of submerged arc welding setup and instrumentation.

size. The specimens were repolished to remove the picric etch and etched a second time with two percent nital to reveal the structure directly beneath the thermocouple.

### 3.3.1 Weld Microstructures

All gas-metal-arc welding was carried out using a water cooled torch, a Hobart RC 500 constant potential power supply in reverse polarity, and semiautomatic rigging. The cover gas chosen for this experiment was a mixture of 60% CO<sub>2</sub> - 20% Ar - 20% He. The wire selected was a solid E70-S 1/16" electrode. This electrode yielded a weld metal composition at the center of a multiple pass weldment of 0.07% carbon, 0.48% manganese, 0.16% silicon, and 0.06% sulfur.

An initial study utilized bead on plate welds to investigate the acceptable ranges for welding variables in order to evaluate possible heat input levels and deposition ratios. The beads were inspected for defects and were defined as unacceptable if they exhibited: (i) porosity, (ii) undercutting along the edges of the bead, (iii) humping of the bead, or (iv) lack of penetration or fusion. The results of the process space boundary study are shown in Figures 17 and 18. These figures show the process space within which acceptable welds can be produced in deposition ratio - weld travel speed coordinates. The two heat input levels are 1.5 and 2.0 MJ/m. The process conditions for acceptable welds are marked "A", and those for unacceptable welds are marked with a "U". The diagrams show that the greatest process latitude is achieved at the heat input level of 1.5 MJ/m.

After the process spec investigation a series of single pass welds were then made to: (1) provide a basis of comparison of HAZ structures in single and multipass welds; (2) to evaluate the effects of heat input on the different alloys; and (3) to evaluate the peak temperatures and cooling rates associated with GMA welding heat inputs. These welds were made on one half of the test block from each heat using the welding parameters shown in Table 9. Each pass was made without preheat, and was instrumented to record the thermal history.

TABLE 9 - PARAMETERS USED FOR SINGLE PASS GMA WELDS

Deposition Ratio	Wire Speed cm/s	Travel Speed cm/s	Heat Input MJ/m	Arc Voltage Volts	Welding Current Amps
0.20	7.0	0.69	1.0	24.7	280
0.30	8.2	0.54	1.5	27.8	291
0.40	7.0	0.36	2.7	29.0	270

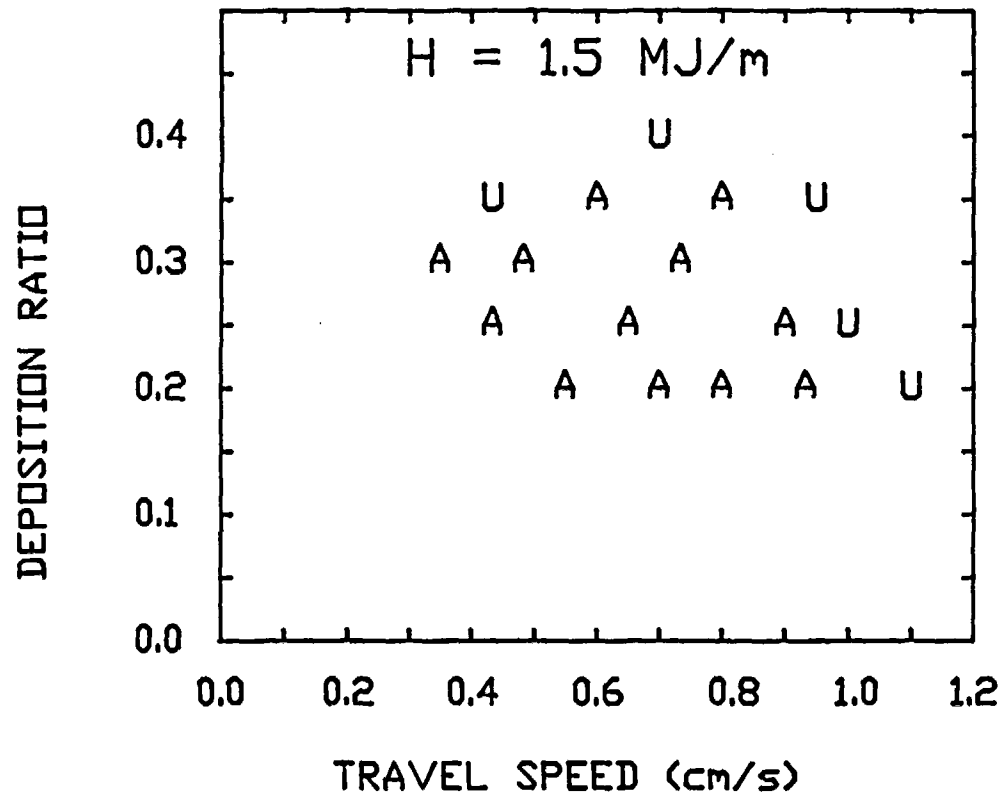


FIGURE 17. Experimentally determined process space for a heat input of 1.5 MJ/m.

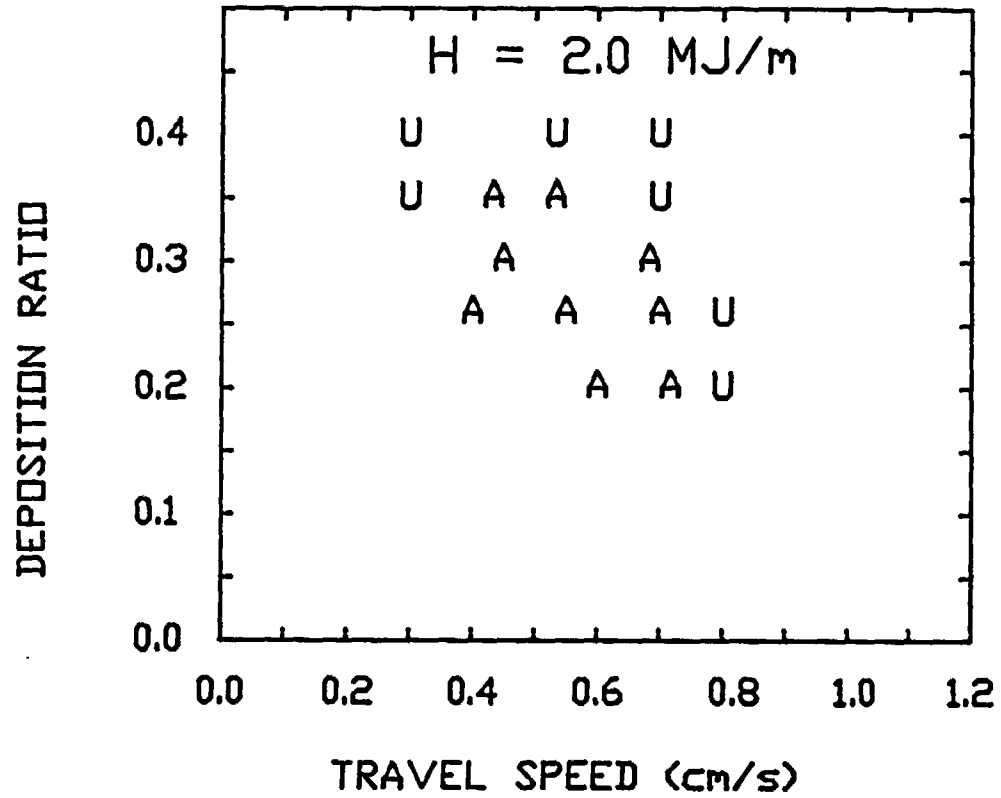


FIGURE 18. Experimentally determined process space for a heat input of 2.0 MJ/m.

After completion of the single pass welds, two sets of multipass GMA welds were made using the joint configuration shown in Figure 19. Each pass was made at a nominal heat input of 1.5 MJ/m using an arc voltage of 27.8 V, a welding current of 291 amperes, a wire speed of 8.2 cm/s, and a weld travel speed of 0.54 cm/s. This power input level was shown to provide a refined weld microstructure. The thermal profiles were recorded for each pass using the same equipment and techniques as those used for the submerged arc welds.

Metallographic evaluations were made of both the single pass and multiple pass welds on sections transverse to the welding direction. The sections were polished and etched in a boiling picric acid solution with a 1% Aerosol O.T. as a wetting agent. This etch was used to reveal the prior austenite grain size in the grain growth region of the heat affected zone.

### 3.3.2 Thermal Profiling

The thermal data for the submerged arc and gas metal arc welds was stored on a disk in the Nicolet 4094 oscilloscope in terms of voltage versus time for the thermocouple. The voltage-time data was transmitted to an IBM AT personal computer, and converted to temperature-time using a ninth order polynomial (179). The temperature-time data was filtered by appropriate programming, to print every 10th data point. Each profile was recorded using 7936 points, and the filtering program reduced this to 794 thermal data points. These data were further manually sorted to yield 50 thermal data points which could be programmed for Gleeble 1500 simulation of heat affected zone thermal history.

The temperature-time data obtained from the welding experiments was plotted, and the experimental curves were matched with the 3-dimensional heat flow equations presented by Rosenthal (184). Supplementary data from the Welding Institute (185) coincided with measured data. These data were used along with a modification to the Rosenthal equation presented by Tsi (186) to provide a reasonable representation of the thermal profiles.

The weld thermal cycle is a function of the energy input, the weld velocity, the thermal properties of the base metal and filler metal, and other welding process variables. The energy input from a welding arc is given by:

$$q = \eta VI \quad (28)$$

where:  $\eta$  = arc efficiency

(0.9 to 0.99 for submerged arc welds)  
(0.7 to 0.8 for gas metal arc welds)

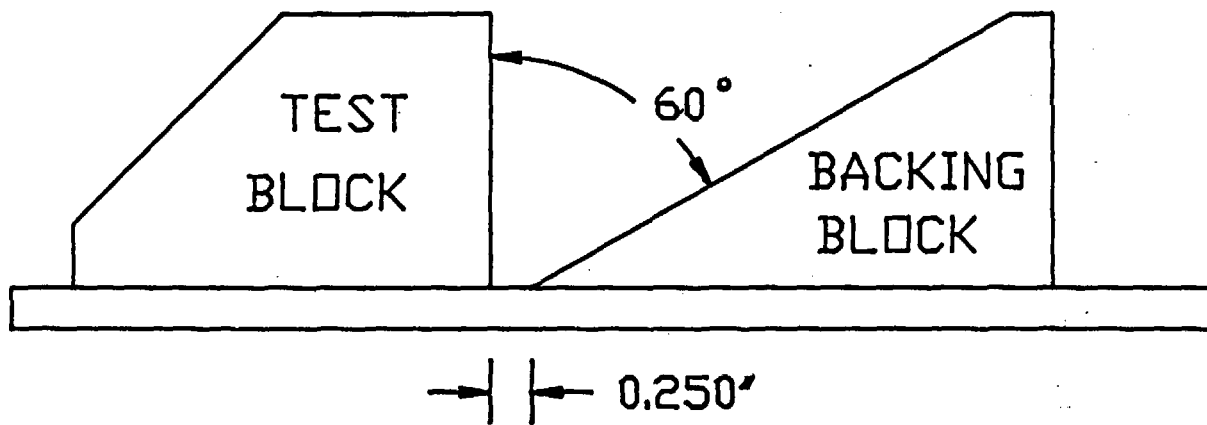


FIGURE 19. Joint configuration used for multiple pass welding.

Following the analysis of Easterling (67), the temperature as a function of time and position for a point source of heat moving at a velocity (v) can be represented by the partial differential equation for unsteady heat transport:

$$2\lambda \frac{\partial^2 T}{\partial \tau^2} = \frac{\partial^2 T}{\partial x^2} + \frac{\partial^2 T}{\partial y^2} + \frac{\partial^2 T}{\partial z^2} \quad (29)$$

where  $\lambda$  = thermal conductivity

This equation can be simplified by assuming quasi steady state conditions in which the isotherms are moving at the same velocity as the heat source, and by using a coordinate transformation to account for the movement of the heat source:

$$\xi = x - vt \quad (30)$$

The simplified differential equation is then:

$$-2\lambda v \frac{\partial T}{\partial \xi} = \frac{\partial^2 T}{\partial \xi^2} + \frac{\partial^2 T}{\partial y^2} + \frac{\partial^2 T}{\partial z^2} \quad (31)$$

This equation applies to welds of thick material, such as those encountered in overpack containers.

If the source moves at a constant velocity, the thermal properties of the base material are assumed not to depend on the temperature, and heat losses from joule heating and surface effects are negligible; then an approximate solution for the three dimensional case can be found:

$$T - T_0 = \frac{q/v}{2\lambda\pi r} \exp\{-r^2/4at\} \quad (32)$$

where:  $T_0$  = initial temperature  
 $q$  =  $\eta VI$   
 $h$  = arc efficiency  
 $V$  = arc voltage  
 $I$  = current  
 $\lambda$  = thermal conductivity  
 $r = (\epsilon^2 + y^2 + z^2)^{\frac{1}{2}}$   
 $\epsilon = x - vt$   
 $t$  = time  
 $y$  =  $y$  coordinate of interest  
 $x$  =  $x$  coordinate of interest  
 $a$  = thermal diffusivity =  $\lambda / \rho C$   
 $\rho$  = density  
 $C$  = specific heat

Empirical modifications to the Rosenthal Equation were used to describe the higher peak temperatures that were unable to be measured in the heat affected zone. The experimental curves show that heating is faster than predicted by Rosenthal and cooling is slower. These differences are caused by the fact that the specific heat, thermal conductivity, and density of steels are not constant as assumed in the Rosenthal derivation. The thermal conductivity for various steel alloys changes substantially over the temperature region of interest in welding. Figure 20 from Geiger and Poirier (187) illustrates the variation in thermal conductivity with temperature for seven different steel alloys.

If these variations in thermal properties were incorporated into the Rosenthal equation its accuracy would improve; however, it could no longer be integrated to its present form and a numerical solution would be required (184). Numerical approaches such as this, or finite element analyses such as those used by the Welding Institute (184) are beyond the scope of this investigation. Instead an empirical approach based on modification of the thermal conductivity was used to model the thermal histories of the submerged arc welds, so that the weld thermal cycles could be reproduced using the Gleeble 1500.

On the heat-up cycle, Rosenthal's equation was too slow, and a higher thermal conductivity was inserted to match the experimentally observed heating rates. For the cooling cycle a second Rosenthal equation was used with a lower value of the thermal conductivity so that the predictions matched the observed experimental cooling rates. Thus, two equations were used, one with a high thermal conductivity for heating, and one with a low thermal conductivity for cooling. The curves MR11092, MR111 and MR1111 are these modified equations plotted, along with the experimental curves, 15W12, 14W11, 112W10, 12W9 and the curve derived by the Welding Institute (WI-1) in Figure 21. The curves shown in Figure 21 were typed into the Gleeble 1500 weld simulator and used for heat affected zone modelling of steels from heat NRC-5, NRC-12, NRC-14 and NRC-15.

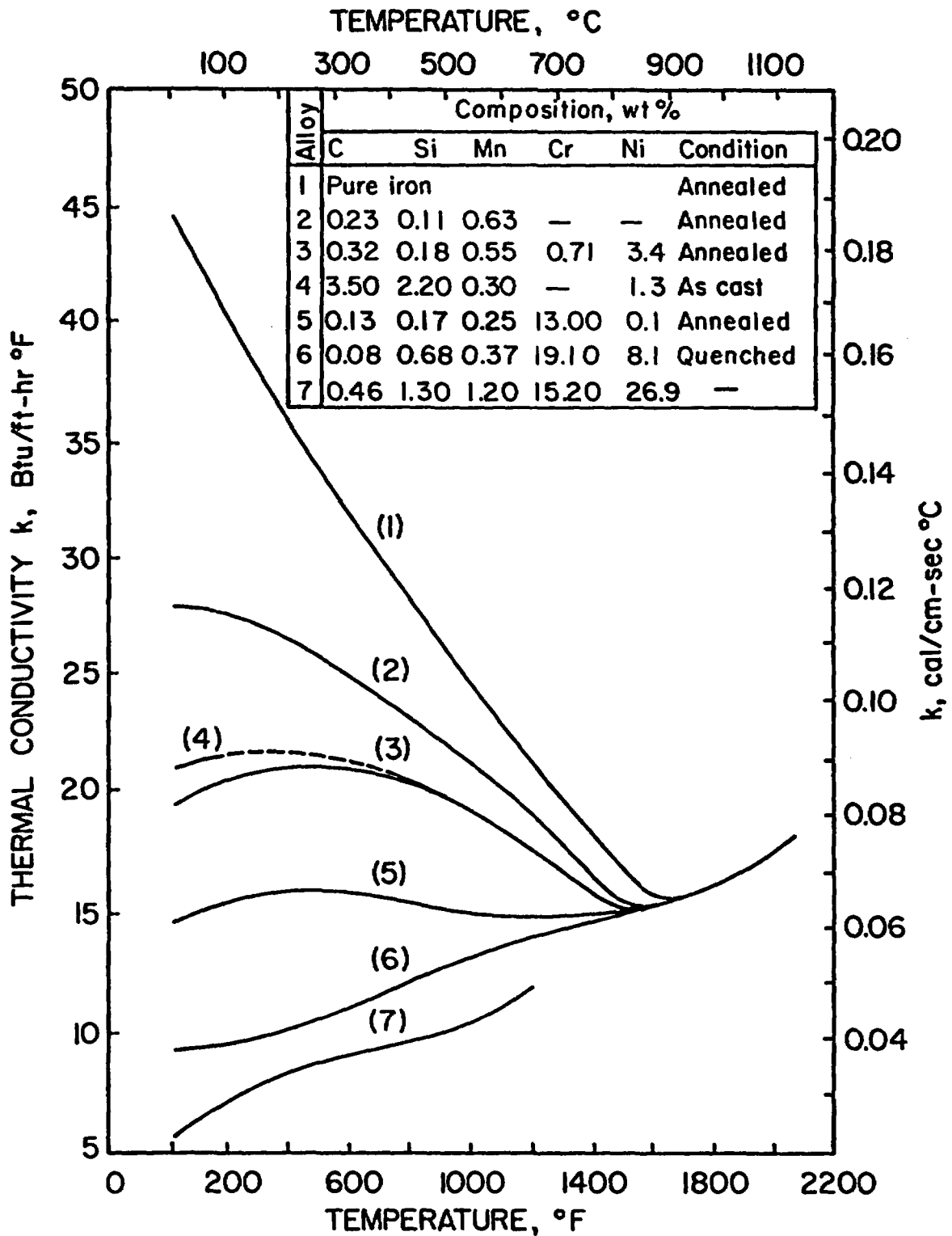


FIGURE 20. Changes in thermal conductivity with temperature for a variety of steels.

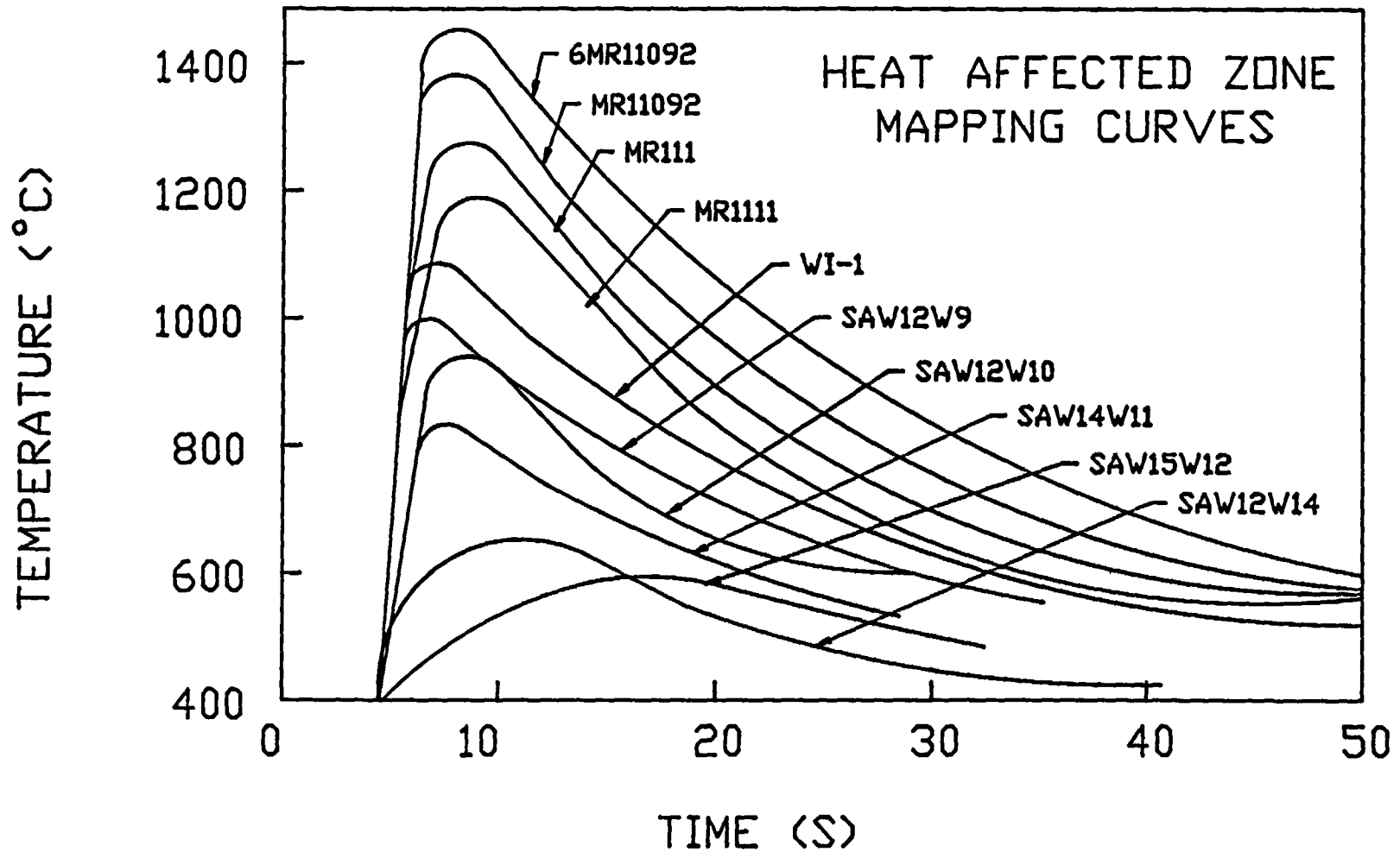


FIGURE 21. Experimentally measured and analytically derived thermal profiles describing specific areas in the heat affected zone.

The three most important factors in determining the microstructure of the heat affected zone are the peak temperature ( $T_p$ ), the cooling rate, and the relative strength of the heat cycle. The cooling rate below the eutectoid temperature is usually approximated by the cooling time from 800°C to 500°C. The amount of time spent at temperature is important because it is indicative of the number of atomic jumps that can occur; and thus, of the amount of microstructural rearrangement which may take place. The peak temperature reached at some point,  $r$  in the heat affected zone can be shown to be (67):

$$T_p = T_o + \left(\frac{2}{\pi e}\right) \left(\frac{q/v}{\rho cr^2}\right) \quad (33)$$

The time spent between 800°C and 500°C is given by (188):

$$\Delta T_{8-5} = \frac{q/v}{2\pi\lambda} \left\{ \frac{1}{773-T_o} - \frac{1}{1073-T_o} \right\} \quad (34)$$

Easterling et. al. (67, 188, 189) have represented the kinetic strength of the heat cycle by:

$$I = \alpha \tau \exp(-Q/RT_p)$$

where:

$$\alpha = 3(RT_p/Q)^{1/2}$$

$$\tau = Aq/(2\pi e\lambda v(T_p - T_o))$$

$Q$  = activation energy for diffusion controlled processes of interest.

$T_p$  = peak temperature of heat cycle.

Figure 22 gives the peak temperatures as a function of distance from the fusion line for GMA welds with a heat input of 1.5 MJ/m. Figure 23 gives the cooling time from 800°C to 500°C ( $\Delta T_{8-5}$ ) as a function of the energy input.

### 3.3.3 Gleeble Simulation

Twelve specimens from each heat, NRC-3, 5, 12, 14 and 15, were machined from the specially normalized Gleeble plate to 0.250 inch diameter, 4 inch long cylindrical specimens for use in the Gleeble 1500. The machined samples were mounted in the Gleeble weld simulator. The span between the jaws was maintained constant at one inch. On samples where the peak temperature was below 1200°C a type K thermocouple was welded to the specimen to monitor the induced thermal cycle. Above 1200°C a type R thermocouple was used. The thermoprofiles were recorded on an analog chart recorder which is part of the Gleeble 1500 unit. On samples where peak temperature were below 1000°C the full scale

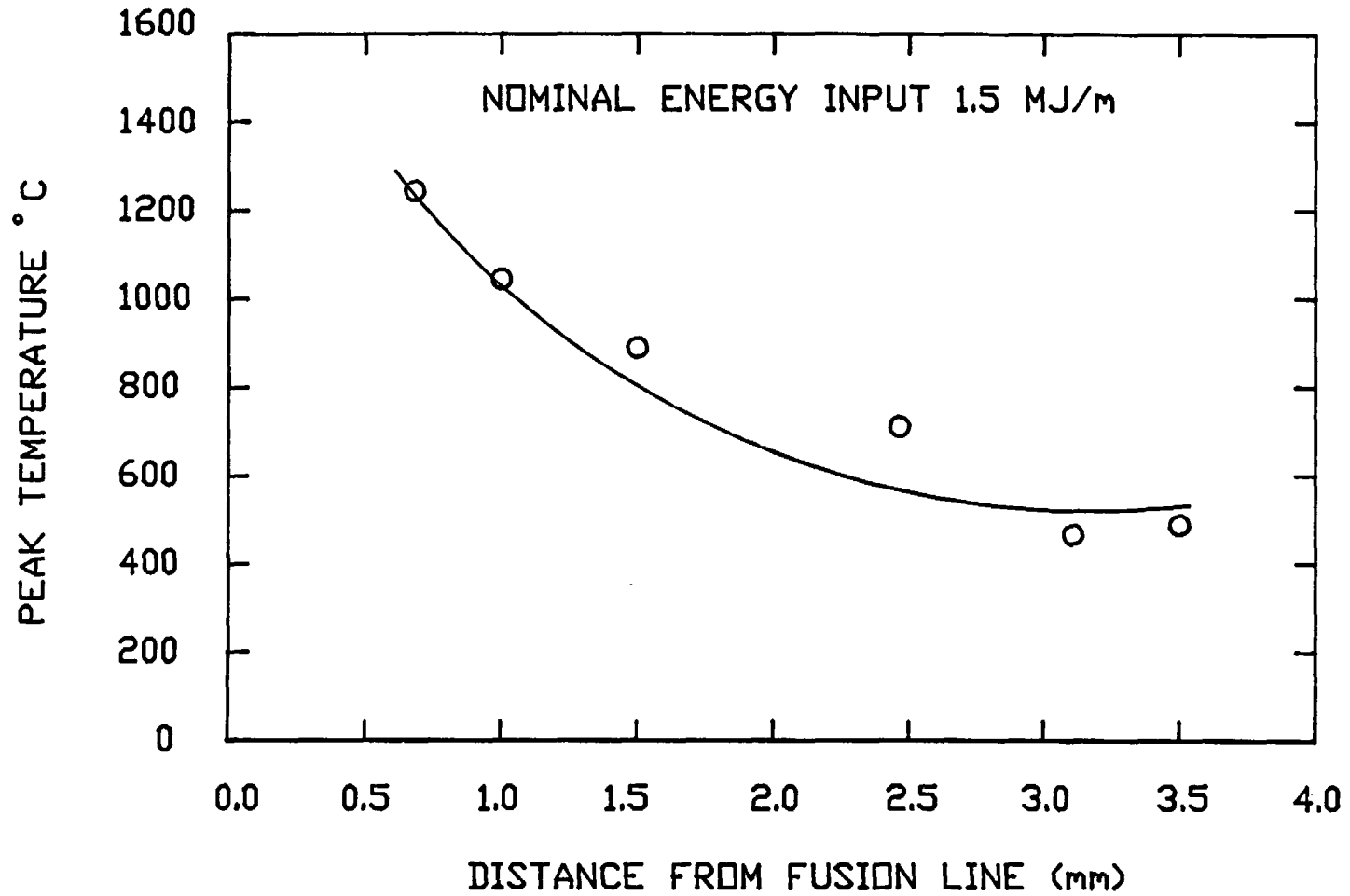


FIGURE 22. Measured peak temperatures versus distance from the fusion line for a heat input of 1.5 MJ/m.

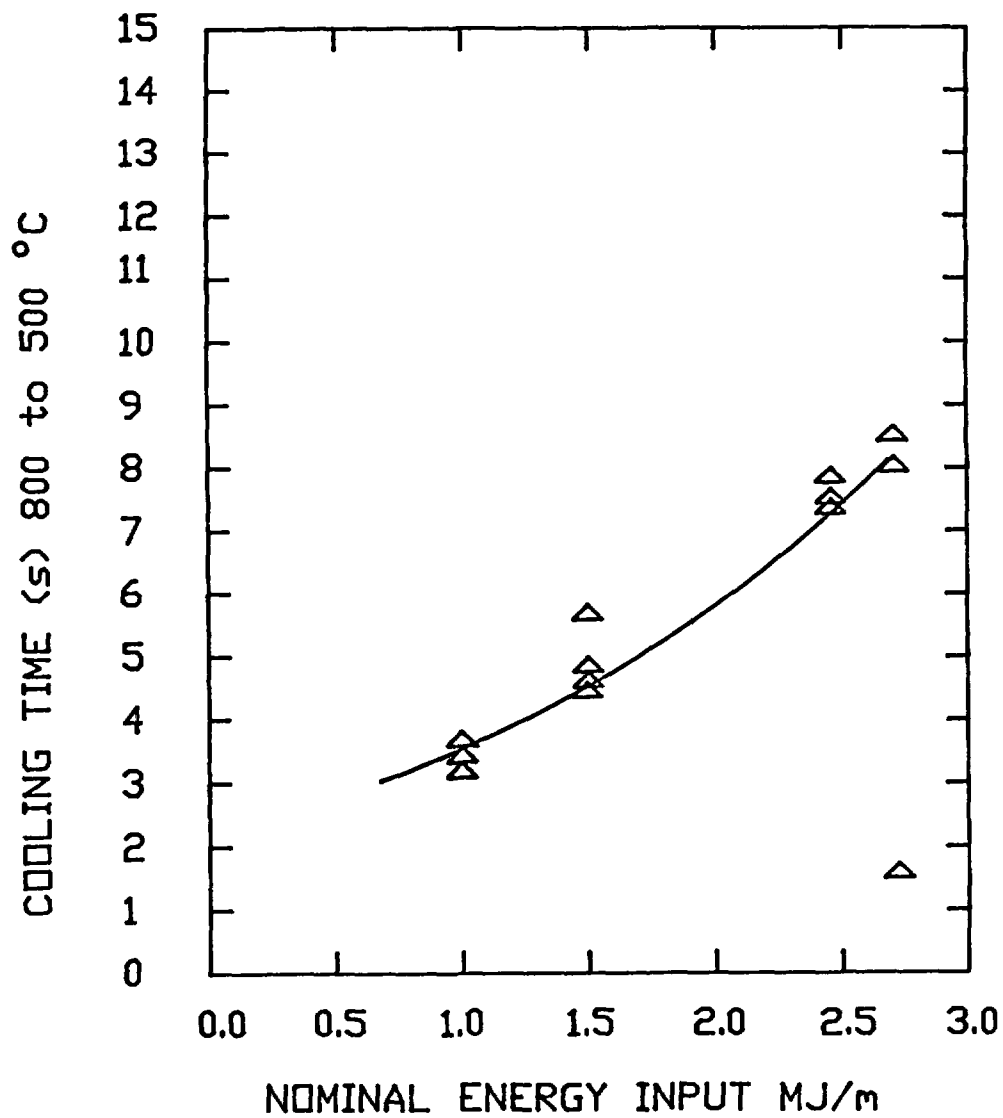


FIGURE 23. Measured and theoretical  $t_{8 \rightarrow 5}$  times as a function of heat input.

setting on the chart recorder was one volt (1000°C full scale). Above 1000°C the full scale setting was two volts (2000°C full scale). The chart speed was 40 cm/min. with the coordinate setting on Y-vs-t. After thermal cycling the Gleeble specimens were sectioned directly beneath the thermocouple hot junction and polished to an 0.05 micron Al<sub>2</sub>O<sub>3</sub> finish. All specimens were etched in two percent nital and photographed. Specimens where the prior austenite grain boundaries were not decorated with allotriomorphic ferrite, were repolished and etched with saturated picric acid in methanol with one percent Aerosol OT and rephotographed. The microstructures were compared to the microstructures of the actual welds and the Gleeble 1500 was evaluated as a tool to model heat affected zone microstructures on cast steel. In addition the microstructures generated by the Gleeble were examined to find microstructural differences caused by variations in cleanliness and alloy composition between samples.

### 3.3.4 Discussion of Welding Experiments

Variations in the Mn/O ratio and the sulfur content within the ASTM A-216 specification are expected to shift the continuous cooling transformation curves and cause changes in the microstructure and properties of the heat affected zone in multipass submerged arc welds. These influences on austenite decomposition can be illustrated using the continuous cooling transformation curve for AISI 1018 steel as shown in Figure 24 (190). An increase in hardenability causes a shift of the ferrite and pearlite curves on the CCT diagram to longer times. Oxide or sulfide inclusions in the 0.3 to 1.0 micron size range promote ferrite nucleation, and cause a shift of the ferrite and pearlite curves on the CCT diagram to shorter times.

The post weld microstructure in the heat affected zone has an important influence on weld toughness. Large fractions of blocky grain boundary ferrite, bainite, or martensite yield poor toughness (67, 191). The best toughness is provided by acicular ferrite which nucleates in the interior of the grain as well as at the grain boundary at an undercooling below the temperature for the formation of blocky ferrite. Acicular ferrite is promoted by the presence of oxide inclusions in the correct size range to act as nucleation sites, and by reduced levels of hardenability agents which promote the formation of bainite.

The influence of cleanliness on heat affected zone microstructures in submerged arc welds was evaluated using heats NRC-5, NRC-12, NRC-14, and NRC-15. Table 7 shows a comparison of the chemical analyses of these heats with those of the three target alloy compositions: Alloys A, B and C. Figure 25 shows a comparison of the cleanliness inclusion distributions of the four experimental cast steels using photomicrographs of the polished and unetched structures. Alloy A was designed to have a low Mn/O ratio to provide a low hardenability and a high concentration of oxide inclusions to act as nucleation sites for acicular ferrite. The composition of Heat NRC 5 (top left in Figure 25) is close to the target Alloy A with the exception that the oxygen level is

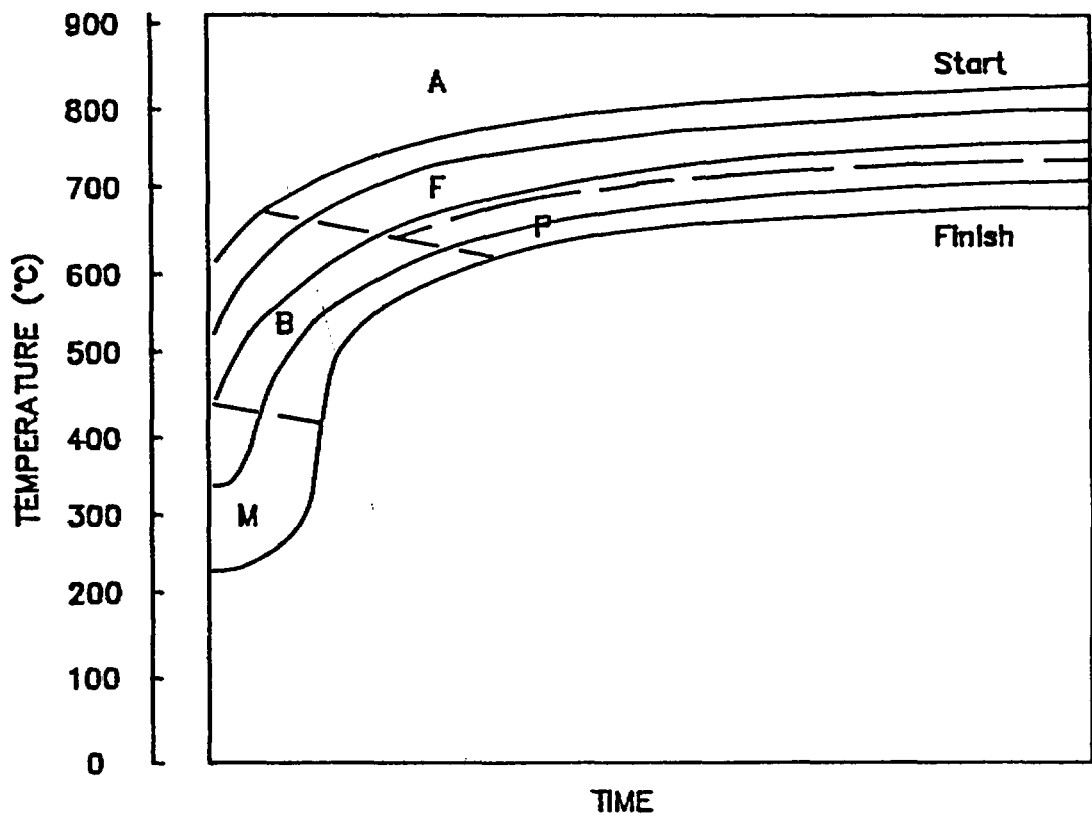
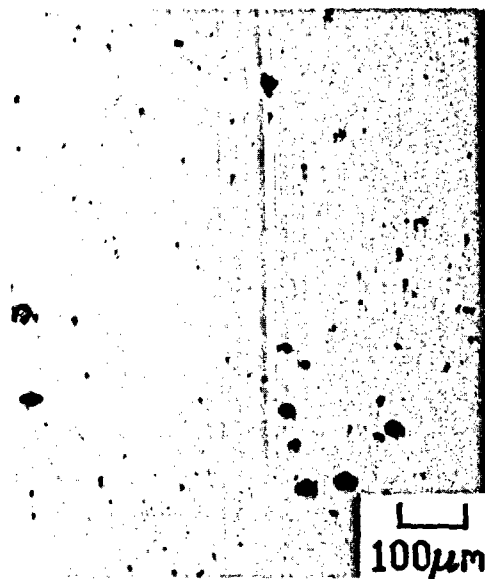
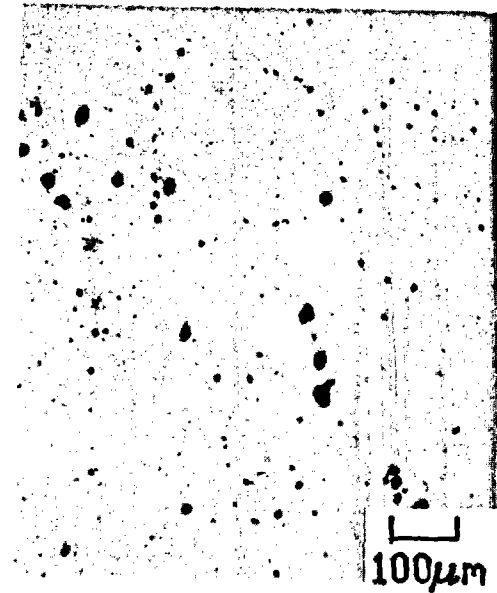


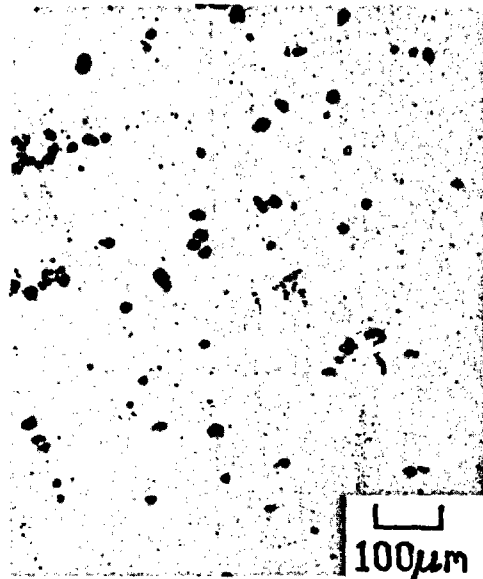
FIGURE 24. Continuous cooling transformation diagram for AISI 1018 steel (35).



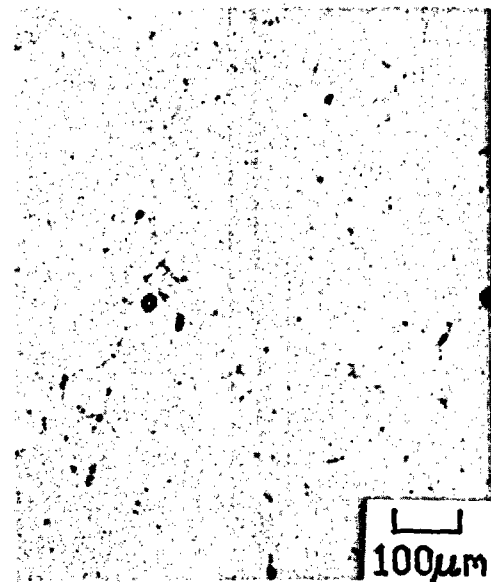
NRC-5



NRC-12



NRC-14



NRC-15

FIGURE 25. Unetched photomicrographs of the four steel compositions showing the nonmetallic inclusions. (100X)

slightly smaller (110 ppm vs. 200 ppm.) and the manganese/oxygen ratio is slightly higher than the target (35 vs. 25). The large inclusions in the micrograph are sulfides. The oxide inclusions are much smaller than the sulfides and they are present in much larger numbers.

Heat NRC 12 (top right in Figure 25) is close to target Alloy B, except for a high oxygen composition which yields a lower Mn/O ratio. Since both the oxygen and manganese values are higher than those in Heat NRC 5, the population of oxide inclusions is greater, and the hardenability is lower. Heat NRC 14 (bottom left of Figure 25) has a very high oxygen concentration, a high manganese concentration, a low Mn/O ratio, and a very high sulfur concentration compared to the other heats used in the study.

The microstructure of NRC 14 shows a substantial concentration of large sulfide inclusions as well as a large number of small oxide inclusions. Heat No. 14 is expected to have the lowest hardenability of the four alloys studied.

Heat NRC 15 (bottom right in Figure 25) is close to target composition B with a low oxygen content, a high manganese content, a high Mn/O ratio, and a low sulfur content. This alloy is expected to have an increased hardenability, and a small population of oxide inclusions to act as acicular ferrite nucleation sites. The microstructure of NRC 15 shows a much smaller concentration of sulfide and oxide inclusions than that found in the other heats, and it was expected that the hardenability would be increased and the development of acicular ferrite suppressed.

The heat affected zone shows a wide variety of microstructures depending on the heat input, the base plate composition, the composition and distribution of nonmetallic inclusions, and the preweld and postweld heat treatments. The welds and Gleeble specimens were used to correlate the heat affected zone microstructures obtained for the four alloys with the alloy composition, cleanliness, and the thermal cycles experienced.

Figure 26 shows micrographs of the HAZ region in a multi pass A-216 steel weld from the present study. The top micrograph shows the fusion line and the grain growth region, the center micrograph shows the recrystallized zone, and the bottom micrograph shows the partially transformed and tempered regions.

Figure 27 shows a comparison of the heat affected zone microstructures obtained for the four steel compositions for the case in which the peak temperature was above 1100°C, and Figure 28 is a comparison of the same four microstructures at a higher magnification. In the temperature range between 1100 and 1520°C found near the fusion line the transformation to austenite is complete, grain growth and particle dissolution significantly change the structure, and base metal composition and cleanliness become important variables. Heats 5 and 12 have low sulfur contents and low and medium Mn/O ratios respectively. The heat affected zone microstructures for these compositions show

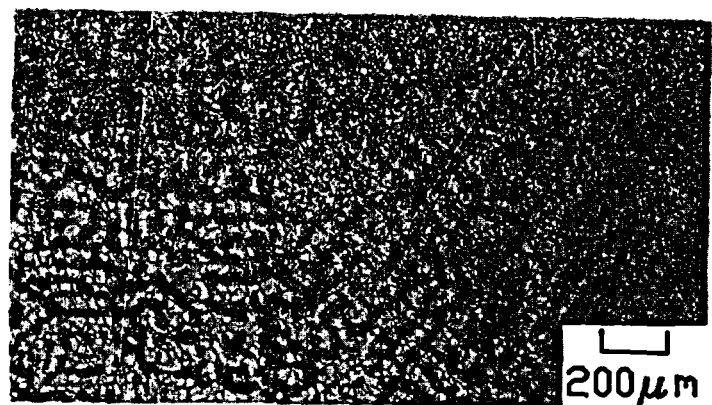
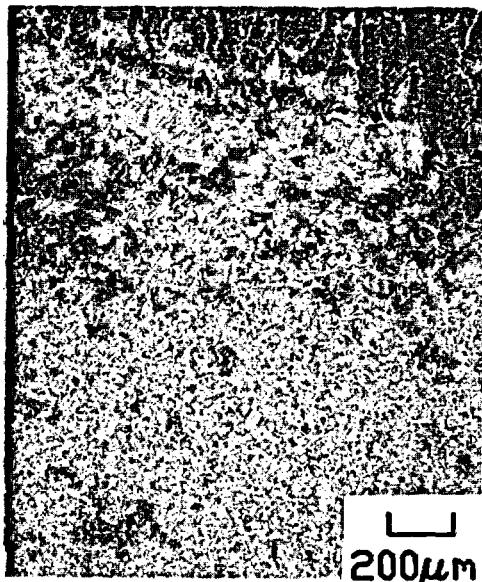
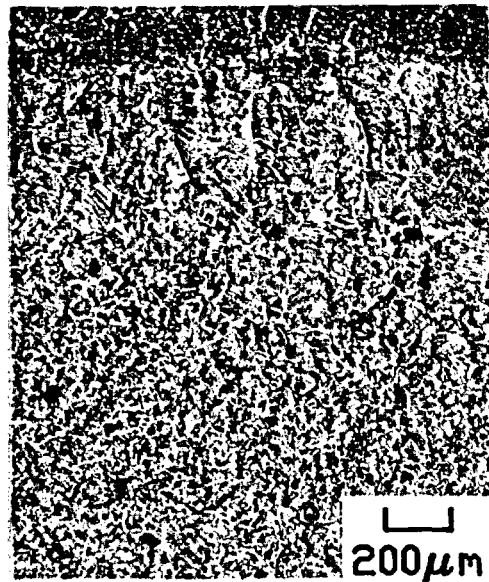


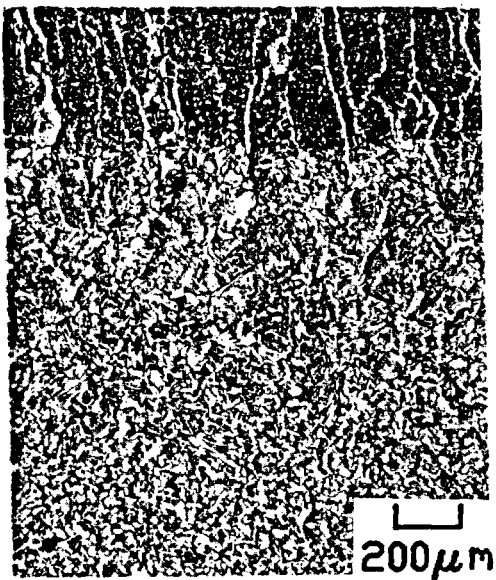
FIGURE 26. Photomicrographs of the four heat affected zone subzones in an off chemistry experimental weldment. The top micrograph shows the fusion line and grain growth region, the middle is recrystallized zone, and the bottom shows the partially transformed zone and tempered zone. 2% nital 50X



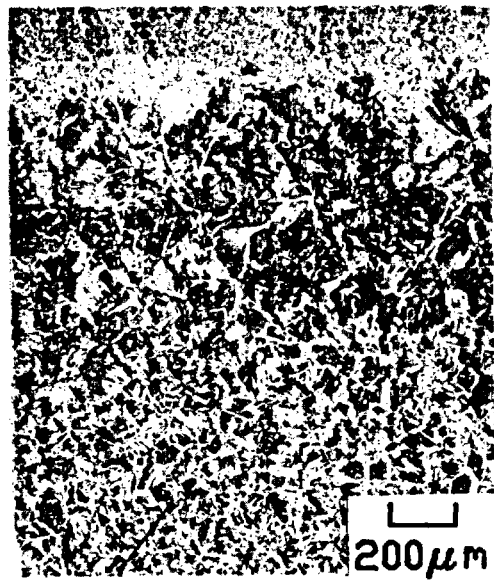
NRC-5



NRC-12



NRC-14

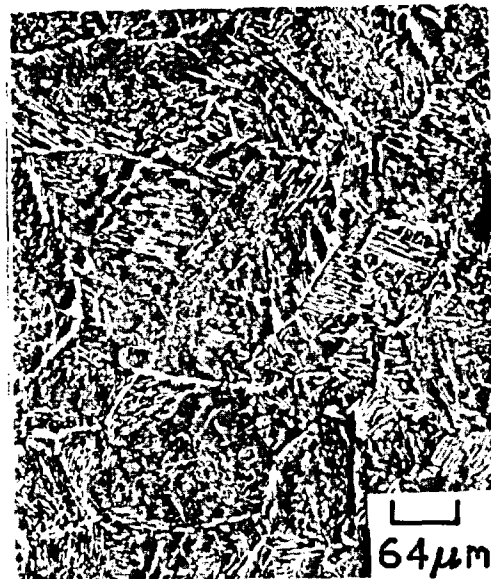


NRC-15

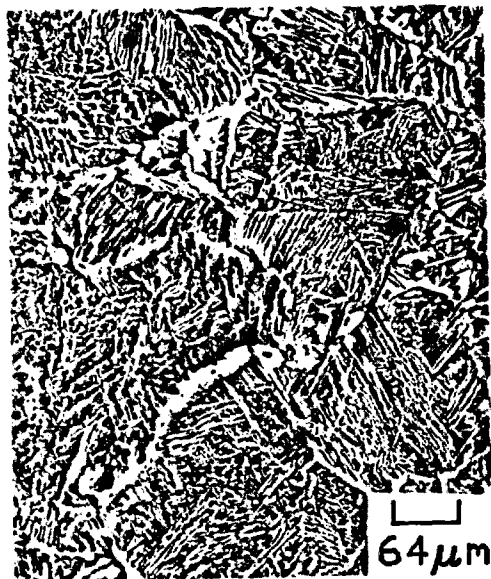
FIGURE 27. The fusion line (top) and grain growth region of the four welds studied, showing the microstructural differences directly next to the fusion line. Yorgason's etch, 50X



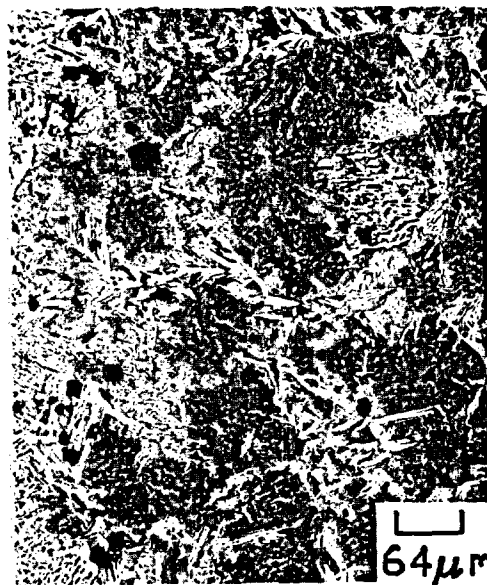
NRC-5



NRC-12



NRC-14



NRC-15

FIGURE 28. The grain growth region of each of the four steels showing microstructural differences related to cleanliness and alloy content. Yorgason's etch, 156X

allotriomorphic grain boundary ferrite, Widmanstatten ferrite, and some acicular ferrite in the central portion of the grain. The concentrations of oxygen and sulfur, and the volume fractions of sulfide and oxide inclusions were greater in Heat 14 than those in Heats 5 and 12. This caused an increase in the volume fraction of acicular ferrite.

Heat 15 had low oxygen and sulfur contents and a manganese content about the same as those of Heats 12, and 14. The high Mn/O ratio and low sulfur resulted in increased hardenability and a lower content of inclusions available for ferrite nucleation. This increased hardenability resulted in the formation of a bainitic microstructure with some widmanstatten ferrite along the grain boundaries. This structure would be expected to provide lower toughness than that provided by the structures which possess large fractions of acicular ferrite.

Figures 29, 30, and 31 show a comparison of the influence of composition and cleanliness on heat affected zone microstructures for three peak temperatures of about 940, 1250, and 1450°C. The structures were generated using the Gleeble weld simulator with programmed heating and cooling curves based on those observed for the actual welds. The structures in Figure 29 represent a peak temperature of about 940°C. The microstructures show some grain refinement, but all four alloy compositions have approximately the same microstructure.

Figure 30 compares the structures for a peak temperature of around 1250°C. Here the structure has transformed to austenite, and the effects of composition and cleanliness can be observed. Alloys 5 and 12, with low and medium Mn/O ratios show equiaxed ferrite/pearlite microstructures. Alloy 14 with a high sulfur level shows acicular and Widmanstatten ferrite; and Alloy 15, which has a high Mn/O ratio shows a bainitic structure.

Figure 31 compares the microstructures for a peak temperature between 1400°C and the liquidus, which would be observed in the grain growth region near the fusion line. Alloy 5 shows large prior austenite grains with allotriomorphic ferrite and Widmanstatten ferrite decorating the boundaries. There is upper bainite in the grain interiors with some acicular ferrite. Alloy 12 shows more ferrite laths throughout the structure than Alloy 5, and the upper bainite present is coarse. Alloy 14 shows smaller prior austenite grains than either Alloy 12 or Alloy 5 with a much coarser ferrite lath structure than either. Alloy 15 shows predominantly fine upper bainite with little or no allotriomorphic ferrite.

The microstructural differences illustrated by Figures 30 and 31 indicate that composition variations within the A-216 specification can have a significant influence on the heat affected zone microstructure where the peak temperature exceeds 1100°C and reaustenization occurs. Composition and cleanliness influence the structure of the reaustenitized region of the heat

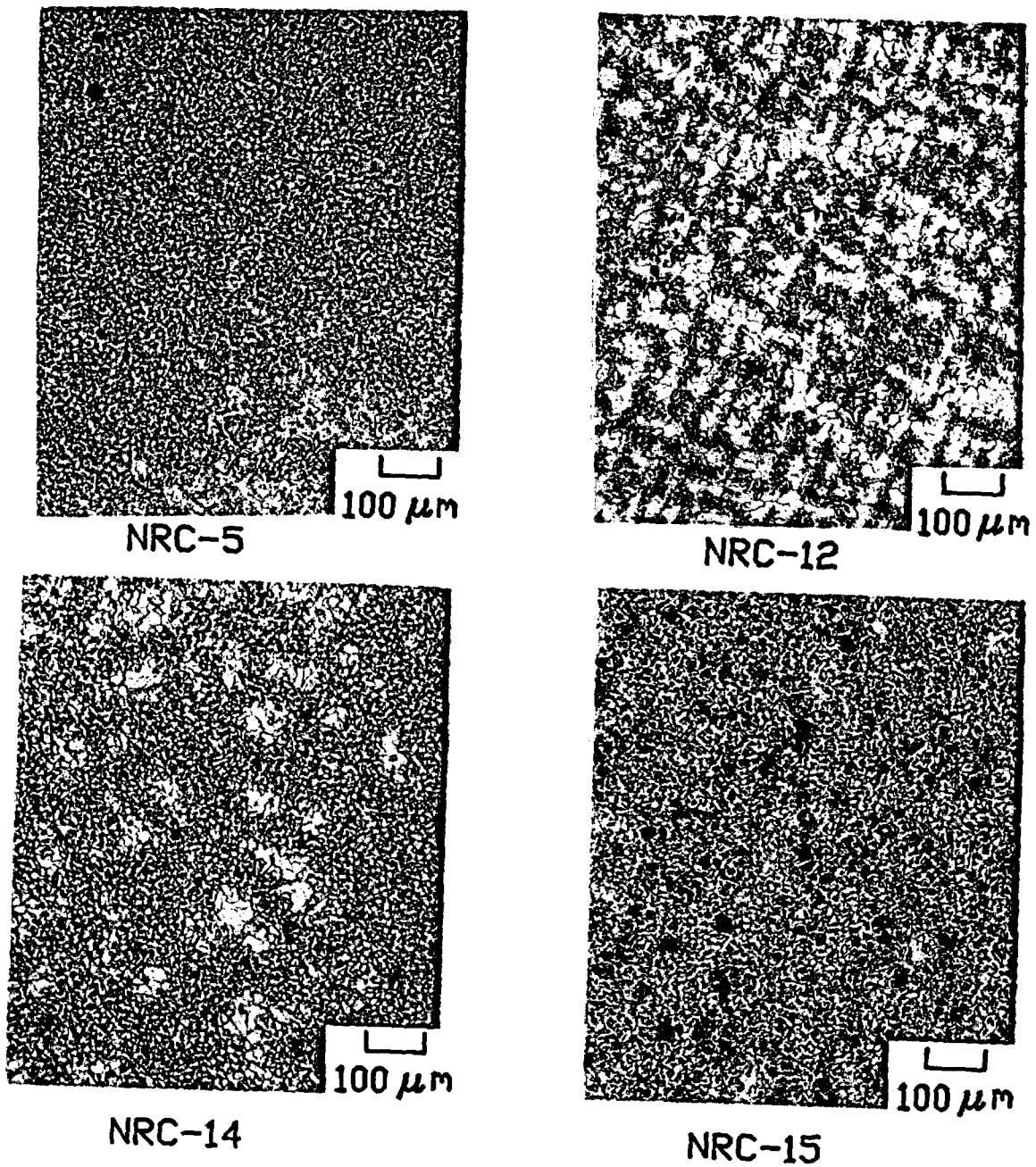
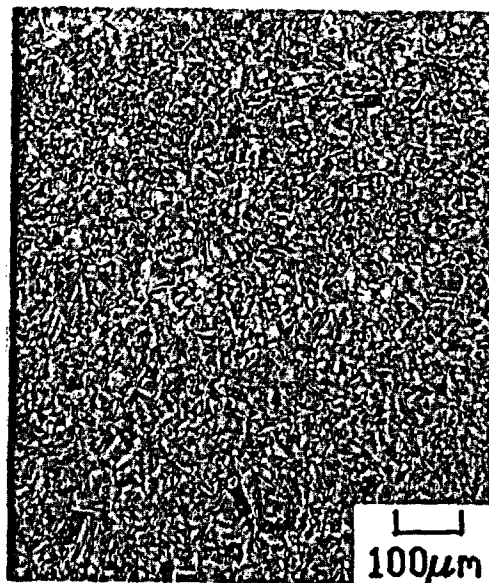
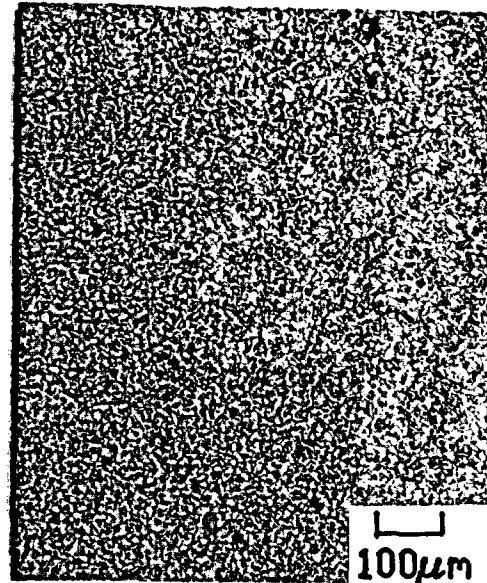


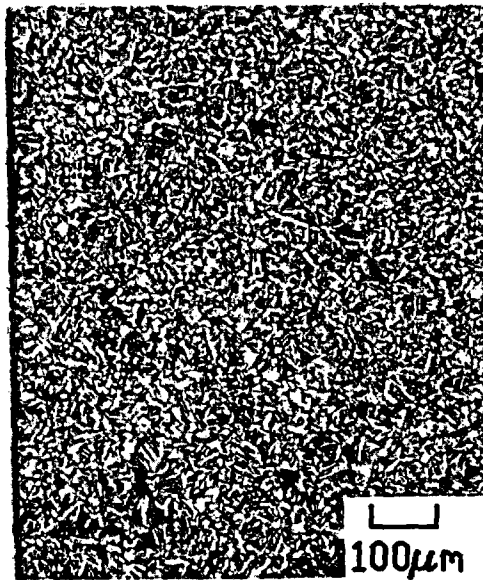
FIGURE 29. Microstructures of the experimental steels that were thermally cycled by a Gleeble 1500 weld simulator. The peak temperature seen is about 940°C. 2% nital 100X.



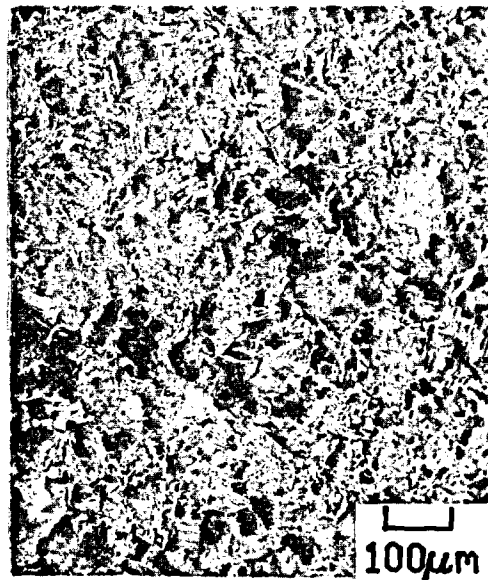
NRC-5



NRC-12



NRC-14

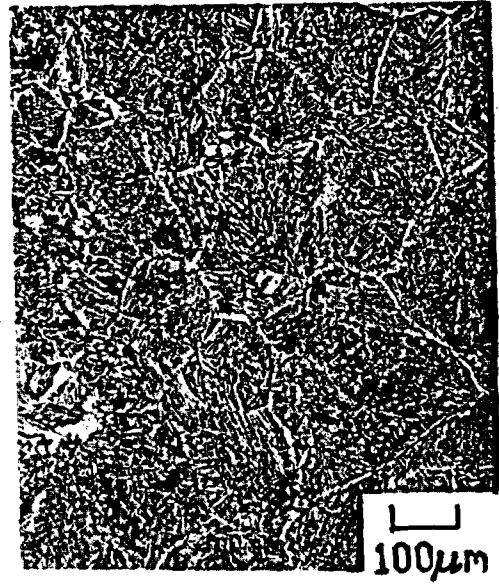


NRC-15

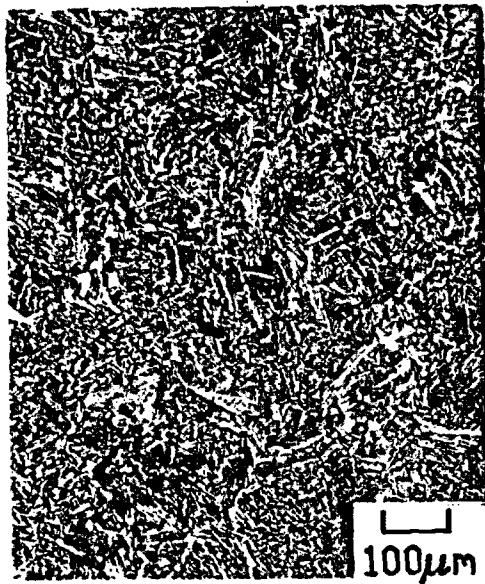
FIGURE 30. Microstructures of the experimental steels that were thermally cycled by a Gleeble 1500 weld simulator. The peak temperature seen is about 1250°C. 2% nital 100X.



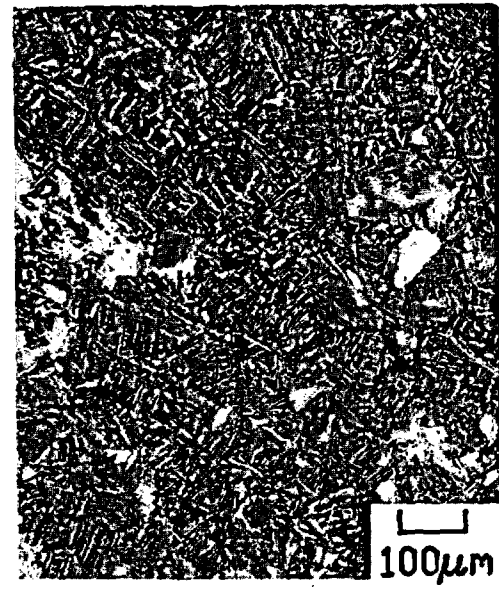
NRC-5



NRC-12



NRC-14



NRC-15

FIGURE 31. Microstructures of the experimental steels that were thermally cycled by a Gleeble 1500 weld simulator using a peak temperature of 1450°C. 2% nital, 100X.

affected zone by influencing hardenability and by providing heterogeneous nucleation sites for austenite decomposition reactions.

The heterogeneous nucleation sites provided by oxide and sulfide inclusions allow the formation of a higher ductility acicular ferrite structure at a smaller undercooling below the eutectoid temperature than that necessary for the formation of the lower ductility Widmanstätten ferrite or bainite microstructures. Hardenability is influenced by the presence of austenite stabilizing alloy elements such as manganese and by the action of second phase particles to limit austenite grain growth. A low Mn/O reduces hardenability by both mechanisms and avoids the transformation to lower temperature bainitic decomposition products.

The microstructural similarities observed for Alloys 5, 12, and 14 indicate that both sulfide and oxide inclusions provide nucleation sites for the formation of acicular ferrite. The small austenite grain size observed in Alloy 14 indicates that both oxide and sulfide inclusions play a significant role in limiting austenite grain growth near the fusion line. The bainitic structure observed near the fusion zone for Alloy 15 illustrates that a moderate manganese concentration coupled with low oxygen and sulfur contents (greater cleanliness) allow for grain growth in the re-austenitized region near the weld fusion line and the formation of undesirable low temperature austenite decomposition products such as bainite. Thus, cleanliness and alloy content have been shown to be significant variables influencing the structure and properties of welds in low carbon steel castings.

Gas Metal Arc welds were produced on cast Alloys 1 through 4 whose compositions were listed in Table 7. The characteristics of the four alloys are summarized in Table 10. Alloy 2 is representative of a typical production heat of steel castings conforming to the ASTM A216 - Grade WCA Specification. It has a high Mn/O ratio and few inclusions. Alloy 1 has a high silicon content, a low manganese content and a low Mn/O ratio. The manganese and silicon contents are such that the deoxidation product should be solid silica inclusions. Alloy 3 contains normal manganese and silicon levels and a high sulfur content to provide a large concentration of sulfide inclusions; and Alloy 4 has low manganese and silicon contents which give a low Mn/O ratio and globular oxides as a deoxidation product.

Light microscopy and scanning electron microscopy were used to investigate the inclusions in Alloys 1 through 4. The elemental contents of the inclusions and their size distributions were obtained using a JEOL scanning electron microscope with a Tracor Northern particle recognition program. The elemental analyses showed three basic inclusion types: aluminum rich, manganese and sulfur rich (manganese sulfides), and manganese and silicon rich (manganese silicates). Table 11 shows the area fractions for these three types of inclusions in Alloys 1 through 4.

**TABLE 10 - CHARACTERISTICS OF ALLOYS USED FOR GMA WELDING EXPERIMENTS**

Alloy	Silicon Content	Manganese Content	Sulfur Content	Mn/O Ratio	Inclusions
1	High	Low	Low	Low	Solid Silica
2	Normal	Normal	Low	Normal	Molten Manganese Silicates
3	High	High			Manganese Sulfides
4	Low	Low	Low	Low	Globular Oxides

**TABLE 11 - PERCENT OF AREA OF INCLUSIONS OBSERVED IN THE SCANNING ELECTRON MICROSCOPE AT 7500 X MAGNIFICATION.**

Alloy	Inclusion Types		
	Al-Rich	Mn-Sulfide	Mn-Silicate
1	3.6	3.2	5.8
2	4.2	3.3	2.1
3	2.8	8.4	3.4
4	3.3	2.4	4.9

The gas metal arc welds were metallographically evaluated to analyze the weld macrostructures, and the influence of base metal composition and cleanliness and the thermal cycle on the microstructure of the heat affected zone. Figure 32 is a schematic of the weld bead cross section which illustrates the locations of microstructural observations and measurements. All microstructural measurements were taken along a line which passes through the center of the bead and made a 45° angle with the top of the plate. This method was used because of the asymmetrical nature of the welds, and because this location provided the largest heat affected zone width.

The prior austenite grain size was measured at the fusion line of each single pass weld. This represents the maximum grain size in the heat affected zone after grain growth during the thermal cycle. Figure 33 shows a plot of the average grain diameter at the fusion line as a function of the heat input for single pass gas metal arc welds produced on Alloys 1 through 4.

The results in Figure 33 show that the grain size in the heat affected zone increases with increasing heat input, and that a slightly larger grain size is obtained for the standard ASTM A-216 alloy than for the various modifications with increased numbers of sulfide or oxide inclusions. This indicates that inclusions of both oxide and sulfide types are capable of limiting grain growth; however, the effect is a small one.

The base metal composition and the nature of the nonmetallic inclusions had a more significant influence on the volume fractions of various microstructural constituents in the heat affected zone. The volume fractions of the various phases were measured by point counting along a line at 45° to the plate surface. The results are plotted in Figures 34 through 37.

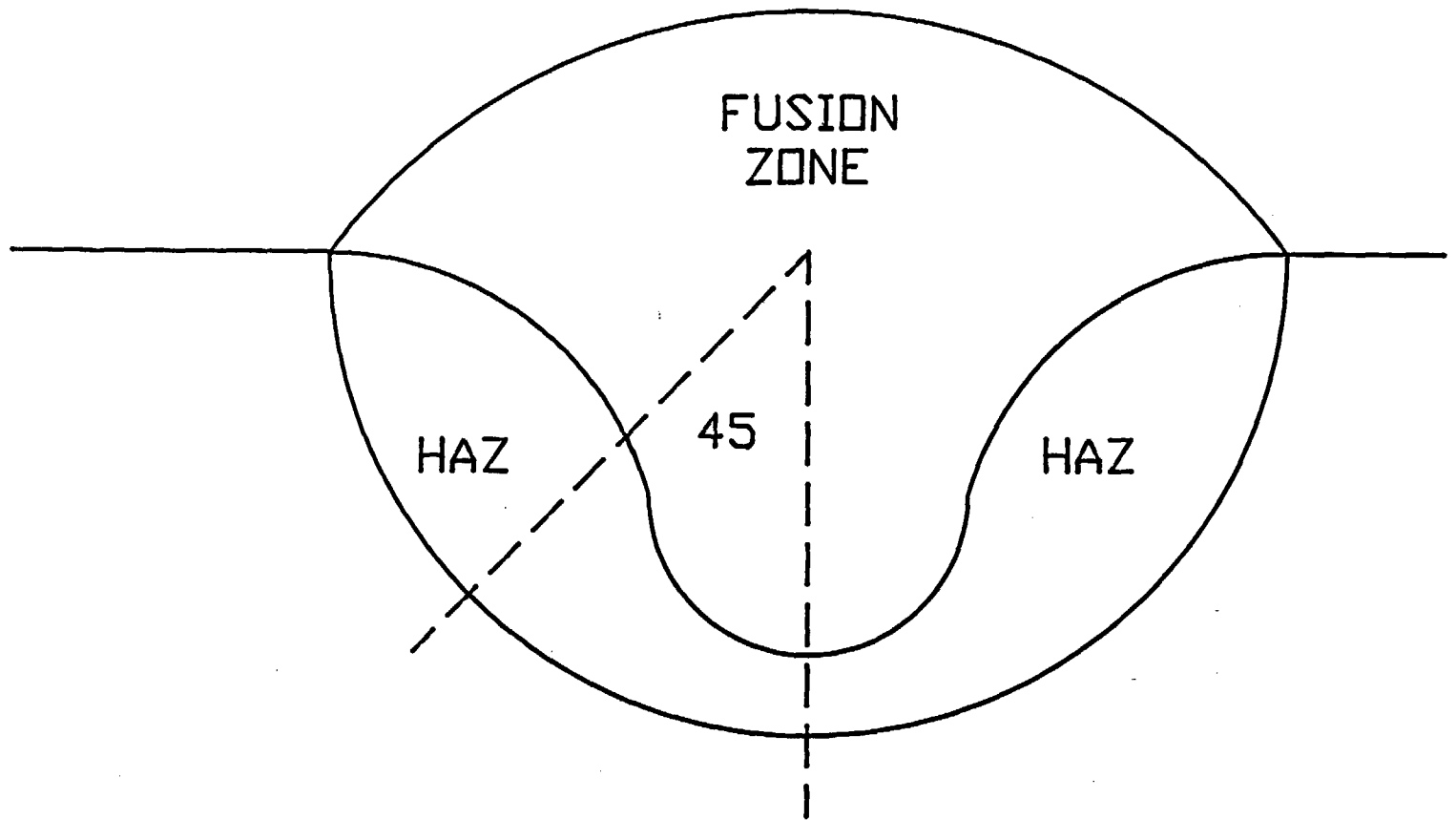


FIGURE 32. Location of microstructural observations and measurements.

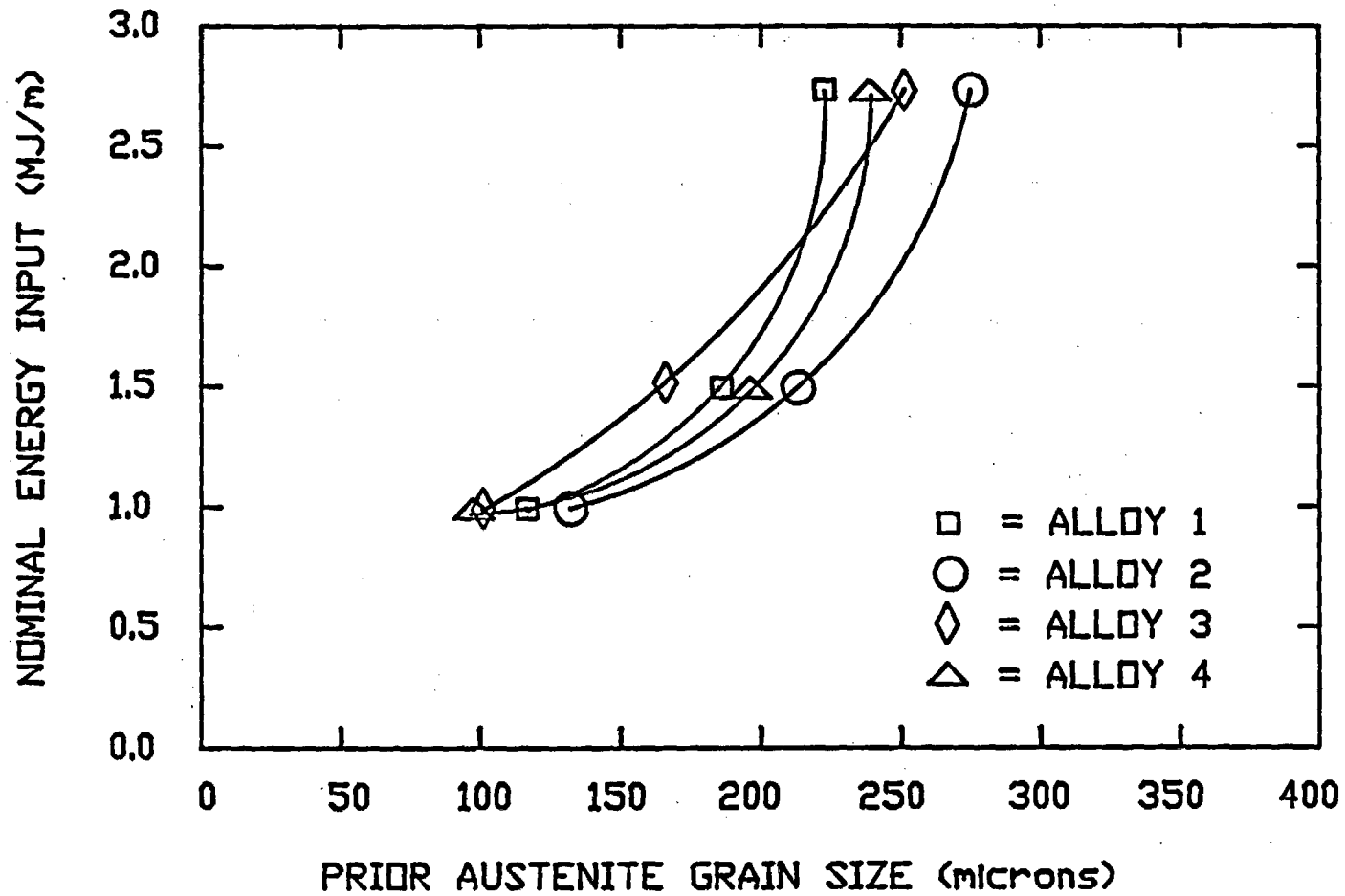


FIGURE 33. Prior austenite grain size at the fusion line as a function of heat input for the test alloys.

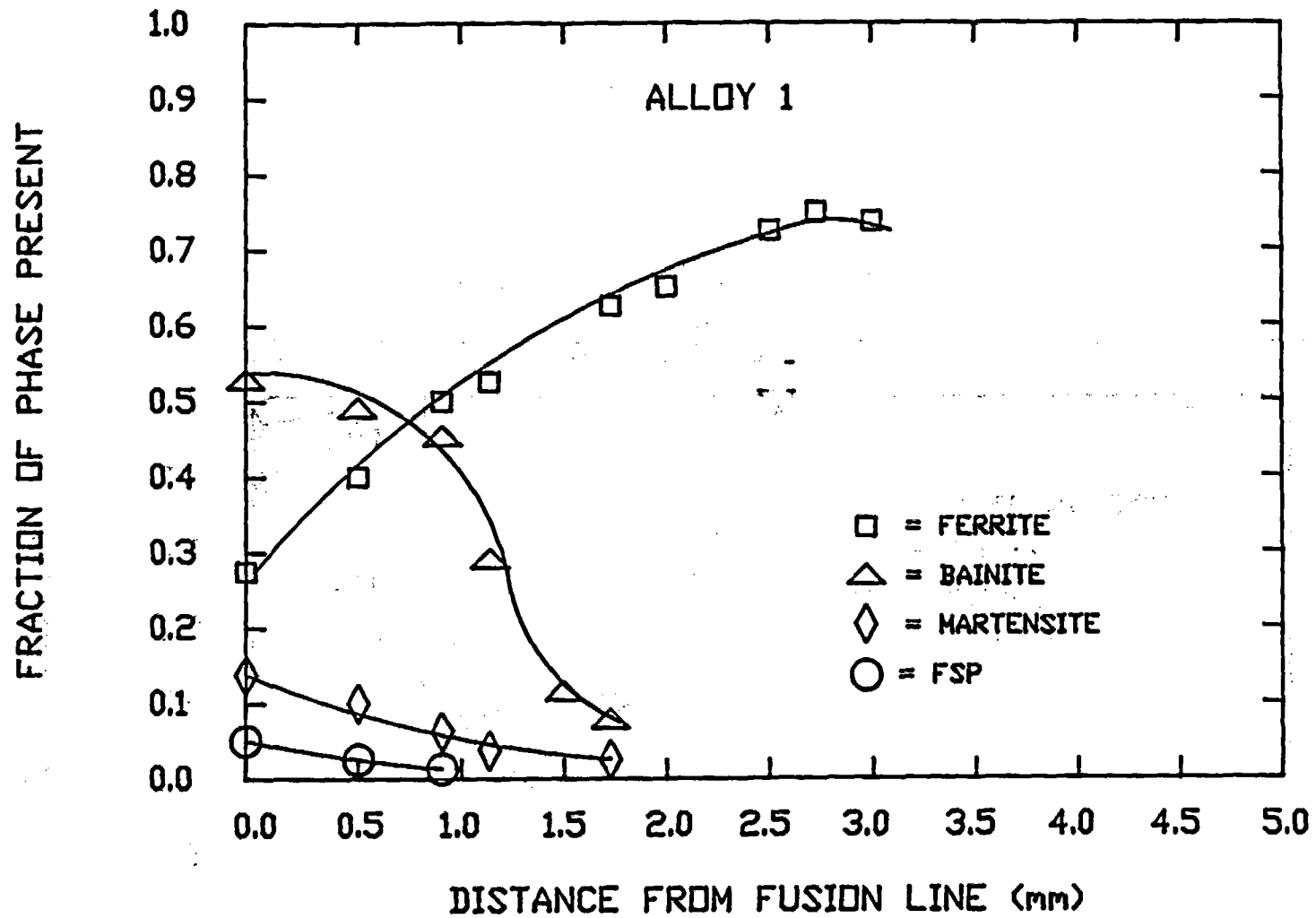


FIGURE 34. Fraction of phases present as a function of distance from the fusion line for alloy 1.

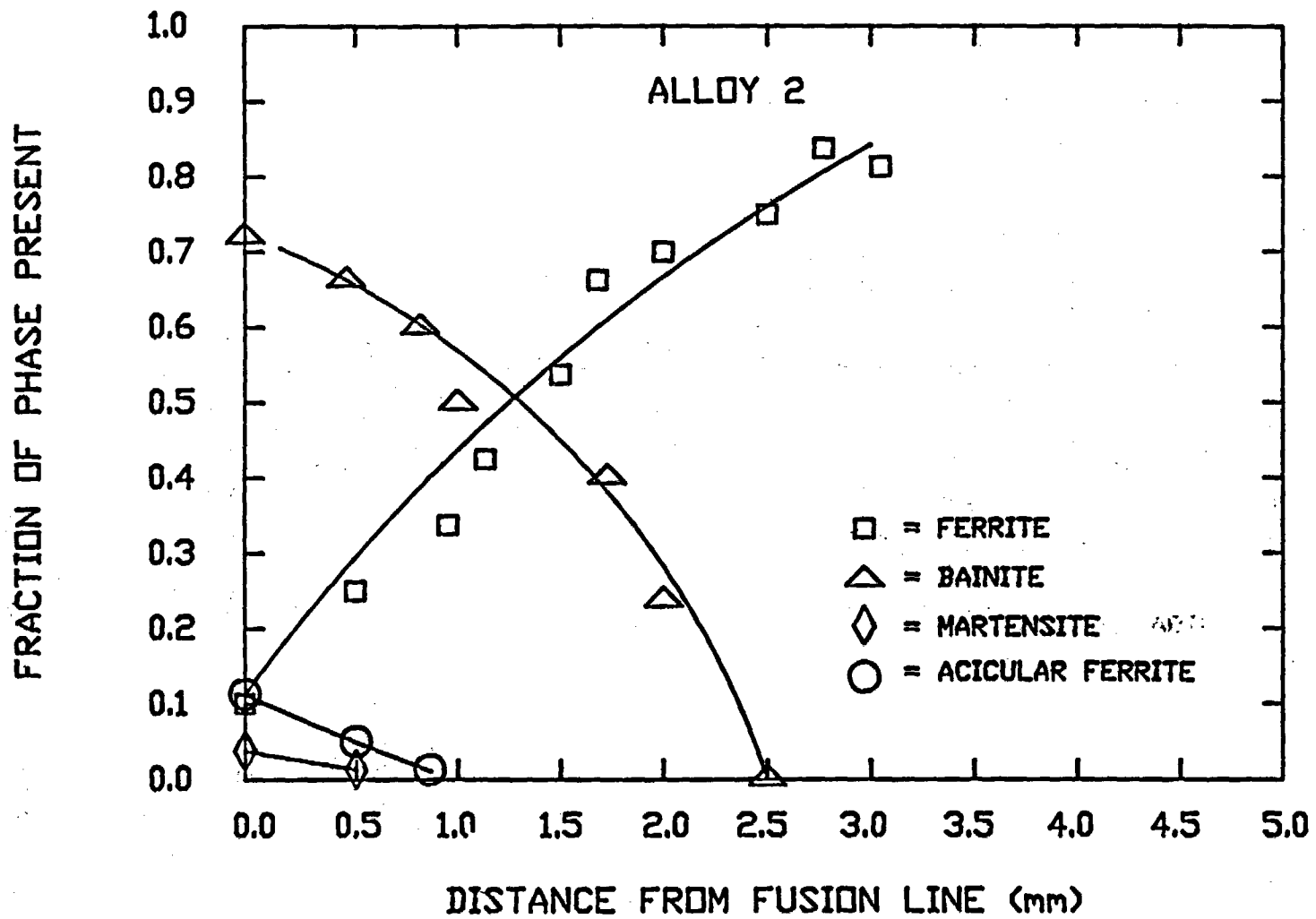


FIGURE 35. Fraction of phases present as a function of distance from the fusion line for alloy 2.

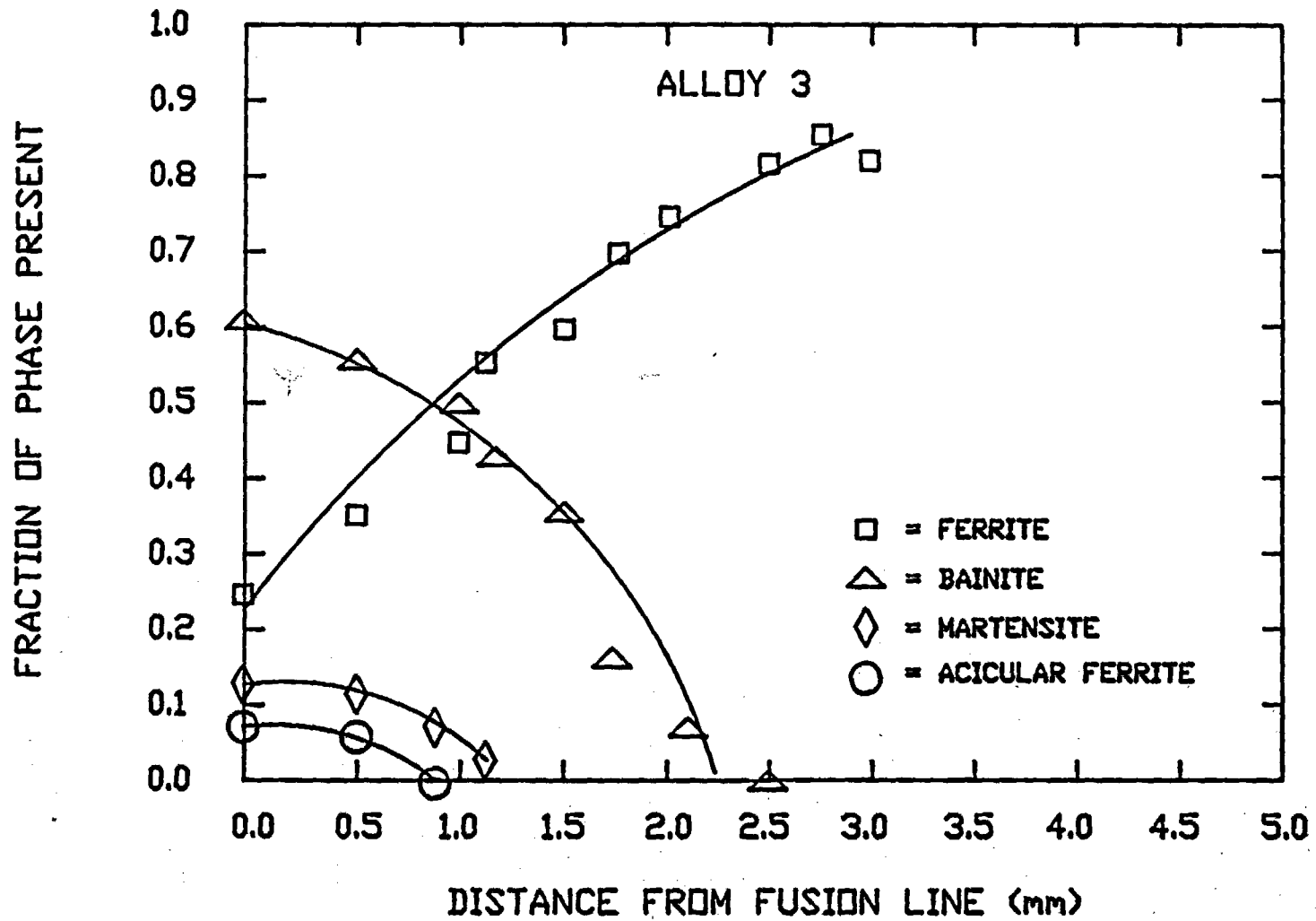


FIGURE 36. Fraction of phases present as a function of distance from the fusion line for alloy 3.

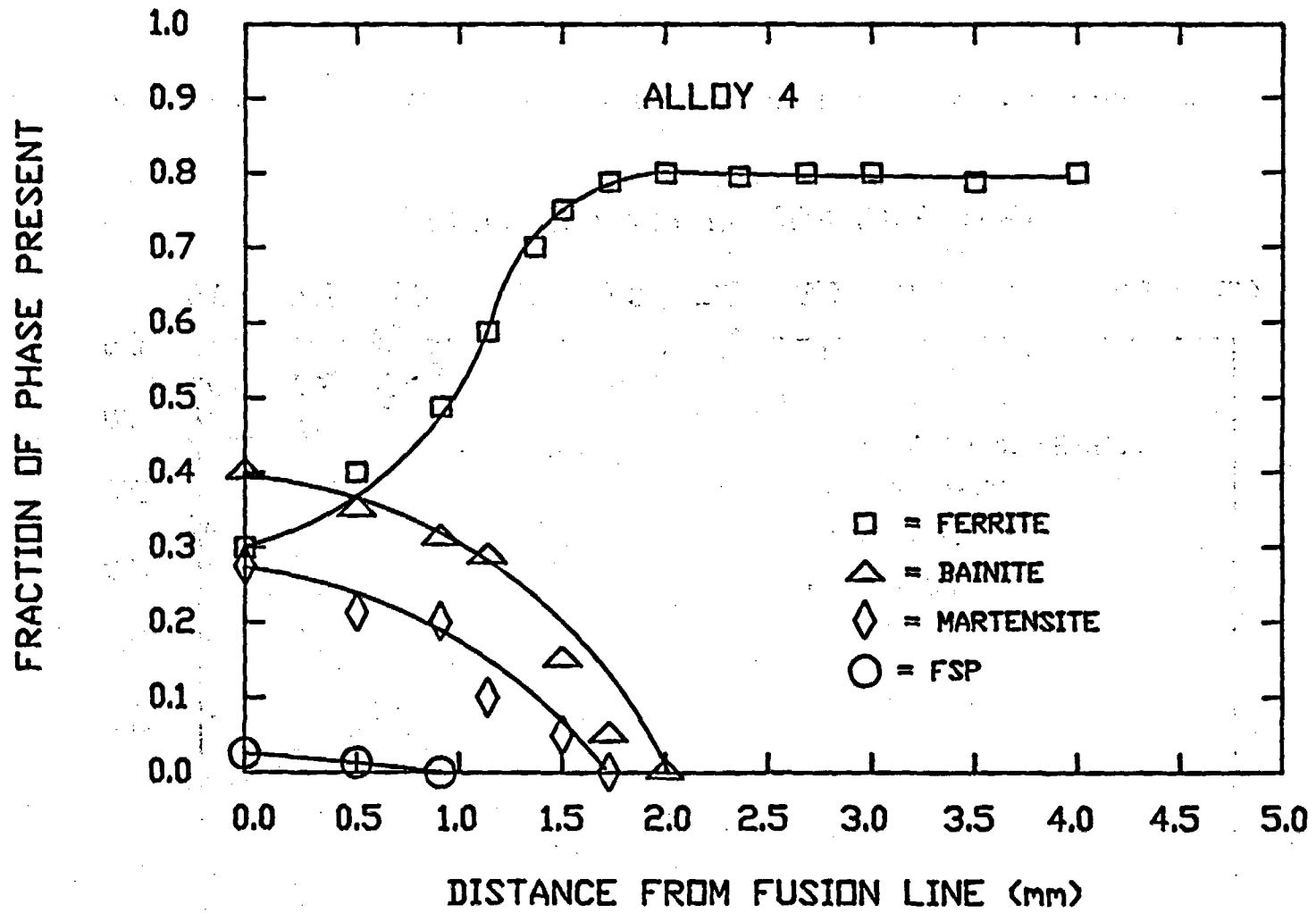


FIGURE 37. Fraction of phases present as a function of distance from the fusion line for alloy 4.

## 4.0 RESULTS AND CONCLUSIONS

### 4.1 Manufacturing Considerations

Heavy steel overpacks may be manufactured by wrought processing, centrifugal casting, or static casting. The scope of work for this project was specific to the study of cast steels. Further, preliminary consideration of wrought processing techniques such as forging, piercing, and ring rolling led to the conclusion that such techniques would probably not be cost competitive with casting. Manufacturing considerations were therefore limited to those approaches that use casting as the starting point for making the overpack.

Of the two casting techniques surveyed, static casting and centrifugal casting, centrifugal casting clearly appears to be the most economical and technically favorable method of making thick-walled steel cylinders of the dimensions applicable to overpacks. It is likely that the ends of the cast steel cylinder would be machined in preparation for attaching end caps by welding. The bottom end would be welded on in the shop where the cylindrical body was made using a high deposition rate welding process such as submerged arc welding. The top end cap would be welded in place at the repository after placement of the waste canister into the overpack. This top end cap weld would be the final seal of the waste package and would be done remotely because of the radiation hazard from the waste form. The welding process chosen for the final closure will likely be one that does not generate flux wastes that would add to the contaminated waste problem. Gas metal arc welding is the most obvious choice for the final weld.

### 4.2 Metallurgical Considerations

Behavior of cast and welded steel overpacks in the repository environment may be determined in part by the choice of material chemistry and manufacturing process conditions. Thermal histories developed during casting, welding, and heat treatment will be reflected as a microstructural signature in the fabricated overpack. Effects of alloy chemistry, solidification processing, and solid state phase transformations on final microstructure of the cast and welded overpack has been examined in detail in chapter 2 of this report.

The most likely failure mode for steel overpacks is generally felt to be corrosion failure, particularly accelerated forms of corrosion such as pitting or stress corrosion cracking. Failure from such localized or accelerated forms of corrosion is not predictable with certainty for any combination of material condition, repository environment, and exposure time. Prediction of corrosion behavior based upon manufacturing history is beyond the scope of this study.

Radioactive decay of waste may under some repository conditions give rise to temperatures in the overpack that are sufficiently

high to cause microstructural changes. Areas of high residual stress and non-equilibrium microstructures such as the final closure weld would be most susceptible to such changes.

#### 4.3 Defects from Manufacturing

Casting and welding processes used to manufacture overpacks may be the source of defects that can adversely affect the life of the overpack during repository storage. Defects such as porosity, cracks, undercutting, and lack of fusion may shorten life by providing a shorter and more active corrosion path through the defect area. Defects of a chemical nature such as micro and macro segregation also may lead to premature failure due to localized corrosion related to local variations in alloy chemistry.

#### 4.4 Quality Assurance

The manufacture of high level waste overpacks will be done under codes and standards that govern and guide the materials, processes, products, services, and systems used in making the final product. Such codes and standards do not presently exist for direct application to high level waste containers. The ASME Boiler and Pressure Code has been cited as that existing document that is most nearly applicable. It is likely that some extension of this code, supplemented by internal government standards, will eventually be adopted for application to high level waste containers.

Various existing codes require the qualification and certification of welding procedures and operators who perform the welding. Likewise, weldments are subject to inspection by qualified personnel using specified procedures. Existing codes do not attempt to regulate quality of castings by qualification of manufacturing personnel or by control of manufacturing methods. Cast products are typically covered by product specifications that seek to define soundness, chemical and metallurgical characteristics, mechanical properties, and dimensional characteristics. It is likely that this situation, procedural control for welding and product specification for casting, will carry over into codes that govern overpack manufacture.

Physical inspection of the product is the generally accepted method of determining the compliance of a manufactured item with codes, standards, or specifications. Body and lid components for cast steel overpacks will be inspected at the place of manufacture using standard, well established methods of nondestructive evaluation such as radiography, ultrasonics, liquid penetrant, and visual inspection. The final closure weld made after waste loading will present a challenge to adequate inspection because the operations must be done remotely. Methods such as ultrasonic inspection, visual inspection through remote

video or fiber optics, and continuous process monitoring using acoustic emission are applicable.

#### 4.5 Experimental Research

The charter of this investigation, to determine the effect of manufacturing on waste overpack performance, encompasses a virtually limitless range of process and material variables. Useful experimental research was done within the project scope by clearly focusing the work toward a few attainable objectives. These objectives are summarized as follows:

1. Characterize microstructures that will result from material and process combinations that DOE will likely use.
2. Explore process limits applicable to practical fabrication of cast steel overpacks.
3. Investigate changes in microstructure that may arise from repository thermal conditions.

Representative microstructures were generated using three alloy composition ranges within the ASTM A-216, Grade WCA specification for carbon steel castings suitable for welding. Chemical composition of the three alloy ranges were chosen to vary the hardenability, oxygen content, and the cleanliness in terms of nonmetallic inclusions. Solidification rates were controlled under laboratory conditions to simulate microstructures attainable both for centrifugal and static casting. Weldments were made using the submerged arc and gas metal arc processes, the two processes felt to be the most likely candidates for end cap welding.

Examination of various cast and welded specimens showed a wide variation of possible microstructures due to variations in alloy chemistry and thermal history. The manganese to oxygen ratio and sulfur content dramatically affect the austenite transformation morphology by influencing the level of nonmetallic inclusions that serve as nucleation sites for formation of acicular ferrite. Ferrite morphology is of primary interest in determining mechanical properties of mild steel weldments. The effect of ferrite morphology on fracture toughness has been well documented. It is likely that the microstructural variations documented by this project will be important in determining the long term behavior of these steels under repository conditions. However, correlation of long term corrosion behavior of mild steel castings and weldments with relatively subtle variations in microstructure remains beyond present understanding.

5. REFERENCES

1. Westinghouse Advanced Energy Systems Division, "Conceptual Designs of Waste Packages for a Nuclear Repository in Basalt," October 1982, Rockwell Hanford Operations Document No. SD-BWI-CDR-004, Rev 0-0.
2. Battelle Project Management Division, Request for Proposal (RFP) No. E512-08400R Design, "Development and Testing of Repository Waste Packages and Packaging, Handling and Emplacement Equipment for a Salt Repository," December 30, 1983.
3. Russell, E.W., et al., "Containment Barrier Metals for High-Level Waste Packages in a Tuff Repository," October 12, 1983, Lawrence Livermore National Laboratory Report UCRL-53449.
4. American Society for Testing Materials, 1977, A-216, Grade WCA.
5. United States Steel, THE MAKING, SHAPING, AND TREATING OF STEEL, 1984.
6. Wladawer, R., DIRECTIONAL SOLIDIFICATION OF STEEL CASTINGS, Pergamon Press, New York.
7. Heine, Loper, and Rosenthal, PRINCIPLES OF METAL CASTING, Second Edition, McGraw Hill, New York, 1967.
8. Flinn, R.A., FUNDAMENTALS OF METAL CASTING, Addison Wesley, 1963.
9. Vennard, J.K., and Street, R.L., ELEMENTARY FLUID MECHANICS, John Wiley & Sons, Inc., 1961.
10. Beeley, P.R., FOUNDRY TECHNOLOGY, Butterworths, London, 1972.
11. Taylor, H.F., Flemings, M.C., and Wulff J., FOUNDRY ENGINEERING, John Wiley and Sons Inc., New York, 1959.
12. Habraken, L. and Brouwer J.L., DE FERRI METALLOGRAPHICA, VOLUME I, W. B. Saunders Co., 1966.
13. ASM Metals Handbook, Vol. 8, 8th Edition, American Society for Metals, Metals Park, Ohio, p. 277.
14. Marsh, C.P., Bland, I.W., Desport, J.A., Westcott, C. and Taylor, K.T., "Corrosion Assessment of Metal Overpacks for Radioactive Waste Disposal", European Appl. Res. Rept. Nucl. Sci. Technol. 5, (2), pp. 223-252 (1983).

15. Mendel, J.E., "The Scientific Basis for Long-Term Prediction of Waste-Form Performance Under Repository Conditions," Mat. Res. Soc Symposium Proceedings 15, 1-7 (1983).
16. Simonson, S.A., and Kuhn, W.L., "Predicting Amounts of Radiolitically Produced Species in Brine Solutions," Mat. Res. Soc. Proc. 26, 781-787 (1984).
17. Pederson, L.R., Clark, D.E., Hodges, F.N., McVay G.L. and Rai, D., "The Expected Environment for Waste Packages in a Salt Repository", Mat. Res. Soc. Proc. 26, 417-427 (1984)
18. Ahn, J.M., Lee, B.S., Woodward, J., Sabatini, R.L. and Soo, P., "Corrosion of TiCode-12 in a Simulated Waste Isolation Pilot Project (WIPP) Brine," Mat. Res. Soc. Symp. Proc. 15, 761-767, (1983).
19. Syrett, B.C., MacDonald D.D., and Shik, H., "Pitting Resistance Engineering Materials in Geothermal Brines-I. Low Salinity Brine," Corrosion, 36(3), 130-139 (1980).
20. Romanoff, A., "Underground Corrosion," NBS Circular 579 (1957).
21. Harrar, J.E., McCright and Goldberg, A., "Corrosion Characteristics of Materials in Hypersaline Geothermal Brine," SAMPE Quarterly, October, 1-15 (1978).
22. Carter, J.P. and McCowley, F.X., "Corrosion tests in Brine and Steam from the Salton Sea, KGRA," J. Materials for Energy Systems, 3(4), 30-38 (1982).
23. Elliott, J. F., and Gleiser, M., THERMOCHEMISTRY FOR STEELMAKING, Vol. I, Addison-Wesley, 1960.
24. Elliott, J. F., Gleiser, M., and Ramakrishna, V., THERMOCHEMISTRY FOR STEELMAKING, Vol. II, Addison-Wesley, 1963.
25. Elliott, J. F., and Meadowcroft, T. R., STEELMAKING: THE CHIPMAN CONFERENCE, M.I.T. Press, 1962.
26. BASIC OPEN HEARTH STEELMAKING, A.I.M.E., 1951.
27. ELECTRIC FURNACE STEELMAKING - VOL. I and II, A.I.M.E., Interscience Publishers, 1962.
28. ELECTRIC FURNACE STEELMAKING - Iron and Steel Society of the A.I.M.E., 1985.
29. BOF STEELMAKING, Vol.I and II, Iron and Steel Society of the A.I.M.E., 1974.
30. Fruehan, R. J., LADLE METALLURGY PRINCIPLES AND PRACTICES, Iron and Steel Society of the A.I.M.E., 1985.

31. THE ELECTRIC ARC FURNACE, International Iron and Steel Institute, Brussels, 1981.
32. Sharp, J. D., ELECTRIC STEELMAKING, London Iliffe Books, Ltd., 1966.
33. Hubbard, M. W., STEELMAKING FOR STEEL FOUNDERS, MONOGRAPH 1, INDUCTION FURNACE PRACTICE, Steel Casting Research and Trade Association, Sheffield, 1972.
34. Holt, J., Hubbard, M. W., and Jackson, W. J., STEELMAKING FOR STEEL FOUNDERS, MONOGRAPH 2, ELECTRIC ARC FURNACE PRACTICE, Steel Casting Research and Trade Association, Sheffield, 1973.
35. Hubbard, M. W., STEELMAKING FOR STEEL FOUNDERS, MONOGRAPH 3, HIGH ALLOY STEELMAKING, Steel Castings Research and Trade Association, Sheffield, 1972.
36. Jackson, W. J., STEELMAKING FOR STEEL FOUNDERS, MONOGRAPH 4, GASSES IN STEEL, Steel Castings Research and Trade Association, Sheffield, 1973.
37. Kirkaldy, J. S., LADLE TREATMENT OF CARBON STEEL, McMaster Symposium on Iron and Steelmaking No. 7, 1979.
38. Kiessling, R., NON-METALLIC INCLUSIONS IN STEEL, Parts I-IV, The Metals Society, London, 1978.
39. Wilson, W. G. and McLean A., DESULFURIZATION OF IRON AND STEEL AND SULFIDE SHAPE CONTROL, Iron and Steel Society of the A.I.M.E., 1980.
40. Coudurier, L., Hopkins, D. W., and Wilkomirski, I., FUNDAMENTALS OF METALLURGICAL PROCESSES, Pergamon, Oxford, 1978.
41. Richardson, F. D., PHYSICAL CHEMISTRY OF MELTS IN METALLURGY, VOLUME 1, Academic Press, London, 1974.
42. Richardson, F. D., PHYSICAL CHEMISTRY OF MELTS IN METALLURGY, VOLUME 2, Academic Press, London, 1974.
43. Rosenquist, T., PRINCIPLES OF EXTRACTIVE METALLURGY, McGraw-Hill, 1974.
44. Carslaw, H. S. and Jaeger, J. C., HEAT CONDUCTION IN SOLIDS, Oxford, 1959.
45. Flemings, M. C., SOLIDIFICATION PROCESSING, McGraw-Hill, New York, 1974.
46. Kurz, W. and Fisher, D.J., FUNDAMENTALS OF SOLIDIFICATION, Trans Tech Publications, Switzerland, 1986.

47. Ruddle, R. W., THE SOLIDIFICATION OF CASTINGS, Institute of Metals Monograph and Report Series, No. 7, Institute of Metals, London, 1957.
48. STEEL CASTINGS HANDBOOK, Fifth Edition, Steel Founders Society of America, 1980.
49. Elliott, EUTECTIC SOLIDIFICATION PROCESSING - CRYSTALLINE AND GLASSY ALLOYS, Butterworths Monographs in Materials, London, 1983.
50. Davies, G. J., SOLIDIFICATION AND CASTING, Applied Science Publishers, Ltd., London, 1973.
51. LIQUID METALS AND SOLIDIFICATION, American Society for Metals, 1958.
52. SOLIDIFICATION, American Society for Metals, 1971.
53. Burke, J. J., Flemings, M. C., and Gorum, A. E., Editors, SOLIDIFICATION TECHNOLOGY, Brook Hill Publishing Co., 1971.
54. Chalmers, B., PRINCIPLES OF SOLIDIFICATION, John Wiley, New York, 1964.
55. Brody, H. D., and Apelian, D., Editors, MODELING OF CASTING AND WELDING PROCESSES, Metallurgical Society of the A.I.M.E., 1981.
56. Dantzig, J. A., and Berry, J. T., MODELING OF CASTING AND WELDING PROCESSES II, Metallurgical Society of the A.I.M.E., 1984.
57. Chvorinov, N., Giesserei, Vol. 27, p. 177, 1940.
58. Schwartz, J. W., Z. Angew. Math. Mech., Vol. 13, p. 202, 1933.
59. A GUIDE TO THE SOLIDIFICATION OF STEELS, Jernkontoret, Stockholm, 1977.
60. Pehlke, R. D., COMPUTER SIMULATION OF SOLIDIFICATION, American Foundrymen's Society, 1976.
61. Flemings, M.C., and Nereo, G.E., "Macroseggregation, Part I", Trans. Met Soc. AIME, 239, p. 1449, 1967.
62. Flemings, M.C., Mehrabian, R., and Nereo, G.E., "Macroseggregation, Part II," Trans, Met. Soc. AIME, 242, p. 41, 1968.
63. Flemings, M.C., and Nereo, G.E., "Macroseggregation, Part III", Trans. Met. Society. AIME, 242, p. 50, 1968.

64. Mehrabian, R., "Segregation Control in Ingot Solidification," in SOLIDIFICATION TECHNOLOGY, J.J. Burke, et al. editors, Brook Hill Publishing Co., 1971.
65. Lancaster, J.F., METALLURGY OF WELDING, George Allen and Unwin, Ltd., London, 1980.
66. THE PHYSICS OF WELDING, J.F. Lancaster Editor, Pergamon Press, 1984.
67. Easterling, K.E., Introduction to the Physical Metallurgy of Welding, Butterworths, London, 1983.
68. WELDING HANDBOOK, VOL. 1, Seventh Edition, American Welding Society, 1981.
69. WELDING HANDBOOK, VOL. 2, Seventh Edition, American Welding Society, 1981.
70. Vaughan, T.R. and Frost R.H., "Process Control in the Gas Metal Arc Welding of Iron-Chromium-Aluminum Alloys," Proceedings of the International Symposium on Advances in Welding Research, Gatlinburg, Tenn., 1986.
71. Welding Handbook, Sixth Edition, Section 5, Applications of Welding, American Welding Society, 1973.
72. Metals Handbook, Ninth Edition, VOLUME 6, WELDING, BRAZING, AND SOLDERING, American Society for Metals, 1983.
73. Jackson, C.E., "Fluxes and Slags in Welding," WRC Bulletin 190 (1973).
74. Russanevitz, N.F., Avtog, Delog. 9, 27 (1938).
75. Davidenko, I.D. Avotog. Delog. 9, 6, (1938).
76. Carmona, E., M.S. Thesis T-2123, Colorado School of Mines, Golden, Colorado, 1978.
77. Patchett, B.M., Dandy, E.A., Schwemmer, D.D., Olson, D.L., and Williamson, D.L., Welding Journal Research Supplement, 59, p. 31-s, (1980).
78. Tuliani, S.S., Boniszewski, T., and Eaton N.F., Weld Metal Fabrication, Vol. 37, 327, (1969).
79. Sekiguchi, H., "Fundamental Research on the Welding Heat Affected Zone of Steel," Nikkan Kogyo Shimbun, Tokyo (1976).
80. American Welding Society, "Terms and Definitions," AWS-A2.0-69 (1969).

81. BSI, "Welding Terms and Symbols - Part I", Welding, Brazing and Thermal Carrying Glossary, B.S. 499, Part I, London (1965).
82. Coe, F.R., Welding Institute Research Report No. 75/1978/M (1978).
83. Davis, M.L.E. and Bailey, N., in International Conference on Trends in Steel and Consumables for Welding," Paper 19, Welding Institute, London, (1978).
84. Noor, M.A.B., North, T.H., and Bell, H.B., Welding and Metal Fabrication, Vol. 46, 1978, p. 194.
85. Mori, K. "A New Scale of Basicity in Oxide Slags," Bulletin of the Faculty of Engineering, Ibaraki University, Vol. 2, p. 45 (1960).
86. North, T.H., Bell, H.B., Nowicki, A., and Craig, I., Welding Journal, Vol. 57, 63s (1978).
87. Palm, J.H., Welding Journal, Vol. 51, 1972, pp. 258s.
88. Kubli, R.A., and Sharav, W.B., Welding Journal, Vol. 40, 1961, p. 497s.
89. Lewis, W.J., Faulkner, G.E., and Rieppel, P.J., Welding Journal, Vol. 40, 1961, p. 337s.
90. Garland, J.G., and Kirkwood, P.R., Welding and Metal Fabrication, Vol. 44, 1976, p. 217.
91. Eager, T.W., Welding Journal, Vol. 57, 1978, p. 76s.
92. Wood, D., "The Case for Determining the Silica Activity of Submerged Arc Fluxes," Presentation to the Welding Institute (1975).
93. Wegrzyn, J., "Properties of Mild Steel Submerged Arc Welds Made with Neutral and Basic Fluxes," Institute of Welding, Gliwic, Poland, IWW Doc. II-A-384-75 (1974).
94. V.R. Dillenbeck, Li Castagno, "The Effects of Various Shielding Gases and Associated Mixtures in GMA Welding of Mild Steel," Welding Journal, Sept. 1987, pp 45 -49
95. O. Grong, N. Christensen, "Factors Controlling Mig Weld Metal Chemistry," Scandinavian Journal of Metallurgy, V12, (4), 1983, pp 155 - 165
96. Nippes, E.F., 1959, "The Weld Heat-Affected Zone," Welding Journal, vol. 38, No. 1, pp. 1s-18s.
97. Deiter, G.E., Jr., 1961, Mechanical Metallurgy, McGraw-Hill, New York, p. 385.

98. Kaae, J.L. and Bailey, N., 1969, "The HAZ Fracture Toughness of Controlled-Rolled Nb Treated, Low C, Mn Steels," Metal Construction, Vol. 1, No. 8, pp. 371-377.
99. Hrivnak, Ivan, 1969, "Materials for Electroslag Welding," Metal Construction, Vol. 1., No. 2, pp. 74-77.
100. Malinovska, E. and Hrivnak, I., 1967, "Electroslag Welding of 100 mm Thick Boiler Steels Eliminating the Need for Normalizing," British Welding Journal, Vol. 14, No. 10, pp. 527-532.
101. Bentley, K.P., "Toughness in Electroslag Welds," British Welding Journal, Vol. 15, No. 8, 1968, p. 408.
102. Braun, M.P., Eregın, L.P., and Malai, A.E., "Preventing the HAZ in High Tensile Steel from Becoming Brittle," Automatic Welding, Vol. 21, No. 5, 1968, p.6.
103. Braun, M.P. et al., 1969, "Reasons Why Complex Alloyed Chromium-Manganese Steel Becomes Brittle After Electroslag Welding," Automatic Welding, Vol. 22, No. 10, pp. 6-11.
104. Makara, A.M., Yegrova, S.V., and Novikov, I.V., "The Heat Treatment of Electroslag Welded Joints Between Ac1 and Ac2 Points, Automatic Welding, Vol. 22, No. 12, pp. 1-6.
105. Jeke, J., and Malanowski, E., "Suitability of Steels for Electroslag Welding," Automatic Welding, Vol. 14, No. 7, pp. 31-39.
106. Hannerz, N.E., Valland, G., and Easterling, K., IIW-II612-72 (1972).
107. Jesseman, R.J., "Columbium Pick Up in High Dilution, Submerged Arc Welding Deposits," Proceedings of MICROALLOYING 75, Union Carbide, P. 578, (1977).
108. Gray, J.M., Stuart, H., and Heisterkamp, F., "The Control of Toughness in Submerged Arc Weldments in Niobium Containing Steels, International Conference on Trends in Steel and Consumables for Welding, Paper 31, Welding Institute, London, (1978).
109. Garland, J.G. and Kirkwood, P.R., "Towards Improved Submerged Arc Weld Metal," Metal Construction, Vol. 7, 1975, p. 275.
110. Garland, J.G. and Kirkwood, P.R., Metal Construction, Vol, 7, 1975, p. 320.
111. Garland, J.G. and Kirkwood, P.R., Welding and Metal Fabrication, Vol. 44, 1976, p. 217.
112. Lewis, W.J., Faulkner, G.E. and Rieppel, P.J., Welding Journal, Vol. 39, 1960, p. 266s.

113. Lewis, W.J., Faulkner, G.E. and Rieppel, P.J., *Welding Journal*, Vol. 40, 1961, p. 337s.
114. Indacochea, J.E., and Olson D.L., "Relationship of Weld Metal Microstructure and Penetration to Weld Metal Oxygen Content'" ASM Conf. on Welding Consumables and Process Developments, Peoria, Illinois, Sept., 1981.
115. Indacochea, J.E., Ph.D. Thesis, Colorado School of Mines, Golden, Colorado, 1981.
116. Abson, D.J. and Dolby, R.E., *Welding Institute Research Bulletin* Vol. 19, (1978).
117. Smith, C.S., *Trans. ASM*, Vol. 45, p. 533 (1953).
118. Shewmon, P., *TRANSFORMATIONS IN METALS*, McGraw Hill, 1969.
119. Abson, D.J., *Welding Institute Research Report* No. 69/1978/M (1978).
120. Abson, D.J., and Dolby, R.E., in the International Conference on "Trends in Steel consumables for Welding," Paper 25, *Welding Institute*, London (1978).
121. Coldren, A.P., Smith, Y.E., and Cryderman, R.L., in Symposium "Toward Improved Ductility and Toughness," AMAX Foundation, p. 119, Kyoto (1971).
122. Widgery, D.J., *Welding Journal*, Vol. 55, 1976, p. 57s.
123. Cochrane, R.C., and Kirkwood, P.R., in International Conference "Trends in Steel and Consumables for Welding," Paper 35, *Welding Institute*, London, (1978).
124. Widgery, D.J., in International Conference, "Trends in Steel and Consumables for Welding," Paper 26, *Welding Institute*, London (1978).
125. Widgery, D.J., *Welding Journal*, Vol. 55, No. 3, p. 75s, (1976).
126. Abson, D.J. and Dolby, R.E., "A Scheme for the Quantitative Description of Ferritic Weld Microstructures," IIW Doc. IKJ-29-80, American Council, AWS, (1980).
127. Cochrane, R.C., "Weld Metal Microstructures - A State-of-the-Art Review," IIW Doc. IXJ-62-82, American Council, AWS, (1982).
128. Pargeter, R.J., "Quantification of Ferritic Weld Metal Microstructures - Results of an International Exercise," IIW Doc. IXJ-37-80, American Council, AWS, (1980).

129. Pargeter, R.J., "Quantification of Weld Metal Microstructures," IIW Doc. IXJ-78-83, American Council, AWS, (1983).
130. Pargeter, R.J., "Quantification of Ferritic Steel Weld Metal Microstructures - Summary Report Following Three International Exercises," IIW Doc. IXJ-88-84, American Council, AWS, (1984).
131. Pargeter, R.J., and Dolby, R.E., "Guidelines for Classification of Ferritic Steel Weld Metal Microstructural Constituents, Using the Light Microscope," IIW Doc. IX-1337-85, American Council, AWS, (1985).
132. Committee on Welding Metallurgy of the Japan Welding Society, "Classification of Microstructures in Low-C Low-Alloy Steel Weld Metal and Terminology," IIW Doc. IX-1282-83, American Council, AWS, (1983).
133. Oh, D.W., "The Influence of Boron and Titanium on Low Carbon Microalloyed Steel Weld Metal," M.S. Thesis, Colorado School of Mines, 1987.
134. Thomas, R.D. Jr., Metal Progress, Vol. 111, No. 4, 1977, p. 30.
135. Pederson, K, of Weld Metal: Progress Report No. 1," Royal Norwegian Council for Scientific and Industrial Research, Doc. II-A-446-78 (1978).
136. Glover, A.G., McGrath, J.T., Tinkler, M.J., and Weatherly, G.C., Welding Journal, Vol. 56, 1977, p. 267s.
137. Farrar, R.A, Tulliani, S.S., and Norman, S.R., Welding and Metal Fabrication, Vol. 42, No. 2, 1974, p. 68.
138. Taylor, L.G., and Farrar, R.A., Welding and Metal Fabrication, Vol. 43, 1975, p. 305.
139. Horigome, T., Tsunetomi, E., Shinmyo, K., Nagano, K., Mori, N., and Kato, T., Jor. Japanese Welding Society, Vol. 47, 1978, p. 18.
140. Shiga, A., Imura, H. and Tsuboi, J., "Effects on Niobium and Vanadium on Toughness of Submerged arc Weld Metal," IIW Doc. IX-1049-77, 1021, (1977).
141. Still, J.R., and Roperson J.H., Metal Construction, Vol. 10, No. 7, 1978, p. 339.
142. Dolby, R.E., and Abson, D.J., Welding Institute Report 5509/6/76, (1976).
143. Kirkwood, P.R., Metal Construction, Vol. 10, 260, 1978.

144. North, T.J., Bell, H.B., Nowicki, A., and Craig, I., *Welding Journal*, Vol. 57, p. 63s, (1978).
145. Widgery, D.J., "New Ideas on Submerged Arc Welding," Paper 26, *Welding Institute*, London, (Nov. 1978).
146. Entekin, C.H., Jr., *Metallography*, Vol. 12, 295, (1979).
147. Levine, E., and Hill, D.C., *Metal Construction*, Vol. 9, 346, (1977).
148. Farrar, R.A., and Watson, M.N., *Metal Construction* Vol. 11, 1979, p. 285.
149. Evans, G.M., *Welding Journal*, Vol. 59, 1980, p. 67s.
150. Abson, D.J., R.E. Dolby, and Hart, P.H.M., "The Role of Non-Metallic Inclusions in Ferrite Nucleation in Carbon Steel Weld Metal," Intl. Conf. on "Trends in Steel Consumables for Welding," Paper 25, *Welding Institute*, London, 1978.
151. Keville, B.R., *British Steel Corporation Report No. T/We/1137/1/79/C*, (1979).
152. Pargeter, R.J., *Welding Institute Research Report No. 151/1981* (1981).
153. Dolby, R.E., *Welding Institute Research Report No. 14/1976/M*, (1976). Conf. "Welding Research of the 80's," Paper No. B-24, Osaka.
155. "Specifying Steel Castings," Chapter 27, *Steel Castings Handbook, Fifth Edition*, *Steel Founders' Society of America*, 1980.
156. ASTM Specification A216-75, "Carbon Steel Castings Suitable for Fusion Welding for High-Temperature Service."
157. ASTM Specification A703-74, "General Requirements Applicable to Steel Castings for Pressure Containing Parts,"
158. ASTM Specification E 94-77, "Standard Recommended Practice for Radiographic Testing,"
159. ASTM Specification E 142-72, "Standard Specification for Controlling Quality of Radiographic Testing."
160. ASTM Specification E 446-75, "Standard Reference Radiographs for Steel Castings up to 2 in. in Thickness."
161. ASTM Specification E 186-81, "Standard Reference Radiographs for Heavy-Walled (2 to 4.5 in. (51 to 114 mm)) Steel Castings."

162. ASTM Specification E 280-81, "Standard Reference Radiographs for Heavy-Walled (4.5 to 12 in. (114 to 305 mm)) Steel Castings."
163. ASTM Specification E 390-75, "Standard Reference Radiographs for Steel Fusion Welds."
164. ASTM Specification E 109-63, "Standard Specification for Dry Powder Magnetic Particle Inspection."
165. ASTM Specification E 138-63, "Standard Specification for Wet Magnetic Particle Inspection."
166. ASTM Specification E 125-63, "Standard Reference Photographs for Magnetic Particle Indications on Ferrous Castings".
167. ASTM Specification E 165-75, "Standard Specification for Liquid Penetrant Inspection."
168. ASTM Specification E 433-71, "Standard Reference Photographs for Penetrant Inspection."
169. ASTM Specification A 609 - (Reapproved 1975), "Standard Specification for Longitudinal-Beam Ultrasonic Inspection of Carbon and Low-alloy Steel Castings."
170. ASTM Specification A 370-76, "Standard Specification for Mechanical Testing of Steel Products."
171. ASTM Specification A 488-75, "Standard Qualification of Procedures and Personnel for the Welding of Steel Castings."
172. ASTM Specification A 487-75, "Standard Specification for Steel Castings Suitable for Pressure Service."
173. ASTM Specification A 643-75, "Standard Specification for Steel Castings, Heavy-Walled, Carbon and Alloy, for Pressure Vessels."
174. ASTM Specification A 608-70, "Standard Specification for Centrifugally Cast Iron-Chromium-Nickel High-Alloy Tubing for Pressure Applications at High Temperatures."
175. "Chemical Composition Ni, Co and Fe Base Cast Alloys," Cannon-Muskegon Corporation, 6th Edition.
176. Modern Steels and Their Properties, 7th Edition, Bethlehem Steel, 1972.
177. ASM Metals Handbook, Vol. 7, 8th Edition, American Society for Metals.
178. ASM Metals Handbook, Vol. 2, 8th Edition, American Society for Metals, 1972.

179. Omega Temperature Measurement Handbook, Omega Engineering, Stanford Conn., 1985.
180. Fenton, A.W., "The traveling Gradient Approach to Thermocouple Research," Specialized Techniques in Thermocouple Thermometry, 1971.
181. Temperature, Its Measurement and Control in Science and Industry, Vol. II, American Institute of Physics, 1971.
182. ASTM Manual on the Use of Thermocouples in Temperature Measurement, ASTM Special Publication 470A, 1974.
183. Brown, E., and Nichting, R., Colorado School of Mines, Department of Metallurgical Engineering, Private Communication, unpublished Research, Nov. 1984.
184. Rosenthal, D., "Mathematical Theory of Heat distribution During Welding and Cutting," Welding Research Supplement, May, 1941.
185. Kohno, R., Jones, S.B., "An Initial Study of Arc Energy and Thermal Cycles in Submerged Arc Welding of Steel," Welding Institute Research Report, Dec. 1978.
186. Tsai, C.L., "Modeling of the Thermal Behavior of Metals During Welding," Conference Proceedings, ASM, Metals Park, Ohio, 1982.
187. Geiger, G.H. and Poirier, D.R., Transport Phenomena in Metallurgy, Addison Wesley, 1973.
188. Ion, J.C., Easterling, K.E., and Ashby, M.F., "A Second Report on Diagrams for Heat Affected Zones in Welds," Acta Met., V. 32, No. 11, 1984, pp. 1949-1962.
189. Ashby, M.F., and Easterling, K.E., "The Transformation Hardening of Steel Surfaces by Laser Beams in Hypo-Eutectoid Steels," Acta Met., v.32, No. 11, 1984, pp. 1935-1948.
190. American Society of Mechanical Engineers, 345 East 47th Street, New York, NY 10017.
191. American Welding Society, 550 N. W. LeJeune Road, Post Office Box 351040, Miami, FL 33135.
192. ASTM, 1916 Race Street, Philadelphia, PA 19103.
193. ASTM Specification E749, "Standard practice for acoustic emission monitoring during continuous welding."

NRC FORM 335 (2-89) NRCM 1102, 3201, 3202	U.S. NUCLEAR REGULATORY COMMISSION	<b>1. REPORT NUMBER</b> (Assigned by NRC, Add Vol., Supp., Rev., and Addendum Numbers, if any.)				
<b>BIBLIOGRAPHIC DATA SHEET</b> <i>(See instructions on the reverse)</i>		NUREG/CR-5001				
<b>2. TITLE AND SUBTITLE</b> Effects of Manufacturing Variables on Performance of High-Level Waste Low Carbon Steel Containers		<b>3. DATE REPORT PUBLISHED</b> <table border="1" style="width: 100%;"> <tr> <td style="text-align: center;">MONTH</td> <td style="text-align: center;">YEAR</td> </tr> <tr> <td style="text-align: center;">April</td> <td style="text-align: center;">1990</td> </tr> </table>	MONTH	YEAR	April	1990
MONTH	YEAR					
April	1990					
<b>5. AUTHOR(S)</b>  T. R. Muth, H. R. Frost,* A. L. Liby  *Colorado School of Mines, Golden, Colorado		<b>4. FIN OR GRANT NUMBER</b> FIN B7278  <b>6. TYPE OF REPORT</b> Technical  <b>7. PERIOD COVERED (Inclusive Dates)</b>				
<b>8. PERFORMING ORGANIZATION - NAME AND ADDRESS (If NRC, provide Division, Office or Region, U.S. Nuclear Regulatory Commission, and mailing address; if contractor, provide name and mailing address.)</b> Manufacturing Sciences Corporation P.O. Box 886 Oak Ridge, TN 37831						
<b>9. SPONSORING ORGANIZATION - NAME AND ADDRESS (If NRC, type "Same as above"; if contractor, provide NRC Division, Office or Region, U.S. Nuclear Regulatory Commission, and mailing address.)</b> Division of Engineering Office of Nuclear Regulatory Research U.S. Nuclear Regulatory Commission Washington, DC 20555						
<b>10. SUPPLEMENTARY NOTES</b>						
<b>11. ABSTRACT (200 words or less)</b>  Analytical and experimental research was performed to determine the effect of manufacturing variables on the performance of cast steel overpacks. The work examines the influence of casting and welding process variables on the long-term performance of low carbon steel overpacks in the repository environment. Centrifugal casting was indicated to be the most economical and technically favorable manufacturing approach for cast steel overpacks. A bottom would be welded into a hollow cylinder to make the container and final closure welding to secure the lid would be done at the repository. Effects of alloy chemistry, solidification processing, and solid state phase transformations on final microstructure of the cast and welded overpack has been examined in detail in this report. Codes and standards governing the manufacture of overpacks do not presently exist. An extension of the ASME Boiler and pressure vessel code supplemented by government standards could be adopted for the purpose. Standard, well-established methods of non-destructive evaluation are adequate for the purpose of identifying likely manufacturing defects. Experimental work focused on material and process combinations to be used in manufacture of overpacks. Practical process limits were explored and changes in microstructure due to repository thermal conditions were investigated.						
<b>12. KEY WORDS/DESCRIPTORS (List words or phrases that will assist researchers in locating the report.)</b>  Radioactive Waste Storage; High Level Radioactive Wastes; Containers; Casting; Melting; Submerged Arc Welding; Gas Metal-Arc Welding; Steels; Materials Testing		<b>13. AVAILABILITY STATEMENT</b> Unlimited <b>14. SECURITY CLASSIFICATION</b> <i>(This Page)</i> Unclassified <i>(This Report)</i> Unclassified <b>15. NUMBER OF PAGES</b>  <b>16. PRICE</b>				

UNITED STATES  
NUCLEAR REGULATORY COMMISSION  
WASHINGTON, D.C. 20555

OFFICIAL BUSINESS  
PENALTY FOR PRIVATE USE, \$300

SPECIAL FOURTH-CLASS RATE  
POSTAGE & FEES PAID  
USNRC  
PERMIT No. G-67

120555063583 1 1ANICHIWAIWD1  
US NRC-RES  
DIV OF ENGINEERING  
BRANCH CHIEF  
WASTE MGMT BR  
NL-005  
WASHINGTON DC 20555